

Towards a high-throughput microfluidic drug discovery platform for the screening of GPCR targets in cells

João Fernandes Mateus

Thesis to obtain the Master of Science Degree in

Biological Engineering

Supervisors: Prof. João Pedro Estrela Rodrigues Conde

Prof. Duarte Miguel de França Teixeira dos Prazeres

Examination Committee

Chairperson: Prof. Arsénio do Carmo Sales Mendes Fialho

Supervisor: Prof. João Pedro Estrela Rodrigues Conde

Member of the Committee: Dr. Sofia de Medina Aires Martins

October, 2014

A person who never made a mistake never tried anything new.

– Albert Einstein

Acknowledgements

First I would like to thank my supervisors Prof. João Pedro Conde and Prof. Miguel Prazeres for their support, motivation and ideas during all this work. For the same reasons I thank Dr. Virginia Chu.

A very special thanks to Dr. Sofia Martins for all the guidance, knowledge, help in anything I asked and for giving me the motivation to power through the many obstacles I found during this work.

I would like to thank INESC-MN and IBB for hosting me during this work and for supplying me with all the tools I needed to succeed.

I thank all my colleagues at INESC-MN that helped me with my work, with special notice to: João Tiago Fernandes for letting me adapt his gradient generator channel to my needs and his availability to help. Catarina Pedrosa for teaching me how to use the photodiodes and answering all my questions pertaining to that subject. Ruben Soares for all of his help in anything I asked from microfluidics to 3D printing. Dr. Narayanan Srinivasan for his ideas and for being my mentor during my internship in August 2013, which made me consider doing my dissertation at INESC-MN. Process engineers Virginia Soares and Fernando Silva for their help in microfabrication processes.

I also thank all my colleagues at IBB for their support and good spirits, with special mention to: Dr. Nuno Bernardes and Dr. Dalila Mil-Homens for letting me use the cell culture room whenever I needed. A big thank you to João Trabuco for his help regarding HEK293T cell culture, his insights in cell imaging and microscope tips.

Finally, I would like to thank all of my colleagues, friends and especially family for supporting me during my academic journey and this thesis.

Abstract

G-Protein Coupled Receptors (GPCRs) constitute a large protein family of membrane receptors that play an important role in many cellular processes related to diseases in human beings, and so are primary drug targets for 30-50 % of the pharmaceutical molecules currently available, accounting for annual revenues in the order of the tens of billions (10^9) of United States Dollars. There are about 1000 DNA sequences identified as likely to be GPCRs, with nearly 100 of these confirmed as receptors without any known ligand, and therefore, with great drug discovery potential. Nowadays, the discovery of new drugs targeting GPCRs is done using high throughput screening (HTS) technologies with the activation of receptors being monitored by differences in intracellular calcium. Microfluidics based live cell calcium assays can be performed with low material cost, using smaller volumes of expensive solutions, to present cells with multiple cues that are present in their normal environment.

In this work, an integrated microfluidic device for the screening of GPCR drug targets in cells was conceptualized, with three distinct modules: a microfluidic channel for conducting live cell calcium assays for the screening of GPCR drug targets, a microfluidic gradient generator channel with integrated single cell trapping for performing assays with different concentrations in a single run and integration of hydrogenated amorphous silicon photodiodes with fluorescence filters with the microfluidic channel capable of detecting free calcium concentrations similar to intracellular calcium levels before and after GPCR activation.

Keywords: G-Protein Coupled Receptors, microfluidics, photodiodes, gradient generator

Resumo

Recetores acoplados à proteína G (GPCRs) constituem uma grande família de recetores da membrana que cumprem um papel importante em muitos processos celulares relacionados com doenças em humanos, e assim, são o principal alvo para 30-50% das moléculas farmacêuticas actualmente disponíveis, fármacos estes que facturam anualmente dezenas de biliões (10^9) de dólares. Existem cerca de 1000 sequências de ADN identificadas como podendo ser GPCRs, com perto de 100 destas confirmadas como sendo recetores sem qualquer ligando conhecido, tendo assim um grande potencial para a descoberta de novos fármacos. Actualmente a descoberta de novos fármacos que têm como alvo GPCRs é feita através de tecnologias de elevada capacidade com a activação dos recetores monitorizada pelas diferenças de cálcio intracelular. Ensaios de cálcio com células vivas baseados na microfluídica podem ser feitos com baixo custo de material, usando volumes menores de soluções e proporcionar às células várias condições presentes no seu ambiente normal.

Neste trabalho, um dispositivo microfluídico para a deteção de fármacos que têm como alvo GPCRs em células foi conceptualizado, em três módulos distintos. Um canal microfluídico com uma câmara onde ensaios de cálcio com células vivas são efectuados com o intuito de testar ligandos de GPCRs, um canal gerador de gradientes microfluídico com armadilhas celulares individuais para executar ensaios com concentrações diferentes simultaneamente e, a integração de fotodíodos de silicone amorfo hidrogenado com filtro de absorção incorporado num canal microfluídico capaz de detetar concentração de cálcio similares aquelas encontradas num ambiente intracelular antes e depois da activação dos GPCRs.

Palavras-Chave: Recetores Acoplados à Proteína G, microfluídica, fotodíodos, gerador de gradiente

Table of Contents

Acknowledgements	v
Abstract	vii
Resumo	ix
Table of Contents	xi
List of Tables	xiii
List of Figures	xiv
Abbreviations	xvi
1. Introduction	1
1.1. G-Protein Coupled Receptors	1
1.1.1. The Potential of GPCRs as Drug Discovery Targets	1
1.1.2. GPCR signaling	2
1.1.3. Receptor targeting drugs	5
1.1.4. Purinergic Receptors	6
1.2. Microfluidics	8
1.2.1. Brief History	8
1.2.2. Basic Principles	8
1.2.3. Soft Lithography and PDMS	9
1.2.4. Cell Trapping	10
1.2.5. Live Cell Assays	11
1.2.6. Gradient Generation	13
1.3. Photodiodes	14
1.3.1. p-i-n Photodiodes	14
1.3.2. Amorphous Silicon Photodiodes Integration	16
1.4. Objectives	17
2. Materials and Methods	18
2.1. Animal Cell Culture	18
2.2. Microtiter Plate Live Cell Calcium Assays	19
2.3. Hard Mask Fabrication	20
2.4. Mold Fabrication	21
2.5. PDMS Fabrication	22
2.6. Microfluidic live cell calcium assays	23
2.6.1. Microfluidic Chamber	23
2.6.2. Microfluidic Gradient Generator	24
2.7. Gradient Generation with Calcium Solutions	25
2.8. Video and Data Analysis	26
2.9. Photodiode Characterization	27

3. Results and Discussion.....	30
3.1. Macroscale.....	30
3.1.1. Agonist Assays.....	30
3.1.2. Antagonist Assays.....	36
3.2. Microscale.....	39
3.2.1. Fluo4 Direct Optimization.....	39
3.2.2. Agonist Assays.....	41
3.2.3. Antagonist Assays.....	46
3.2.4. Single Cell Traps.....	49
3.2.5. Gradient Generation with Calcium Solutions.....	52
3.3. Photodiode experiments.....	57
3.3.1. Photodiode Characterization.....	57
3.3.2. Calcium Fluorescence Experiments.....	60
3.3.3. Microfluidic Live Cell Calcium Assay with Photodiodes.....	62
4. Conclusions.....	64
5. Future Work.....	66
References.....	67
A. Appendix Section.....	70
a. Calculating Free Calcium Concentrations.....	70
b. Video Analysis Methods.....	71
c. AutoCAD Microchannel Designs.....	75
d. Crystalline Silicon Photodiode.....	79
e. Hydrogenated Amorphous Silicon Photodiode.....	80
f. SolidWorks Support.....	81

List of Tables

Table 1.1 Five Top-Selling Drugs Targeting GPCRs in 2003.....	1
Table 1.2 Different GPCR subtypes and their specific pathways.....	4
Table 3.1 EC50 values and its 95% confidence intervals for different combinations of video analysis methods and assay buffer composition.	35
Table 3.2 Photo fluxes for the light sources used.	59
Table A.1 Dissociation constants of EGTA for Ca ²⁺ in 0.1 M KCl.....	70
Table A.2 Spectral response characteristic of the Hamamatsu photodiode.	79

List of Figures

Figure 1-1 Mechanism of GPCR activation mediated by the heterotrimeric G-Protein.	3
Figure 1-2 Intracellular calcium release after GPCR activation.	4
Figure 1-3 Diagram showing the effect of agonist or antagonist drugs.	5
Figure 1-4 P2Y2's main agonists.	7
Figure 1-5 P2Y2's antagonists.	7
Figure 1-6 Soft lithography microfabrication technique using PDMS	9
Figure 1-7 Multi cell hydrodynamic chamber trap.	10
Figure 1-8 Hydrodynamic single cell trapping mechanism.	11
Figure 1-9 A micro titer plate (left) and a microfluidic device (right).	12
Figure 1-10 A microfluidic laminar flow based gradient generator.	13
Figure 1-11 Diagram of the photoelectric effect on a semiconductor.	14
Figure 1-12 Example of a p-i-n photodiode cross section.	15
Figure 1-13 Band diagrams of the three different types of semiconductors in p-i-n photodiodes.	15
Figure 1-14 p-i-n photodiode working in reverse bias.	16
Figure 2-1 Schematics of the cell harvesting process.	18
Figure 2-2 Diagram of the agonist fluorescence live cell calcium assays in microtiter plates.	19
Figure 2-3 Diagram of the antagonist fluorescence live cell calcium assay in microtiter plates.	19
Figure 2-4 Schematics of the hard mask fabrication process.	20
Figure 2-5 Schematics of the mold fabrication process.	21
Figure 2-6 Schematics of the PDMS microchannel fabrication process.	22
Figure 2-7 Diagram of the fluorescence live cell calcium assay in a microfluidic channel.	23
Figure 2-8 Diagram of a live cell calcium assay using the gradient generator channel.	24
Figure 2-9 Diagram of a gradient generator experiment.	25
Figure 2-10 Photograph of the photodiodes used.	27
Figure 2-11 Optical table setup with the components used for the photodiode characterization.	27
Figure 3-1 Contrast between the background and cell fluorescence using Fluo4 Direct™.	30
Figure 3-2 Cell response to different UTP concentrations at similar time points in well plates.	31
Figure 3-3 Normalized fluorescence vs. time for different UTP concentrations in microtiter plates. ...	32
Figure 3-4 Hill dose-response curve for UTP in microtiter plates.	33
Figure 3-5 UTP dose-response for experiments with and without calcium ions in the assay buffer. ...	34
Figure 3-6 Cell response to different concentrations of suramin and a fixed UTP concentration.	36
Figure 3-7 Normalized fluorescence vs time for different suramin concentrations in microtiter plates.	37
Figure 3-8 Antagonist Hill dose-response curve for suramin in microtiter plates.	38
Figure 3-9 Chamber of the microfluidic channel with cells.	39
Figure 3-10 Microfluidic Fluo4 Direct™ concentration optimization experiments.	40
Figure 3-11 Cell response to different UTP concentrations at similar time points in the microfluidic chamber.	42
Figure 3-12 Normalized fluorescence vs time for different UTP concentrations in the microfluidic chamber.	43
Figure 3-13 Hill dose-response curve for UTP in the microfluidic chamber.	44
Figure 3-14 Normalized fluorescence vs time for different suramin concentrations in the microfluidic chamber.	46
Figure 3-15 Normalized fluorescence vs time for different mixed antagonist assays in the microfluidic chamber channel.	47
Figure 3-16 Hill dose-response curves for the mixed antagonist assays in the microfluidic chamber.	48
Figure 3-17 Cells trapped inside the gradient generator channel using fibronectin.	49
Figure 3-18 Cells trapped inside the gradient generator channel without using fibronectin.	50
Figure 3-19 Single cell traps inside the gradient generator channel.	51
Figure 3-20 Cell leaving the trap through its opening, after being trapped.	51
Figure 3-21 Formation of blebs on a cell in a trap.	52
Figure 3-22 Representation of the gradient generator bifurcations and assigned letters.	53
Figure 3-23 Mixing of two different bifurcations at an intersection.	54
Figure 3-24 CaEGTA concentration in each of the different areas of the channel.	54
Figure 3-25 Gradient Generation using CaEGTA solutions with Fluo4.	55
Figure 3-26 Determination of the time for gradient generation.	55
Figure 3-27 Fluorescent cells inside the gradient generator channel.	56

Figure 3-28 Current density vs voltage plot for the different light sources and the dark.....	57
Figure 3-29 External quantum efficiency of the photodiode for wavelengths ranging from 400 to 600 nm.	58
Figure 3-30 Relationship between the current densities (J) and the incident photon flux (Φ) for different light sources.	59
Figure 3-31 Fluorescent calcium solutions inside the microfluidic chamber channel.	60
Figure 3-32 Calcium fluorescence measurement using photodiodes with the LED and lamp-monochromator combo.	61
Figure 3-33 Current density vs time for a microfluidic live cell calcium assay.	63
Figure A-1 Stack converted to grayscale.	71
Figure A-2 Mean image intensity values over time, without removing background.....	71
Figure A-3 Z Project image representing the maximum intensity of each pixel of the stack.	72
Figure A-4 Enhanced Z Project image.....	72
Figure A-5 Enhanced Z Project image after being subjected to an auto threshold.	73
Figure A-6 Stack with the background removed.	73
Figure A-7 Comparison of the final results after removing and not removing background.	74
Figure A-8 Microfluidic chamber channel schematics.	75
Figure A-9 Dual chamber variation of the microfluidic chamber channel.	75
Figure A-10 Gradient Generator channel schematics.	76
Figure A-11 Serpentine section of the gradient generator channel. It is in this section that the fluid will mix and form a gradient in the traps section.	77
Figure A-12 Gradient generator trapping area close-up.	78
Figure A-13 Hamamatsu S1226-5BQ crystalline silicon photodiode.....	79
Figure A-14 Cross section of the 200 × 200 μm^2 hydrogenated amorphous silicon photodiodes used.	80
Figure A-15 Amplification of different areas of the hydrogenated amorphous silicon photodiodes.....	80
Figure A-16 LED-filter system with the support made in SolidWorks.	81
Figure A-17 Exploded view of the LED-filter system.	81

Abbreviations

a-Si:H Hydrogenated Amorphous Silicon
Photodiode

ATP Adenosine triphosphate

AU Arbitrary units

AVI Audio Video Interleaved

cAMP Cyclic adenosine monophosphate

DMEM Dulbecco's Modified Eagle's medium

DMSO Dimethyl sulfoxide

EC50 Half maximal effective concentration

ECM Extracellular matrix

EDTA Ethylenediaminetetraacetic acid

EGTA Ethylene glycol tetraacetic acid

FBS Fetal Bovine Serum

GPCR G protein-coupled receptor

GTP Guanosine-5'-Triphosphate

HBSS Hank's Balanced Salt Solution

HEK Human Embryonic Kidney

HEPES 4-(2-hydroxyethyl)-1-piperazineethanesulfonic acid

HRP Horseradish peroxidase

HTS High-Throughput Screening

IC50 Half maximal inhibitory concentration

IP3 Inositol-1,4,5-triphosphate

IP4 Inositol-1,3,4,5-tetrakisphosphate

IPA Isopropyl alcohol

LOC Lab-on-a-chip

LED Light emitting diode

MEMS Micro Electro-Mechanical Systems

PBS Phosphate Buffered Saline

PDMS Polydimethylsiloxane

PGMEA Propylene glycol methyl ether acetate

PIP2 Phosphatidylinositol-4,5-bisphosphate

PLC phosphoinositol phospholipase C enzyme

SEM Standard Error of the Mean

UTP Uridine-5'-triphosphate

μTAS Micro-Total-Analysis-Systems

1. Introduction

1.1. G-Protein Coupled Receptors

1.1.1. The Potential of GPCRs as Drug Discovery Targets

As Gareth Thomas (2003) in his book “Fundamentals of Medicinal Chemistry” rightly pointed out, “*Drug discovery is part luck and part structured investigation*”, the process of finding and launching novel drugs combines both systematic analysis and serendipity. Historically, most drugs were discovered by figuring out the active ingredient from traditional remedies or fortuitous discovery. Nowadays, modern drug discovery relies on the identification of screening hits, medicinal chemistry and the optimization of those hits. But even with significant breakthroughs in the understanding of biological systems and the advances in technologies introduced during recent years, drug discovery remains a difficult and expensive endeavor. Because of these difficulties, it is of crucial importance to find drug targets that serve an important role in cell processes, lead to a desirable therapeutic effect and have economic viability. [1][2]

GPCRs (G-protein coupled receptors) play an important role in many physiological and disease related processes in human beings and, due to their importance in the regulation of cell activity, are primary drug targets for 30-50% of the pharmaceutical molecules currently available, which account for annual revenues in the order of the tens of billions (10⁹) of US Dollars.[3]–[6]

Table 1.1 Five Top-Selling Drugs Targeting GPCRs in 2003 [7]

Trade Name	Brand Name	GPCR	Indication	Sales(\$ Billions)
Salmeterol	Advair/Seretide/ Serevent	β_2 -adrenergic	Asthma	4.351
Olanzapine	Zyprexa	5HT ₂	Schizophrenia	4.277
Clopidogrel	Plavix	P2Y ₁₂ -purinergic	Thrombosis	3.966
Losartan	Cozaar/Hyzaar/ Nu-Lotan	AT ₁ -angiotensin II	Hypertension	2.939
Valsartan	Diovan/Co- Diovan	AT ₁ -angiotensin II	Hypertension	2.425

Generating an enormous amount of revenue and representing a quarter of the US top selling drugs makes GPCRs one of the prime drug discovery targets today. In addition, they are one of the largest classes of receptors in the human genome, with about 1000 sequences identified as likely to be GPCRs and with nearly 100 of these sequences confirmed as receptors, but without any known ligand. These aptly named 'orphan receptors' are seen as having the greatest drug discovery potential. Additionally, there are many non-orphan GPCRs that are not specifically targeted by any drug.[8]

GPCRs are activated by a wide range of ligands, including peptides, hormones, amino acids, photons and ions; additionally, they also transduce signals through many different effectors, having numerous diseases and disorders linked to mutations and polymorphisms in GPCRs. They are active in practically all organ systems, and so present a broad array of opportunities as therapeutic targets in areas such as cancer, cardiac dysfunction, diabetes, central nervous systems disorders, obesity, inflammation and pain. [6][9]

The discovery of new molecules that have GPCRs as drug targets is currently being performed by high-throughput screening platforms (HTS). In these platforms, millions of different test compounds are brought into contact with live cells and the response elements of the GPCR's signaling cascade are monitored using fluorescent or luminescent read-outs. Nowadays, the most used tools for this are the fluorescent imaging plate readers which allow multiwell plate analysis of GPCR activation events; these events in turn give good hints of small-molecule drug leads. [5][9] These technologies are being adopted as they can provide automation, miniaturization and fast turnaround times, which lead to a reduction in screening assay cost. [10][11]

These technologies can only provide miniaturization to a certain degree, and so using concepts such as microfluidics could lead to further improvements, with some new platforms being developed with this new field in consideration. [12][13]

1.1.2. GPCR signaling

The signaling system of GPCR is highly complex and based on three major elements: a GPCR with the ability to couple with a heterotrimeric guanosine-5'-triphosphate (GTP) binding protein (G-protein), a GTP-transferase active G-protein and a second messenger generating enzyme. The general accepted mechanism of GPCRs relies on the connection of the ligand to the receptor being coupled to the second messenger forming enzyme through the heterotrimeric G-protein. The binding of the ligand to the GPCR causes a change in the receptor conformation, which, in turn binds and activates the G-protein. The now active form of the G-protein is released from the surface of the receptor, dissociating into its α and β/γ subunits. These two subunits will, in turn, activate their specific effectors, leading to the release of second messengers, which are recognized by specific proteins, such as protein kinases, causing their activation and triggering of the signaling cascade towards a complex biological event (Figure 1-1). The G-protein is regenerated through the hydrolysis of the GTP molecule and re-trimerisation of the G-protein to its inactive form.[8]

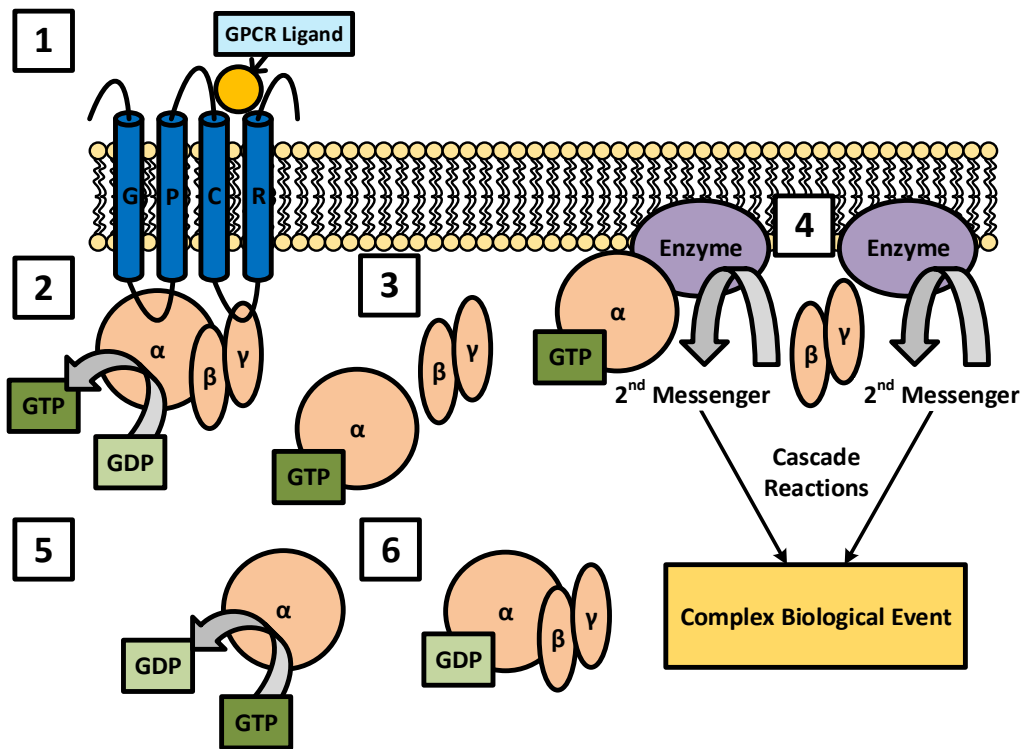


Figure 1-1 Mechanism of GPCR activation mediated by the heterotrimeric G-Protein. (1) Binding of the ligand to the GPCR. (2) The conformational change of the receptor due to the ligand binding leads the α subunit to release GDP and bind to a new GTP molecule. (3) The active G-protein form is released from the GPCR. (4) The α -GTP complex and $\beta\gamma$ subunits dissociate and both associate independently with second messenger-generating enzymes, causing the release of messenger molecules, which in turn trigger a biological or physiological event. (5) The α -GTP complex converts into α -GDP, due to GTPase activity, with the release of inorganic phosphate. (6) The α -GDP subunit reverts to its native state by re-binding with to the $\beta\gamma$ subunits causing the inactivation of the G-protein. Diagram based on [8].

As seen in Figure 1-1 the GPCR actuation principle is complex, with several different processes occurring before a regulating biological event happens. In order to detect the function of a GPCR receptor, the monitoring of some of these processes could be accessed. One of the events that occurs in the signaling cascade is the release of calcium ions from the endoplasmic reticulum to the cytosol. These ions function as second messengers and can be monitored in a variety of ways, and will be the GPCR revealing element in this thesis.

Table 1.2 Different GPCR subtypes and their specific pathways.[8]

Type	Action	Second messenger
$G_{\alpha s}$	Activate adenylate cyclase	cAMP
$G_{\alpha i}$	Inactivate adenylate cyclase	cAMP
$G_{\alpha q}$	Regulate phospholipase C	IP3/Cytosolic calcium
$G_{\alpha o}$	Regulate phospholipase C	IP3/Cytosolic calcium

The second messenger releasing enzymes comprise two main groups, with each one being activated or inactivated by different types of G-proteins (Table 1.2). The $G_{\alpha s}$ and $G_{\alpha i}$ subtypes either activate or inactivate, respectively, the adenylate cyclase enzyme that converts adenosine triphosphate (ATP) into cyclic adenosine monophosphate (cAMP), simultaneously releasing pyrophosphate, whereas other subtypes, namely $G_{\alpha q}$ and $G_{\alpha o}$ will alternately activate the phosphoinositol phospholipase C enzyme (PLC) which hydrolyses phosphatidylinositol-4,5-biphosphate (PIP₂) into sn-1,2 diacylglycerol (DAG) and inositol-1,4,5-triphosphate (IP₃). The IP₃ molecule binds to an endoplasmic reticulum calcium channel, triggering the release of calcium ions into the cytosol. There are also other IP₃ derivatives which have cell function modulating properties, such as inositol-1,3,4,5-tetraphosphate (IP₄) that has the ability to facilitate the release of calcium caused by the IP₃ (Figure 1-2). [8]

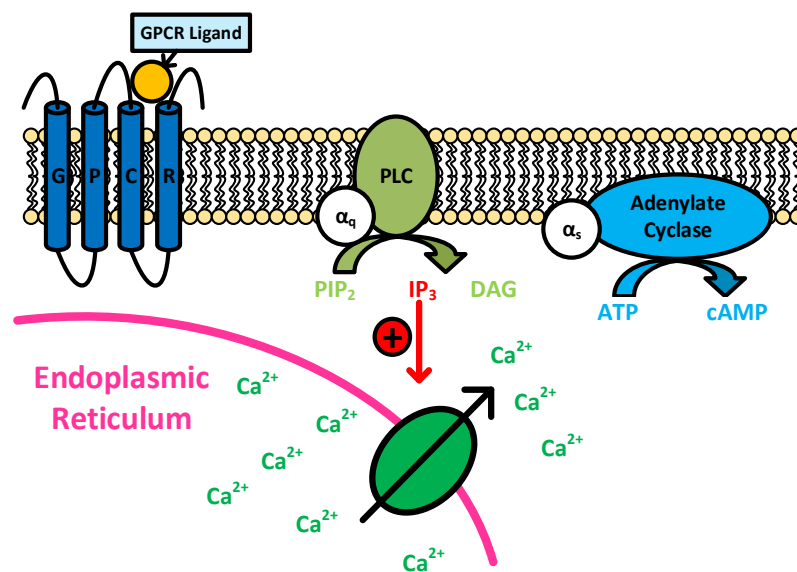


Figure 1-2 Intracellular calcium release after GPCR activation.

The activation of the GPCR by an agonist will trigger the release of intracellular calcium, while the binding of an antagonist will lead to inhibition and no change in this element.

1.1.3. Receptor targeting drugs

As mentioned earlier, GPCR targeting drugs are one of the most commonly existent drug types in modern times. These GPCR targeting drugs bind to a receptor, and either inhibit its action or stimulate the receptor to give a biological response characteristic of the drug. The drugs that stimulate, in a similar manner to an endogenous ligand, upon receptor binding are called agonists, whereas drugs that bind to a receptor and do not cause a response are called antagonists.. A visual representation of the effect of these two types of drugs is in Figure 1-3. [1] Agonists commonly have similar structure to the endogenous ligand of the receptor. The increase of concentration of an agonist cause increased cell activity, until it reaches a maximum, at which point the receptors of the cells for that particular agonist are saturated. There are pure agonists and partial agonists, the former pertains to drugs that bind to the receptor and are capable of a strong activation, the latter are compounds that act both as agonists and antagonists, binding to the receptor, preventing pure agonists or endogenous ligands from binding, but still weakly activating the receptor. [1] They are often grouped into two types, competitive and non-competitive antagonists. Competitive antagonists bind the same receptor as an agonist but don't cause a response, so the increase of the antagonist's concentration causes a decrease in response due to the agonist. However, by increasing the agonist's concentration this phenomenon can be reversed, as there is competition for the binding site. In the case of non-competitive antagonists it is believed that they bind irreversibly by strong bonds to allosteric sites on the receptor and prevent the agonist from binding, in spite of its concentration. This occurs, since the binding of a non-competitive antagonist leads to changes in receptor conformation, with the agonist not being able to bind. [1]

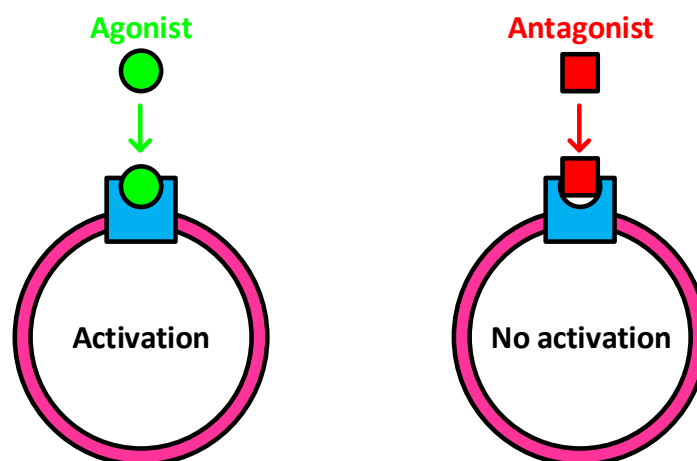


Figure 1-3 Diagram showing the effect of agonist or antagonist drugs. Both the agonist and the antagonist bind to the receptor (blue), on the surface of the cell membrane (pink), with the agonist causing the activation of the receptor while the antagonist not.

In this work, two main receptor targeting drugs were used. One was a pure agonist of the purinergic receptor P2Y₂, called UTP and the other was a weak antagonist for the same receptor called Suramin.

1.1.4. Purinergic Receptors

The main GPCR studied in this work was the P2Y₂ receptor, which belongs to the purinergic receptor family. This family of receptors was first defined in 1976 and comprises of two types of purinoceptors, the P1 and P2. What distinguishes the two types are their ligands, P1 is a receptor for adenosine and P2 is a receptor for ATP/UTP/ADP. Among the P2 receptors, there are two major families, the P2X and P2Y. The P2X a family of ligand-gated ion channel receptors and the P2Y, a family of G-protein coupled purinoceptors. The purinergic signaling is a primitive system involved in many non-neuronal and neuronal mechanisms, in both short and long term events. They are involved in exocrine and endocrine secretion, immune response, pain, inflammation, platelet aggregation, endothelial-mediated vasodilatation, cell proliferation and death. [14]

The term P2Y is used for functional mammalian receptor proteins and functional non-mammalian species. Currently, there are 8 of these receptors that have been discovered in humans: P2Y₁, P2Y₂, P2Y₄, P2Y₆, P2Y₁₁, P2Y₁₂, P2Y₁₃ and P2Y₁₄, with the missing numbers pertaining to either nonmammalian orthologs or receptors having some sequence homology to P2Y receptors, but with no established functional response to nucleosides. In pharmacological terms, P2Y receptor can be subdivided into 1) adenine nucleotide-preferring receptors, which respond mainly to ADP and ATP, included in this group are human and rodent P2Y₁, P2Y₁₂ and P2Y₁₃, and human P2Y₁₁. 2) Uracil nucleotide-preferring receptors, such as P2Y₄ and P2Y₆, responding to either UTP or UDP. 3) Mixed selectivity receptors, comprising of the human and rodent P2Y₂, rodent P2Y₄ and, possibly, P2Y₁₁. And lastly, 4) receptors responding solely to the sugar nucleotides UDP-galactose and UDP-galactose, P2Y₁₄. [15][16]

The GPCR studied in this work, P2Y₂, is expressed in many tissues including lung, heart, spleen, kidney, skeletal muscle, liver and epithelia. This receptor plays an important role in regulating ion transport in epithelial cells. P2Y₂ receptors can directly couple to PLC β ₁ (phospholipase C- β 1) via G α _{q/11} protein to mediate the production of IP₃, second messenger for calcium release from intracellular stores. The activation of the P2Y₂ receptor leads to the opening of N-type Ca²⁺ channel, a voltage-dependent calcium channel, which causes the increase of intracellular calcium. The action of the P2Y₂ receptor on N-type Ca²⁺ channels is very similar to the endogenous M1 receptor (Muscarinic acetylcholine receptor), with both receptors linking to a G α _{q/11} protein which regulates PLC and has, as second messengers, IP₃ and cytosolic calcium (Table 1.2). In terms of activation, P2Y₂ is activated almost equipotently by UTP and ATP, but is not activated by the corresponding 5'-diphosphates, such as UDP and ADP, since the potency of P2Y receptors is dependent on the number of bridging phosphate units, with the optimum being the tetraphosphate. It was also reported that substitution of the uracil ring of UTP reduces potency at the P2Y₂ receptor. The agonists for P2Y₂ are important for the treatment of pulmonary and ophthalmic diseases and possibly cancer.[15]

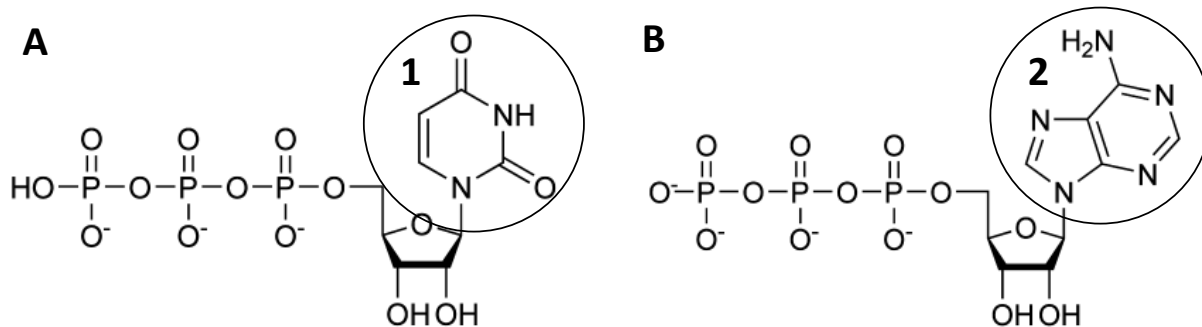


Figure 1-4 P2Y2's main agonists. (A) UTP (uridine-5'-triphosphate) chemical structure, with (1) being the uracil group. (B) ATP (adenosine-5'-triphosphate) chemical structure, with (2) being the adenosine group. Both molecules also have in common a ribose and triphosphate group.

The P2Y2 is antagonized by a family of selective, heterocyclic antagonists containing a thiouracil moiety, including AR-C126313 and AR-C118925. Flavonoids have also been identified as P2Y2 receptor antagonists, with Tangeritin being a potent, noncompetitive antagonist. Additionally, suramin acts as competitive weak antagonist of the P2Y2 receptor and its derivatives are relatively nonselective P2 antagonists having, in general, reversibility upon washout.[15]

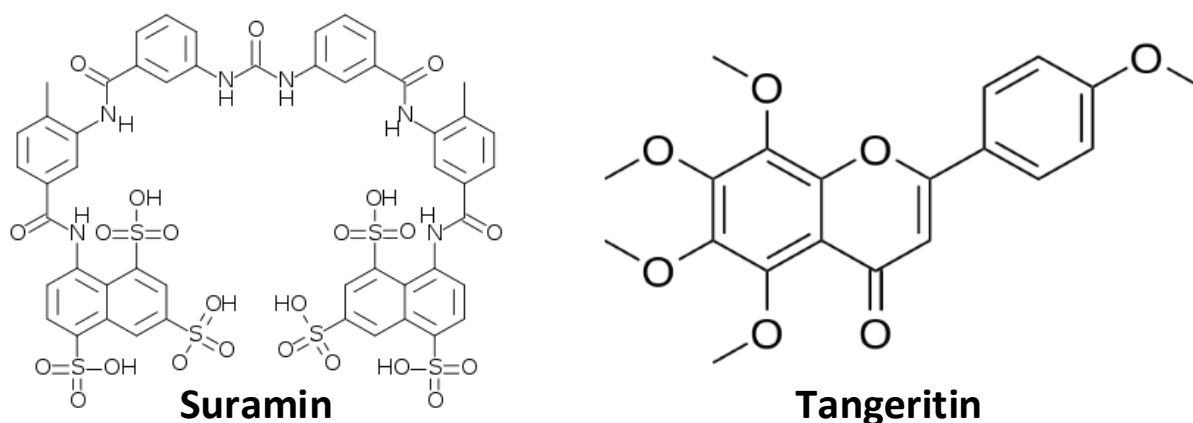


Figure 1-5 P2Y2's antagonists. Suramin is a weak P2Y2 antagonist and also used as a treatment for sleeping sickness. Tangeritin is a flavonoid that acts as a P2Y2 antagonist, it can be found in tangerine and shows enormous potential as an anti-cancer agent.

1.2. Microfluidics

1.2.1. Brief History

In the last couple of decades, the field of miniaturization has seen great progress. Because of this, it is now possible to miniaturize down to submicron sizes a broad range of systems, such as mechanical, fluidic, electromechanical or thermal systems. In the 1980s, the field of Micro Electro-Mechanical Systems (MEMS) was created and in the 1990s became considerably diversified, with devices being created to be used for chemical, biological and biomedical applications. Because of the reduced size of these devices, these systems were employing fluid flows operating under unusual and unexplored conditions, which led to the need for the creation of a new discipline called microfluidics.[17]

1.2.2. Basic Principle

In its simplest form, microfluidics can be defined as the science that deals with liquid flows inside channels at the micrometer scale. The use of microfluidics brings many advantages to a variety of fields, with the possibility of integration, in miniaturized chips, of otherwise very complex assays, reducing costs and time. The costs are reduced by using smaller volume of expensive reagents and through economies of scale, which also provide the possibility of high throughput assays.[18] The usage of very small volumes of liquid, ranging from fl to μl , flowing inside the channels also proves to be an advantage, not only enabling cost reduction, but also due to the unique conditions that arise at such small volumes. The flow regime in microfluidic channels is defined by the Reynolds number.

$$Re = \frac{\rho v D}{\mu} \quad \text{Equation 1}$$

In Equation 1, the Reynolds number expression is depicted, with ρ representing the density of the fluid, v the velocity inside the channel, D the diameter of the channel (as most channels are have a rectangular cross section, the diameter used is usually the hydraulic diameter) and μ the viscosity of the fluid. As the diameter or hydraulic diameter in microfluidics is in the order of microns and the flow rates usually in the order of $\mu\text{L}/\text{min}$ or lower, the velocity is also not very high (despite low square section area), leading to low Reynolds numbers and to laminar flow inside the channel. For laminar flow to be present, the Reynolds number needs to be lower than 2040 [19], and because values higher than this seldom happen at the microscale, laminar flow is very likely. In the laminar flow regime, viscosity plays an important role in mass transport and because there is no turbulence, two adjacent layers of different liquids will not mix through convection, but only by diffusion, and so aqueous two phase systems and gradient generation can be employed in microfluidics. In chemical and biological assays, because the surface area to volume ratio in microfluidic devices is commonly higher than in traditional systems, there is enhanced detection sensitivity as the sample being tested has a bigger area of contact with the sensing element. This increase in surface area to volume ratio also increases heat transfer and mass transport.[18]

1.2.3. Soft Lithography and PDMS

When thinking about microfluidics, it is difficult not to mention its most used microfabrication technique and important elastomer. For fabricating microfluidic channels for chemical or biological applications, the most widely used technique is soft lithography. In this process, the central substance and one that makes microfluidic channel fabrication relatively easy and inexpensive, is polydimethylsiloxane, commonly abbreviated to PDMS. PDMS, which is the most widely used silicon-based organic polymer, is an elastomer formed by mixing a silicon rubber base with a curing agent and cured at a higher temperature than its polymerization's.[17]

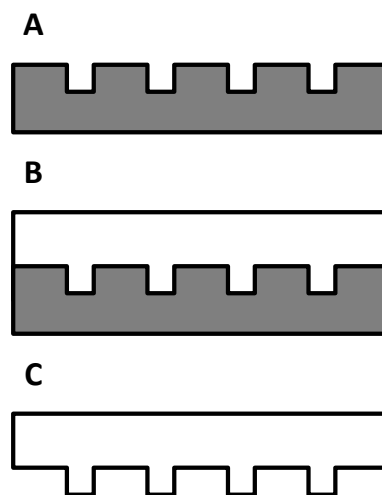


Figure 1-6 Soft lithography microfabrication technique using PDMS (A) The mold is fabricated, usually made from silicon. (B) The PDMS mix, silicon rubber base and curing agent, is poured over the mold. The PDMS mold set is cured at a higher temperature than the PDMS polymerization temperature. (C) The PDMS is peeled off the mold.

Using PDMS for microfabrication, it is possible to achieve great precision of the structures, with submicrometric features being a possibility. However, due to the elastomeric character of the materials and aging phenomena, the microchannel dimensions best suited for PDMS lie between 5 and 500 μm . Its most remarkable features, with respect to microfluidics and microfabrication, are its optical transparency between 300 nm and 2200 nm, which make it perfect for the visualization of flows. Its elastomeric quality facilitates watertightness of microfluidic connections, tightly hugging the shape of fluid pathways. Its elasticity also proves to be an advantage, enabling the fabrication of valves and pumps using membranes. Naturally PDMS is hydrophobic, but when oxidized it becomes hydrophilic (temporarily) and adheres non-reversibly to other materials, most notably glass if its surface was also oxidized. PDMS is also permeable to gas, which enables the exchange of gases between the channel and the exterior, making it possible to culture cells and facilitate filling, as air bubbles can escape through the material. All of these features, in addition to its non-toxicity and non-reactivity, make PDMS the top choice with respect to fluid management inside microchannels, and so, most complex lab-on-a-chip (LOC) systems today are made of PDMS.[17]

1.2.4. Cell Trapping

The need to conduct live cells assays in a precisely controlled environment, to understand and assess complex fundamental processes involved in cell regulating mechanisms, has continuously driven science to develop new technologies, with miniaturization being a main focus. In order to perform cell assays in microfluidics, there needs to be a way to fixate the cells inside the microchannel, so that using optical, magnetic or hydrodynamic methods, cell populations can be monitored. It is possible, using cell trapping strategies, to effectively trap the cells inside microfluidic channels. [20]

A simple way of making sure adherent cells, such as HEK (Human Embryonic Kidney), become stuck inside a channel, and one of the strategies used in this work, is to design an area (such as a chamber) in the microchannel larger than the channel leading up to it. This enables the expansion of the flow in the larger area, slowing the fluid and cells down which, when the flow is stopped, will tend to settle there. This method works best if, before inserting the cells, the channel is incubated with a solution of ECM (Extracellular Matrix) protein, such as fibronectin or laminin, which allow the cells to adhere better. An example of this can be seen in Figure 1-7.

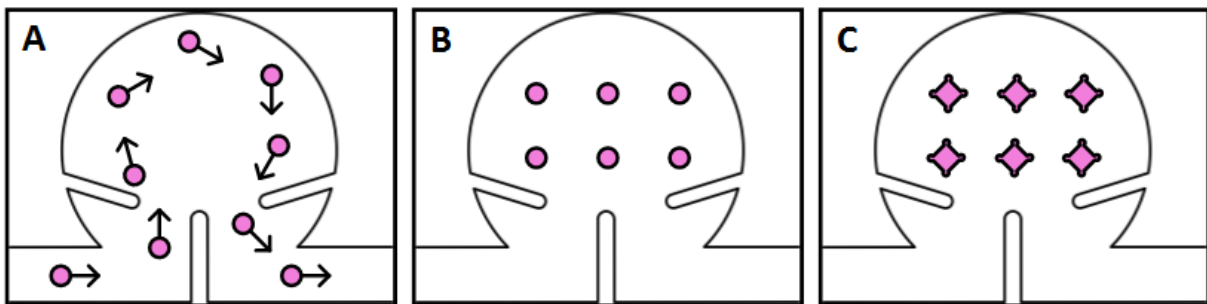


Figure 1-7 Multi cell hydrodynamic chamber trap. (A) The cells are flowed inside the channel. (B) The flow is stopped and the cells settle inside the chamber. (C) If the channel was incubated with an ECM protein, the cells will adhere to the channel and change shape.

Single cell trapping in microfluidics is an interesting concept, since it enables single cell analysis which offers the possibility of extracting detailed information on inherent cell-to-cell variations in large populations, enabling a deeper understanding of cell dynamics. Various single cell trapping strategies exist, ranging from low to high complexity. Some strategies worth mentioning include optical trapping, where a tightly focused laser is used to trap and manipulate cells with very high precision, and dielectrophoretic trapping, where the cells are aligned due to forces generated by a non-uniform field.[20][21]

The most notable strategy and most common way of achieving single cell trapping in microchannels is through hydrodynamic cell trapping. One example of such strategy is in Figure 1-8.

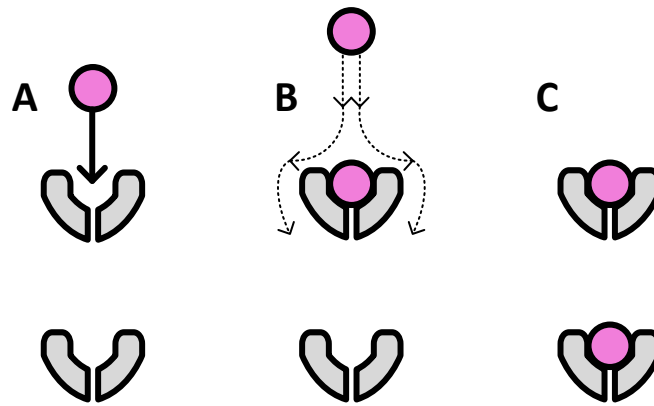


Figure 1-8 Hydrodynamic single cell trapping mechanism. (A) The cell flows into the trap due to the opening that allows fluid to pass through. (B) Because the opening of the occupied trap is blocked the cell flow is diverted. (C) The diverted cell occupies the second trap, as the opening was unblocked.

This strategy is very straightforward material-wise, as the microfabrication and assaying methods are the same as for a simple straight channel, which is something that does not happen when using optical or dielectrophoretic cell trapping, since additional equipment is needed. The main difficulty of this strategy is designing the channels, because a slight variation in the trap design can cause the cells to form clusters or avoid the traps altogether. Due to its simplicity and existent know-how, hydrodynamic single cell trapping was the chosen strategy for the gradient generator channel designed in this work.

1.2.5. Live Cell Assays

Using microfluidics, it is possible to conduct live cell assays under a precisely controlled environment, while using minor quantities of expensive chemicals and precious drugs. These microfabricated systems can present cells with multiple cues that are present in their normal environment, including direct cell-to-cell contact and biochemical and mechanical interactions with ECM proteins, in a controllable and reproducible fashion that cannot be easily achieved in standard assays, and can be used to link live cell assays with integrated analytical devices that can probe the biological processes that govern cell behavior. Microfluidic cell-based systems can simply represent miniaturized versions of conventional laboratory techniques, while others exploit the advantages of small length scales and low Reynolds numbers.[21][22]

The majority of cell-based microsystem research has been focused on LOC or micro-total-analysis-systems (μ TAS) which have the goal of creating microsystems that incorporate several steps of an assay into a single device. These integrated microfluidic devices perform rapid and reproducible measurements on small volume samples while eliminating the need for labor-intensive and potentially error-prone laboratory manipulations.[22] Some microfluidic devices allow experiments that can't be performed simply by miniaturizing and mechanizing conventional laboratory procedures using robotics and micro titer plates. In cell-based studies, the macroscale transition from 384 to 1536 well plates is proving to be a challenge, as uncontrolled evaporation and edge effects result in poorly defined culture conditions in very small wells. Working with very small fluidic volumes using conventional methods is

difficult, and subjected to both variability and high fixed losses, and so, using automated microfabricated devices allows small reagent volumes to be used effectively and labor cost to diminish. Additionally, the small footprint and low power consumption of integrated systems allow the creation of new portable devices capable of performing sophisticated analyses previously only possible in research laboratories.[22]

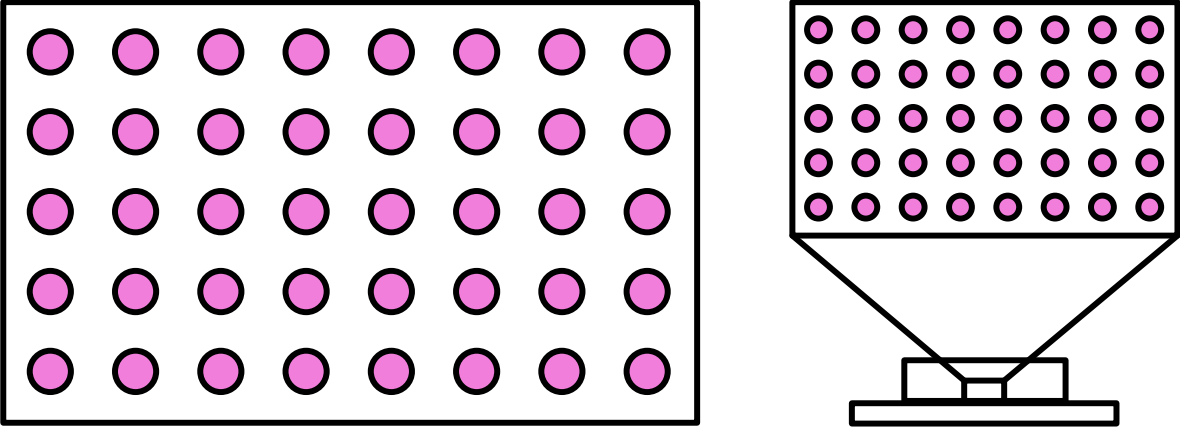


Figure 1-9 A micro titer plate (left) and a microfluidic device (right). Microfluidic devices use smaller volumes and occupy less space than traditional research laboratory equipment.

1.2.6. Gradient Generation

In biological systems, biomolecular gradients play an important role in many phenomena, such as development, inflammation, wound healing and cancer. Therefore, the ability to generate gradients of proteins, surface properties, and fluid streams containing growth factors, toxin, enzymes, drugs and other important biological molecules are greatly beneficial for biological studies, such as cell-based assays.[23], [24] Microfluidic systems provide an excellent way of generating gradients, as the precise dimensions of microfluidic devices and the understanding of how fluids behave at the micrometer scale provide unique advantages over traditional methods, such as increased throughput and reduced cost.[24] Steady-state microfluidic gradient generators are typically based on two different strategies. Gradients can be accomplished through laminar flow streams or diffusion from a concentrated source. The latter strategy, diffusion from a concentrated source, uses a variety of means to minimize or eliminate convection that can prevent gradient formation or destabilize existing gradients, namely using high flow resistive elements, such as hydrogels, and, since there is nearly no fluid flow, biomolecule mass transport is done through diffusion, and hence the name of the strategy. Laminar flow based gradient generators exploit the lack of convective mixing that occurs between adjacent fluid streams under laminar flow, and are capable of forming gradients for long periods of time, only limited by the flow of reagents. In these gradients, it is possible, by carefully choosing the initial inlet concentrations and the manner in which they are combined, to define specific concentration ranges.[24]

In this work, an example of the gradient generator used is depicted in Figure 1-10.

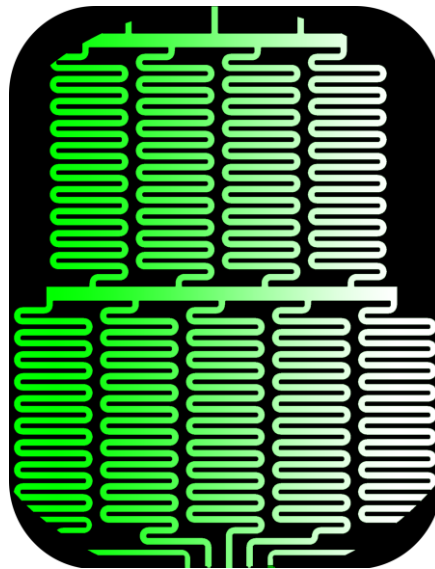


Figure 1-10 A microfluidic laminar flow based gradient generator. The gradient goes from left to right with three different concentrations flowed. The higher concentrations of the fluorescent molecule start from the left.

1.3. Photodiodes

Photodiodes are a powerful tool for microfluidic integration in assays that involve fluorescence or chemiluminescence, and can possibly be used as an alternative to expensive equipments, such as microscopes and imaging equipment. At its most basic level, a photodiode is a semiconductor device capable of turning light into current. The photodiode principle of operation is the internal photoelectric effect. Contrary to the external photoelectric effect, in the internal photoelectric effect, the displaced electron doesn't leave the material and an electron-hole pair is created, both effects are pictured in Figure 1-11. As the photons, with enough energy, are absorbed by the material, the electrons migrate to the conduction band from the valence band and leave electrons holes, which are a theoretical concept of where there is potential for the existence of an electron. The displaced electrons, of negative charge, move towards the cathode, whereas the holes, of positive charge, move to the anode, generating a measurable electric current. [25]

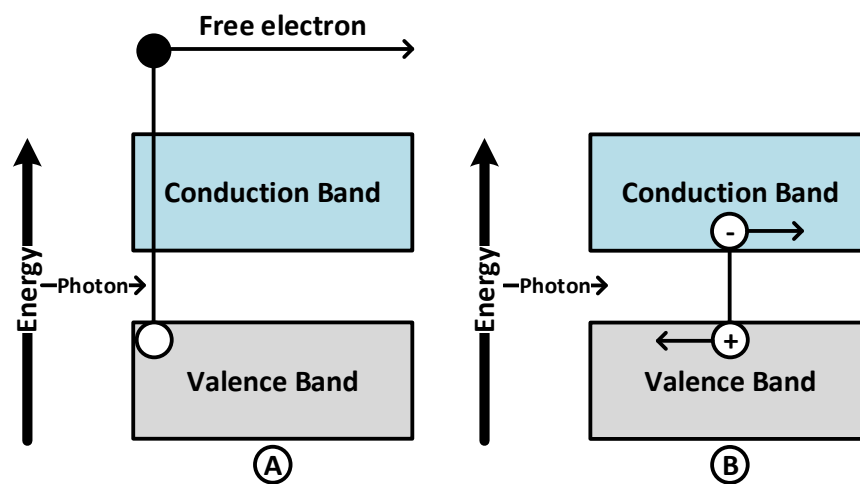


Figure 1-11 Diagram of the photoelectric effect on a semiconductor. (A) External photoelectrical effect. The energy of the photon was enough for the electron to leave the material. (B) Internal photoelectron effect. The energy of the photon excited the electron (- sign) from the valence band to the conduction band of the material, generating an electron hole (+ sign) in the valence band.

1.3.1. p-i-n Photodiodes

The photodiodes used in this work were made of hydrogenated amorphous silicon and of the p-i-n variety, this means that they have three types of semiconductor regions, the p-type, the intrinsic semiconductor region and the n-type. In this type of diode, the intrinsic semiconductor is generally wider than the other regions; in the used photodiodes, the width of the intrinsic layer was 5000 Å, whereas the p and n layers had both 200 Å each.

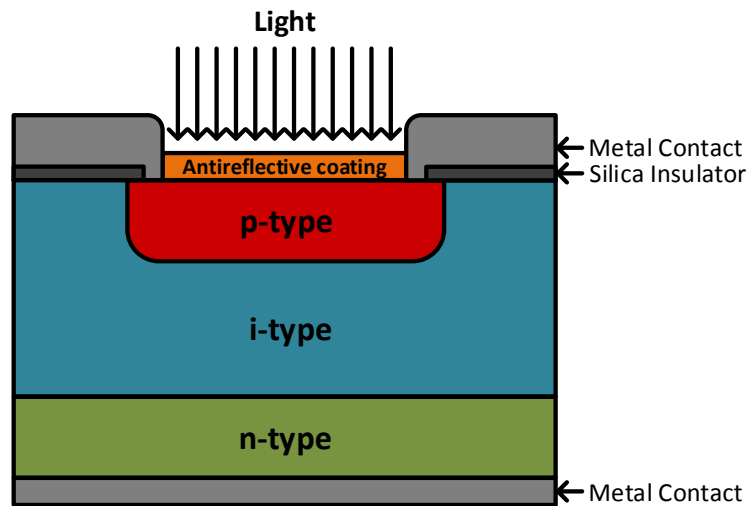


Figure 1-12 Example of a p-i-n photodiode cross section.

In the n-type semiconductor, the n stands for negative charge, as there is a higher concentration of electrons than holes. As opposed to n-type semiconductors, the p-type, with the p standing for positive, has a higher concentration of holes than electrons. Both types, n and p, of semiconductors are extrinsic, meaning that impurities were introduced in a process known as doping, in order to create the difference in electron and hole concentrations. The intrinsic semiconductor region has a balanced distribution of electrons and holes. It is in this region that an electric field is generated, allowing the transportation of both electrons and holes to and from the other layers. The differences in the valence and conduction band of the different regions can be seen in Figure 1-13. For the n-type semiconductor, an intrinsic semiconductor (not doped) is doped with donor impurities (excess electrons), with a common dopant being phosphorus. For the p-type semiconductor, an intrinsic semiconductor or an n-type is doped with acceptor impurities (excess holes), with a common dopant being boron. The intrinsic semiconductor region is made of an undoped intrinsic semiconductor, commonly referred as the i-region of a photodiode.[25]

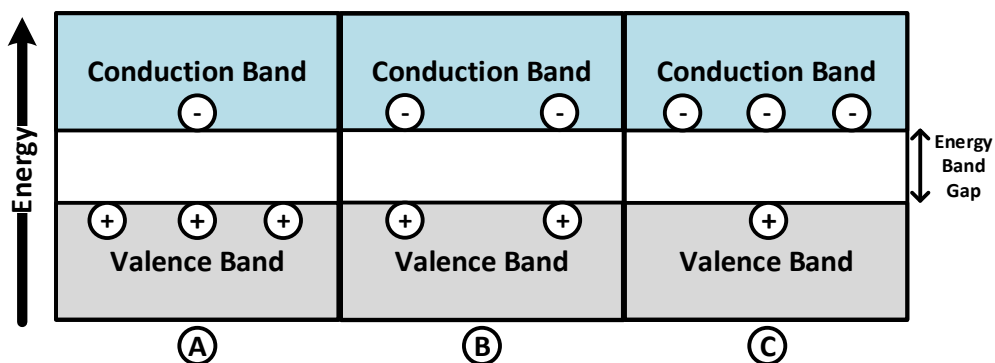


Figure 1-13 Band diagrams of the three different types of semiconductors in p-i-n photodiodes. (A) Band diagram for a p-type semiconductor. (B) Band diagram for an intrinsic photodiode. (C) Band diagram for an n-type semiconductor.

In Figure 1-13, it is possible to observe that the p-type semiconductor has a higher concentration of holes in the valence band than electrons in the conduction band, while the opposite happens in the n-type semiconductor. The intrinsic semiconductor has a balanced concentration of both electrons and holes.

In order for the p-i-n device to work as a photodiode, it needs to work in reverse bias. In this operation mode, a positive voltage is applied to the n-region, causing an electric field in the intrinsic layer to go in the n - p direction, as seen in Figure 1-14. This way when a photon impinges on the depletion layer, in this case the intrinsic semiconductor, and electron-hole pair is created and go in opposite directions due to the electric field, the electrons go to the n direction due to lower energy levels and holes to in the p direction, generating current that can then be measured in an ammeter.

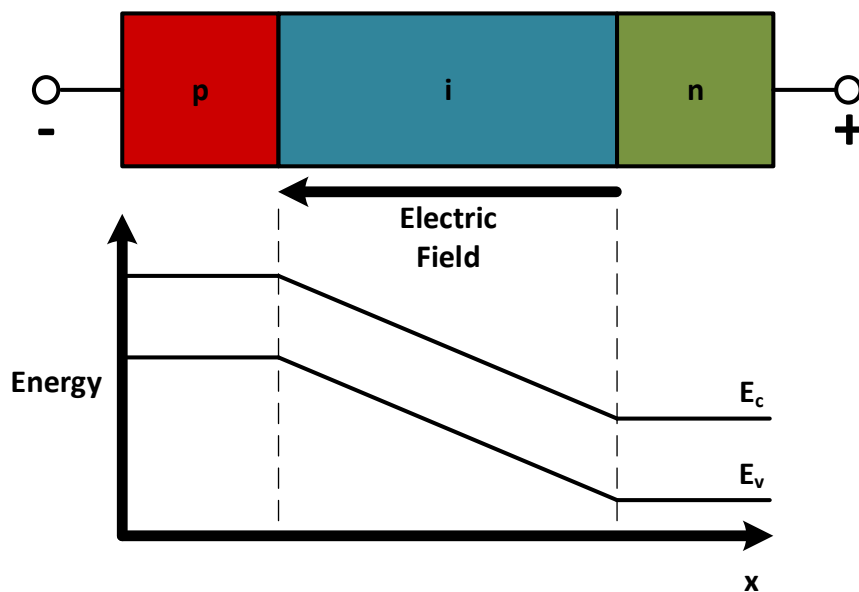


Figure 1-14 p-i-n photodiode working in reverse bias.

1.3.2. Amorphous Silicon Photodiodes Integration

The photodiodes used will be made of hydrogenated amorphous silicon (a-Si:H). To date, hydrogenated amorphous silicon photodiodes have been used for a variety of different applications, ranging from the detection of chemiluminescent molecules, such as horseradish peroxidase (HRP), for the quantification of proteins or DNA, to the quantification of molecules labeled with fluorescent probes and quantum dots.[26]–[33] Hydrogenated amorphous silicon photodiodes are a good choice for integrated optoelectronic detection of biomolecules in microarray and LOC applications. They have a high quantum efficiency in the visible, low dark current and low-temperature processing technology, below 250°C, which enables their usage with substrates such as glass and polymers.[29]

1.4. Objectives

Microfluidic live cell assays with integrated detection using photodiodes have the potential to perform high-throughput GPCR screening while simultaneously using smaller volumes of expensive solutions and requiring less expensive equipment. So, the main objective of this work is to contribute towards the improvement of microfluidic live cell GPCR screening assays with integrated photodiode detection. A secondary objective is the creation of a single cell hydrodynamic trapping microfluidic channel with integrated gradient generation as a tool for multiplexing GPCR screening assays with live cells.

This work was divided into three main parts: Macroscale, Microscale and Photodiodes. The macroscale part was a benchmarking set of experiments, using traditional tools for the screening of GPCR targeting drugs. The microscale part comprised of the characterization of a pre-existent microfluidic chamber channel as a tool for screening of GPCR drug targets in live cells and the adaptation of a gradient generator channel with integrated hydrodynamic single cell trapping as a multiplexing platform for the analysis of single cell variance in a population. The photodiode part consisted in the characterization of $200 \times 200 \mu\text{m}^2$ a-Si-H photodiodes and its integration in the microfluidic chamber channel.

Materials and Methods

2.1. Animal Cell Culture

The animal cell line used for the live cell calcium assays was Human Embryonic Kidney (HEK) 293T. The handling of the cells was performed in sterile conditions to prevent microbial and fungal contamination. The HEK 293T cells used for the live cell calcium assays were obtained from working cell banks (3×10^6 cells preserved at -80°C) by thawing followed by DMSO removal, seeding in T75 cell culture flasks using Dulbecco's Modified Eagle's medium (DMEM) supplemented with 10% fetal bovine serum (FBS) and 1% antibiotic-antimycotic solution (penicillin, streptomycin and Fungizone®) and incubation at 37°C in a 5% CO_2 atmosphere until reaching a confluence of 80% (approximately 4 days). After reaching 80% confluence, the non-adhered cells were removed by washing with PBS and the adhered cells detached by incubation, for 3 min, with a solution of trypsin-0.05% EDTA. The cells were then passed to another platform for assaying or to a culture flask (T25 or T75) at an initial density between 0.15×10^6 cells/mL and 0.3×10^6 cells/mL, and then grown for 24-48 hours under the same conditions. The number of cells and their viability was periodically checked before passage using Trypan Blue Dye. After about 20 passages, the cell culture was discontinued and another one obtained from the frozen working cell banks.

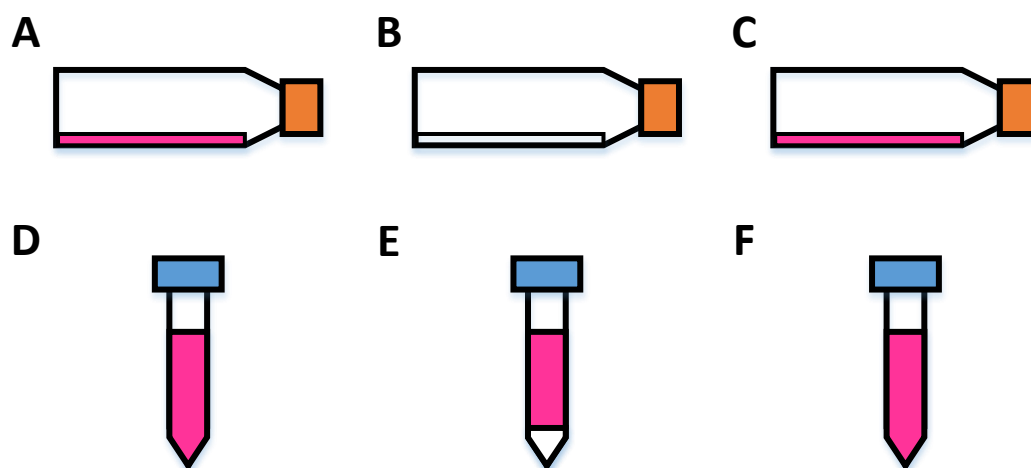


Figure 2-1 Schematics of the cell harvesting process. (A) The cells are in a T-flask. (B) The cell medium is removed and the T-flask filled with PBS. (C) The PBS is removed and Trypsin-EDTA added to the T-flask. (D) After the T-flask with Trypsin-EDTA is removed from the incubator, cell medium is added and the flask contents transferred to a tube. (E) The contents of the tube are centrifuged, with the cells forming a pellet. (F) The pellet is re-suspended and ready for use in assays or for a passage to another T-flask.

2.2. Microtiter Plate Live Cell Calcium Assays

HEK293T cells were transferred to microtiter plates (Becton-Dickinson) at an initial cell density of 0.15×10^6 cells/ml and incubated for 24 h at 37°C in a 5% CO_2 atmosphere, using DMEM with 10% FBS and 1% AntiAnti in a total volume of 100 μL per well. The adhered cells were then incubated for 30 minutes at 37°C with 100 μL of Fluo-4 Direct™ prepared in assay buffer (1xHBSS, 20mM HEPES supplemented with 2.5 mM probenecid) and then in the dark for 30 minutes, at room temperature. The compounds to be assayed were prepared fresh and diluted in assay buffer, in a way to achieve the desired concentrations inside the wells, in the range of 10^{-8} - 10^{-4} for UTP and 10^{-8} - 10^{-3} for Suramin. The agonist live cell calcium assays were done on a fluorescence inverted microscope (Olympus CKX41), with the microtiter plates mounted on the microscope stage and the cell baseline fluorescence recorded for 20 s. Then 50 μL of the compounds assayed, concentrated 5 times, were injected using an automated pipette and the change in fluorescence recorded until 180 s elapsed. For the antagonist assays, the cell baseline fluorescence was recorded for 20 s and then 40 μL of the antagonist, concentrated 6 times, added using an automated pipette. The response of the cells to the antagonist was recorded for 60 s and then 40 μL of the agonist, concentrated 7 times, added to the well with the change in fluorescence being recorded until a total of 180 s had passed.

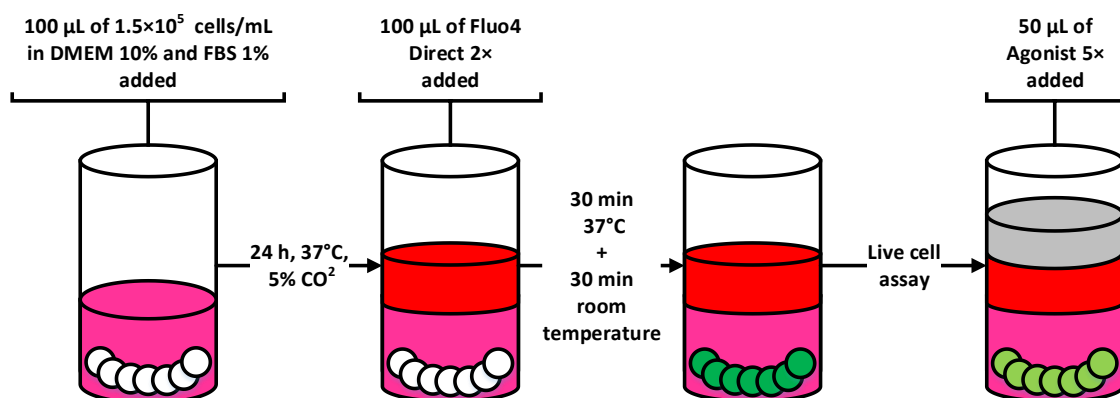


Figure 2-2 Diagram of the agonist fluorescence live cell calcium assays in microtiter plates.

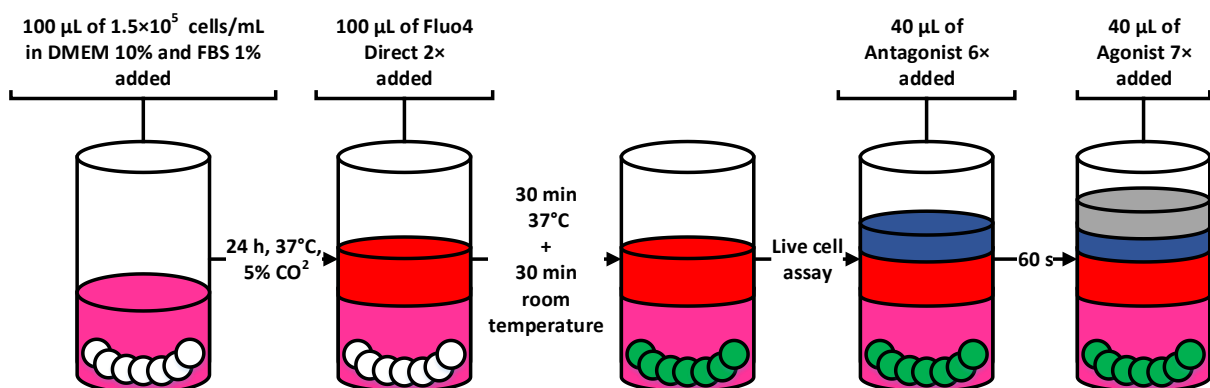


Figure 2-3 Diagram of the antagonist fluorescence live cell calcium assay in microtiter plates.

2.3. Hard Mask Fabrication

The fabrication of the microfluidic structure started with the creation of a 2D design in AutoCAD 2014 software. Initially, a 200 nm thick layer of aluminum was deposited on top of a glass substrate in a Nordiko 7000 magnetron sputtering system. Then, a 1 μm thick positive photoresist layer was spincoated on the aluminum covered glass substrate. The 2D design was then transferred to the photoresist by exposing it at 442 nm using a Heidelberg DWL II direct write laser lithography equipment. After the photoresist was developed, the aluminum was etched using an aluminum etchant standard mix and the remaining photoresist cleared using acetone. This aluminum hard mask patterned with the desired 2D design works as a mask for the fabrication of a SU-8 photoresist mold.

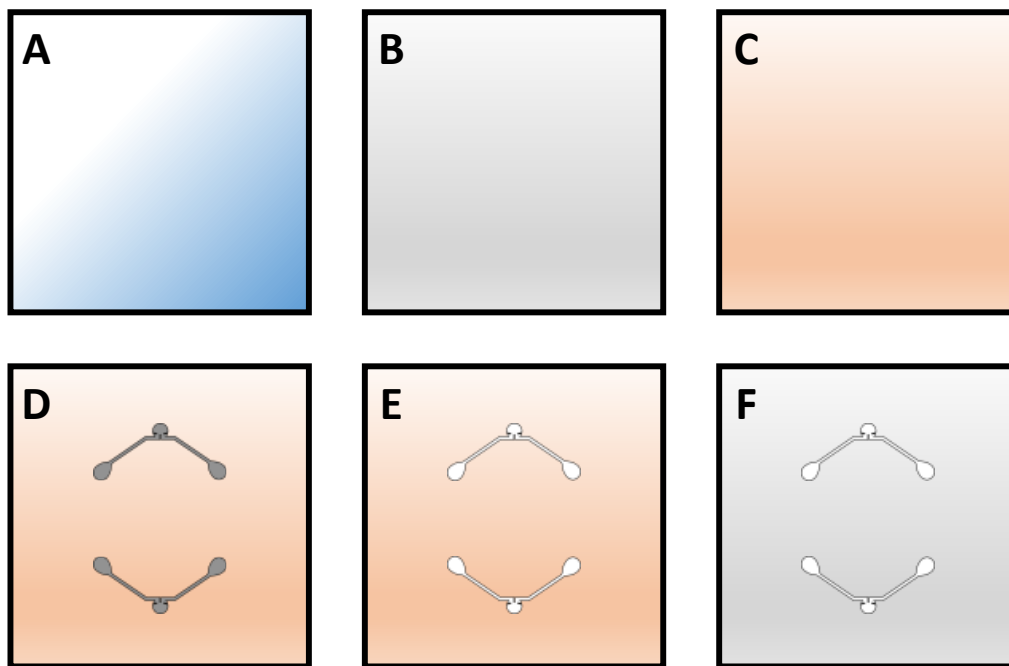


Figure 2-4 Schematics of the hard mask fabrication process. (A) Glass slide. (B) Deposition of aluminum. (C) Photoresist spincoating. (D) Laser lithography and photoresist developing. (E) Aluminum Etching. (F) Remaining photoresist cleared with acetone.

2.4. Mold Fabrication

A silicon substrate was cleaned with acetone followed by an ultra sonicator bath in Alconox® at 65°C for 20 minutes, then rinsed with IPA and distilled water. A SU-8 photoresist layer was spincoated over the cleaned silicon substrate. The photoresist used varied with the desired height of the SU-8 spincoated layer, for a height of 17 μm , SU-8 2015 was used whereas for a height of 60 μm , SU-8 50 was chosen. Both formulations of SU-8 were purchased from Microchem and the spincoater was a Laurel WS-650-23. The SU-8 covered silicon substrate was then pre-baked at 65°C for 3 min, then soft baked at 95°C for 8 min and finally cooled down at room temperature for 5 min. Then, the hard mask, with the desired patterned design, was placed on top of the silicon substrate with the aluminum side facing the SU-8. The SU-8 was then exposed, through the mask, using a UV lamp which induced the hardening of the exposed photoresist. The SU-8 that was not exposed through the mask was removed from the substrate by developing with a 99% solution of PGMEA. The substrate was hard baked at 150°C for 15 min and then the thickness of the SU-8 mold measured in a profilometer (Tencor Alpha-Step 200). The height of the SU-8 layer varied from 15 to 20 μm for the gradient generator structure and from 50 to 60 μm for the microfluidic chamber structure.

For the gradient generator structure, due to the small traps features in the mask, the mold was done directly on the mask, instead of using a silicon substrate the substrate, was the mask itself.

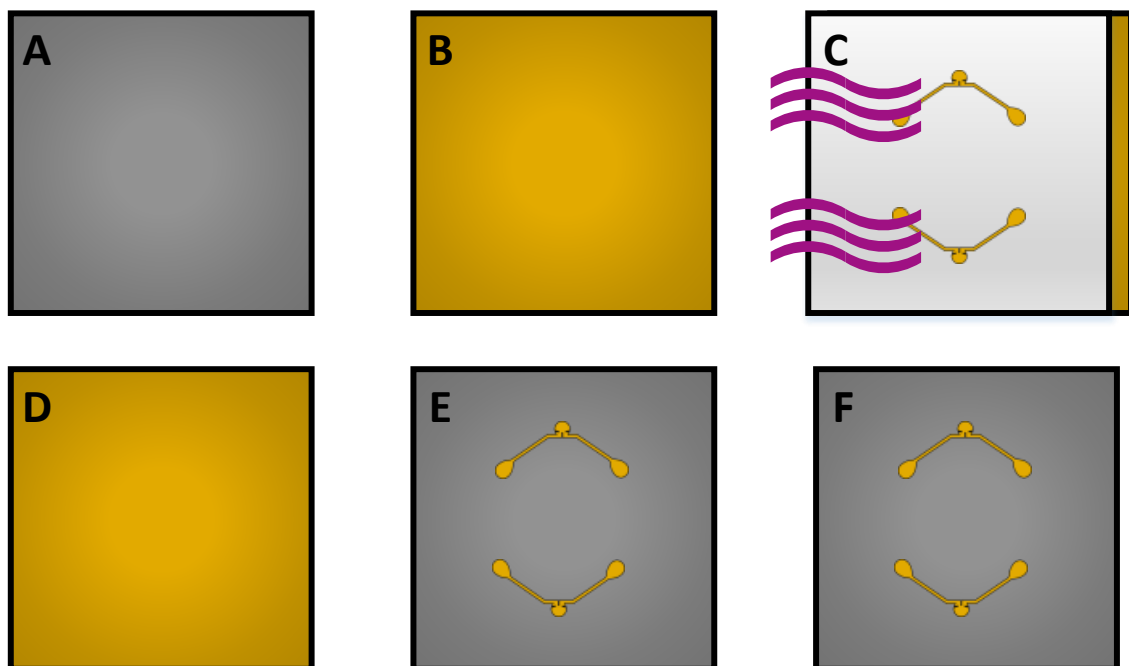


Figure 2-5 Schematics of the mold fabrication process. (A) Clean silicon substrate. (B) SU-8 spincoating. (C) Placing of the hard mask on top of the substrate and exposure to UV light. (D) SU-8 substrate after UV light exposure. (E) Developing of the unexposed SU-8 with PGMEA. (F) Final mold after hard baking at 150 °C for 15 min.

2.5. PDMS Fabrication

PDMS (SYLGARD 184 silicon elastomer kit) was prepared by mixing the base monomer with 10:1 parts curing agent and degassed in a vacuum chamber. The degassed PDMS was poured over the SU-8 mold and cured in an oven at 70°C for 90-120 min, and then peeled off from the mold. The inlet and outlet holes of the structure were done on the PDMS using a 20 ga syringe needle from Instech Solomon. A glass slide was cleaned in a solution of Alconox® for 20 min and then for 5 min in a solution of IPA, both steps were done inside an ultra sonicator. The PDMS structure was also cleaned with IPA for 5 min inside a sonicator. Both the PDMS structure and the glass were then rinsed with water and dried with compressed air. For the sealing step, the PDMS structure and the glass were then placed inside a UVO-cleaner (Jelight Model 144AX) for 11 min with the area to be sealed upwards. After the 11 min had passed, the glass slide was placed on top of the PDMS structure and pressed to form an irreversible seal. The resulting channels were left for 24h before further usage.

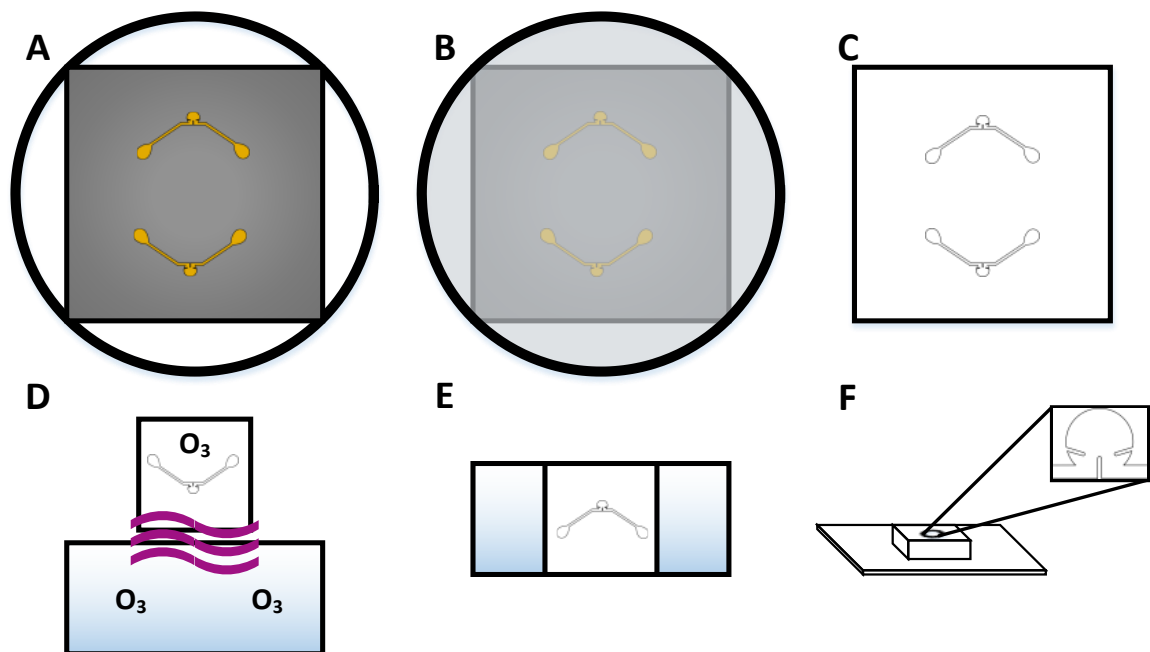


Figure 2-6 Schematics of the PDMS microchannel fabrication process. (A) The mold is placed in a Petri dish. (B) PDMS is poured on top of the mold. (C) After being cured at 70°C for 90-120 min, the PDMS is peeled off the mold. (D) A cleaned glass slide and PDMS, with inlet and outlet holes, are placed inside an UVO cleaner and cleaned with UV radiation and ozone. (E) The PDMS is placed on top of the glass slide and pressed to remove air bubbles. (F) Final channel and close-up of the chamber section.

2.6. Microfluidic live cell calcium assays

2.6.1. Microfluidic Chamber

The microfluidic channels were functionalized with ethanol and left overnight at 4°C to remove air bubbles. The channels were then washed with water followed by incubation with Fibronectin (100 µg/mL in H₂O) for 2 hours at 37 °C. For the insertion of HEK293T cells, a concentration of 3×10⁶ cells/mL in DMEM were inserted into the microchannel using an infusion pump (KDS Legato 100), the initial flow rate (Q) set to 50 µL/min and after cells were entering the chamber, it was set to 1.5 µL/min in order to control cell placement inside the channel. When a sufficient amount of cells were inside the channel, the flow was stopped. The microfluidic channels with cells were then incubated for 20 min at 37 °C and in a 5% CO₂ atmosphere to allow cell adhesion. Afterwards, DMEM was flowed inside the channel at Q=2 µL/min for 10 min to wash out cell debris and provide fresh cell medium to the cells, followed by a 30 min incubation step at 37 °C to allow the cells to adhere to the channel. Then, 250 µL of Fluo-4 Direct™ prepared in assay buffer (1×HBSS, 20mM HEPES supplemented with 2.5 mM probenecid) were mixed with 750 µL DMEM with 10% FBS and 1% AntiAnti in an Eppendorf and then flowed inside the channel at a Q=1.25 µL/min until 8 µL had been inserted. The cells were then incubated for 30 min at 37 °C and afterwards for 30 min in the dark at room temperature. UTP was then injected into the channels (Q=1.25 µL/min) and the P2Y₂ GPCR activation was monitored in real-time using fluorescence microscopy. The microscope used was an Olympus (CKX41), the exposure time was set to 1 s and the gain to 12.

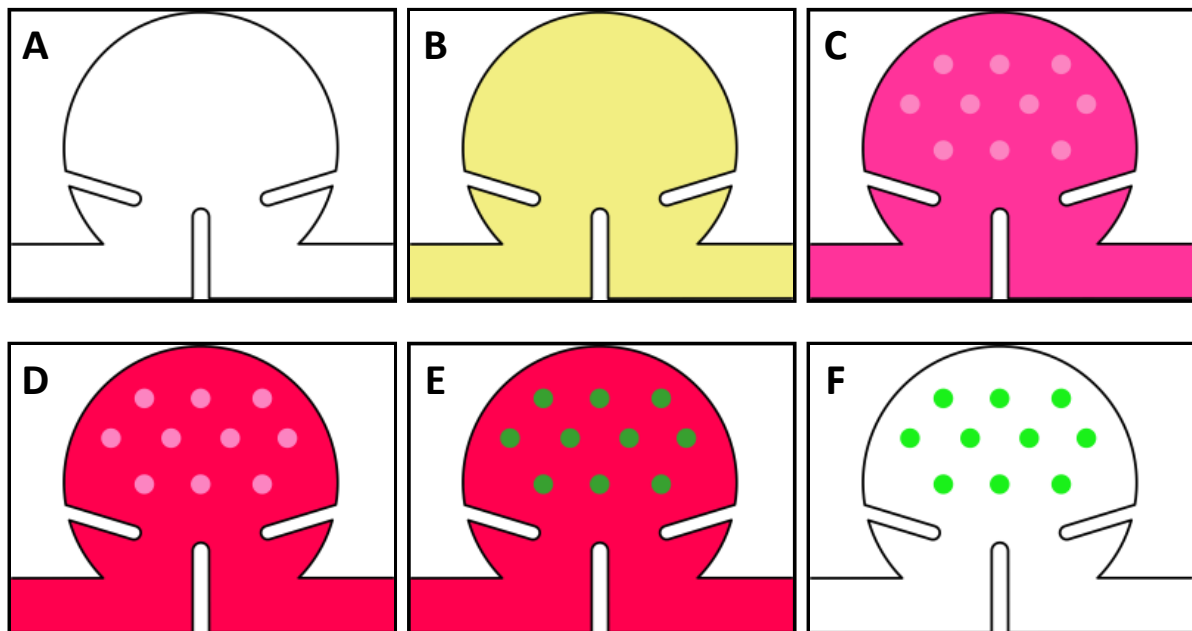


Figure 2-7 Diagram of the fluorescence live cell calcium assay in a microfluidic channel. (A) Channel filled with water after being cleaned with ethanol. (B) Incubation with fibronectin. (C) Cell insertion into the channel and washing with medium. (D) Incubation with Fluo4 Direct. (E) Cells become fluorescent after 30 min at 37°C + 30 min at room temperature. (F) Cell response to the compound assayed.

2.6.2. Microfluidic Gradient Generator

For the microfluidic live calcium cell assay using the gradient generator channel, the channel was filled with cell medium using a flow rate of 0.5 $\mu\text{L}/\text{min}$ for 10 min, and incubated for 2h at 37°C and in a 5% CO_2 atmosphere. The cells were inserted at a concentration of 0.75×10^6 to 1.5×10^6 cells/mL using a flow rate of first 2 $\mu\text{L}/\text{min}$ then, after the cells were flowing inside channel, the flow rate was lowered to 250 nL/min and the insertion continued until the desired amount of cells was in the traps. The cells in the channel were incubated for 20 min at 37°C, and then Fluo4 (solution with $\frac{1}{4}$ Fluo4 Direct and $\frac{3}{4}$ cell medium) flowed at $Q=0.5 \mu\text{L}/\text{min}$ for 10 min. Afterwards, the cells were incubated for 30 min at 37°C and then for 30 min in the dark, at room temperature. Three different concentrations of UTP were prepared, put in syringes and connected to the inlets as shown in Figure 2-9. The flow rate used for the UTP assay was 0.5 $\mu\text{L}/\text{min}$. The assay was recorded using CellSens software in an Olympus inverted microscope using an exposure time of 1 s and 12 gain.

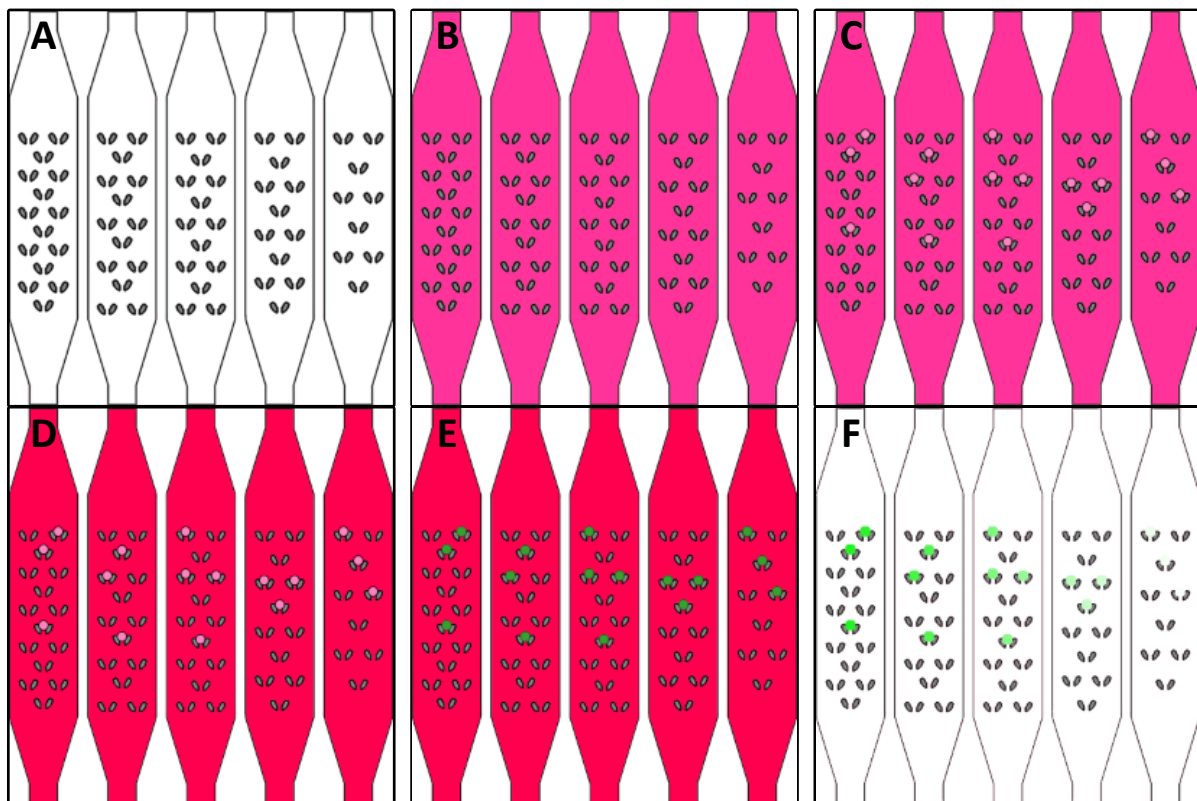


Figure 2-8 Diagram of a live cell calcium assay using the gradient generator channel. (A) The channel was functionalized with ethanol and then washed with water. (B) The channel was filled with cell medium. (C) Cells were inserted with some getting stuck on the traps. (D) Fluo4 Direct™ was put inside the channel. (E) After two incubation steps, the cells are fluorescent. (F) The cells respond to the drug.

2.7. Gradient Generation with Calcium Solutions

The gradient generator channel was functionalized with ethanol and left overnight at 4°C to remove air bubbles. The channel was then cleaned with water. Both steps were done using the same materials as the microfluidic live cell assay at a flow rate of 0.5 μL for 10 minutes. For the gradient generation with calcium solutions, Calcium Calibration Buffer Kit #1, purchased from Life Technologies, was used to prepare solutions with different concentrations of calcium, by mixing CaEGTA with K₂EGTA buffer. EGTA (ethylene glycol tetraacetic acid) is a chelating agent. Three different concentrations of calcium were prepared in eppendorfs, with each totaling 250 μL . Then 2 μL of 1mM Fluo4 pentapotassium salt solution, purchased from Life Technologies, were added to each eppendorf so that the final Fluo4 concentration in each solution equalled 4 μM . The solutions were then put on three different 1ml syringes, purchased from Codan, on a support that enables the simultaneous pumping of three solutions at the same time, and then the tubing connected to the adapters on the channels. In Figure 2-9 is the visual representation of the support and channel inlets.

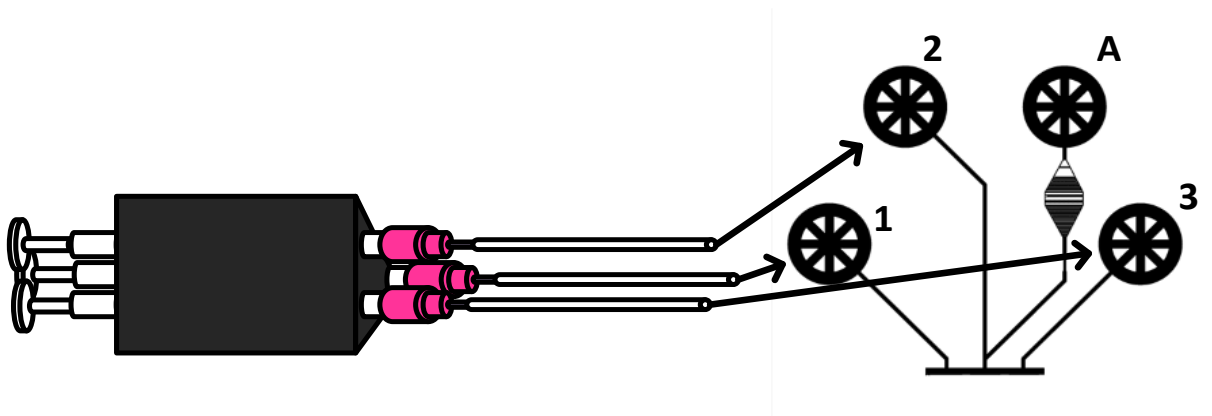


Figure 2-9 Diagram of a gradient generator experiment. On the left, the support and three syringes with different concentrations are represented. On the right, the inlets of the gradient generator are represented. Only inlets 1,2 and 3 were used to form a gradient.

To have a gradient that started from the right, meaning more intense from the right to the left channels, the syringe with the highest concentration of CaEGTA was connected to inlet 1 (Figure 2-9), then the syringe with the middle concentration to inlet 2 and then the syringe with the lowest concentration to inlet 3. If the desired gradient was more intense from the left to the right, the connections were inverted. After the syringes were connected to the inlets, the infusion pump (New Era NE300) was turned on and the flow rate set to 0.5 $\mu\text{L}/\text{min}$. Images of the trap area of the gradient generator were taken every 15 minutes or a video recorded to determine the needed time for the gradient to form. The photos or videos were made using CellSens software in an Olympus microscope, with the gain set for 12 and exposure time of 5s for the video recordings and 1s for the photos.

2.8. Video and Data Analysis

The videos of the cell response in the live cell calcium assays were obtained using Olympus (CKX41) companion software CellSens, which outputs uncompressed AVI files. The videos were recorded with exposure time of 1 s, 12 gain and in gray scale, with the latter setting used to lower the size of the video files. The uncompressed AVI files were imported to the free ImageJ software with the MBF (ImageJ for Microscopy) Plugin Collection which enables the analysis of video as image stacks. The videos were converted to gray scale 8 bit image stacks, with the scale ranging between 0 (black pixel) and 255 (white pixel). Each stack was measured using two approaches, removing and not removing the background. The approach where the background was removed only takes in account the area occupied by the cells, not counting with the black space between them, whereas the approach where the background is not removed analyzed the whole area of each slice of the stack, including black space between the cells. In each approach, the average gray scale intensity of each slice of a stack was measured, with each slice of the stack representing 1 s of the video. The data of each assay was normalized to its baseline, which was defined as the average of the first 10-20 seconds of the video (before the drug was injected or flowed). The normalized values represent a percentage of increase from the baseline value, as represented in Equation 2.

$$\text{Normalized Value} = \frac{\text{Initial Value} - \text{Baseline Value}}{\text{Baseline Value}} \times 100 \quad \text{Equation 2}$$

Then, the maximum normalized value for each assay was extracted, and the maximum of the normalized maximums, accounting for the highest concentration assayed for the agonist and lowest for the antagonist, was normalized to 100%. Using GraphPad Prism® software, a Hill dose-response curve was plotted, using Equation 3. In this equation, y is the % of maximum response, x the logarithmic value of a given concentration, p the Hill slope and $EC50$ the effective concentration that generates the half-maximal response.

$$y = \frac{100}{1 + 10^{[(\text{Log}EC50 - x) \times p]}} \times 100 \quad \text{Equation 3}$$

For the antagonist assays, the same software was used and a variation of the Hill dose-response curve plotted, using Equation 4. In this equation the only parameter that changes from Equation 3 is the $EC50$, which is replaced by the $IC50$ that represents the concentration to inhibit 50% of the maximum response.

$$y = \frac{100}{1 + 10^{[(\text{Log}IC50 - x) \times p]}} \times 100 \quad \text{Equation 4}$$

2.9. Photodiode Characterization

The photodiodes used in this work were made of hydrogenated amorphous silicon of the p-i-n variety, with a 5000 Å wide i-region and 200 Å p and n regions. The dimensions of the photodiode were 200 by 200 μm and the photodiodes had an integrated absorption filter (Figure 2-10).

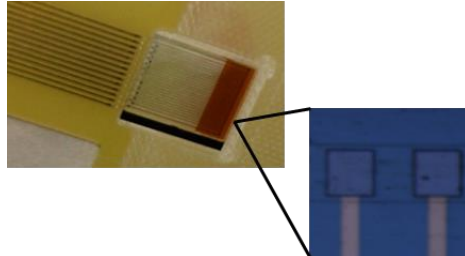


Figure 2-10 Photograph of the photodiodes used. On the left is the real scale photograph of the photodiode area, and on the right is the actual photodiodes, each with a width of 200 μm.

A conventional blue LED with peak emission at 470 nm coupled to a low pass filter with cut-off wavelength of 500 nm (Thorlabs) and a tungsten-halogen lamp (250 W) coupled to a monochromator (McPherson 2035) were used as light sources. 494 and 516 nm were the chosen wavelengths, for the lamp-monochromator combo, because they correspond to the excitation and emission wavelengths, respectively, of the Fluo4 Direct™ fluorophore. The response of the photodiodes to the characterization experiments was obtained using a picoammeter (Keithley 237) operating at room temperature. All the measurements with photodiodes were done on an optical table, as pictured in Figure 2-11.

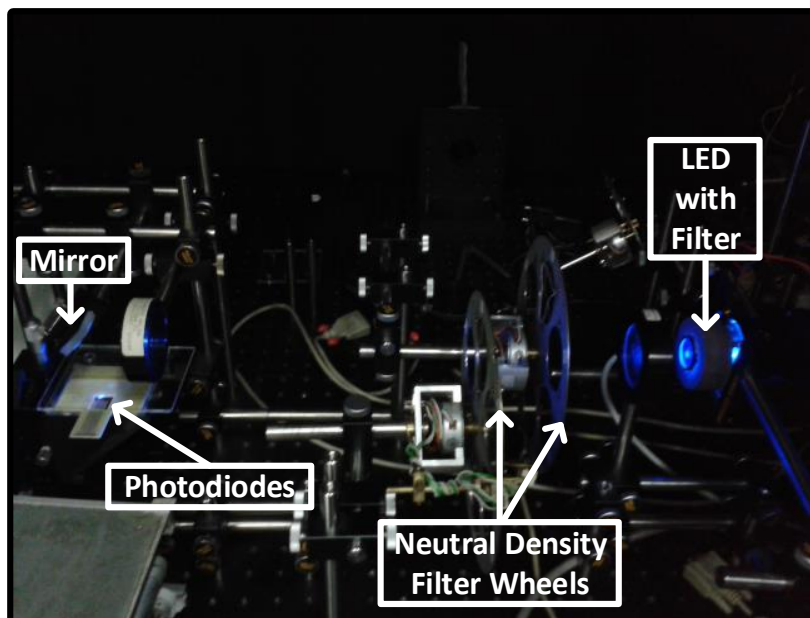


Figure 2-11 Optical table setup with the components used for the photodiode characterization.

For the experiments with the LED, a support was created using 3D prototyping software (SolidWorks) in order to have the LED and the low pass coupled as a unit. This created prototype was then printed in a 3D printer (Witbox). The schematics are on the Appendix Section f.

The first experiment done was the determination of the photon fluxes for the light sources used. For this, a calibrated crystalline silicon photodiode (Hamamatsu S1226-5BQ) was used and the current measured for the wavelengths of 494 and 516 nm of the lamp-monochromator combo and the LED with and without low pass filter. Using the calibrated values of the Hamamatsu photodiode in Table A.2 of the Appendix section, the photon flux (Φ) was calculated using Equation 5.

$$\Phi(\lambda) = \frac{I(\lambda) \times \lambda}{A \times S(\lambda) \times c \times h} \quad \text{Equation 5}$$

In this equation $I(\lambda)$ is the current at a given wavelength, λ the wavelength, A the surface area of the photodiode, c the speed of light, h the Planck's constant and $S(\lambda)$ is the responsiveness of the calibrated crystalline silicon photodiode. The Current vs Voltage of the photodiode was also analyzed using the lamp coupled to the monochromator (set to 494 and 516 nm) and the LED with and without filter, setting a range of voltages from -1 to 0 in 0.1 V steps. In this characterization step, a measurement in the dark was also done. It is important to note that all current measurements were converted to current density, by dividing the current obtained by the area of the photodiode (0.0004 cm²). The characterization of the integrated fluorescence filter and photodiode was also performed, with respect to the suitable wavelengths. For this, an external quantum efficiency (EQE) vs. wavelength graph was plotted. The lamp-monochromator combo was used for this experiment. The current for different wavelengths was measured, starting at 600 nm and decreasing to 400 nm with a step of 5 nm. For the calculation of the EQE, Equation 6 was used.

$$\text{EQE} = \frac{J}{\Phi \times q} \quad \text{Equation 6}$$

In this equation, J is the current density in A per sq.cm and q is the electron charge. Using neutral density filters to cut the intensity of the incoming light from the LED or lamp-monochromator combo, the characterization of the response of the photodiodes to different light intensities at the same wavelength was performed. The neutral density filters used ranged from cutting 1000-10 times the original intensity. At the end, a graph with a plot of the current density (J) vs the photon flux (Φ) was obtained for the LED, LED with filter, 494 nm and 516 nm.

A calibrated fluorescent calcium experiment was also performed using CaEGTA solutions mixed with K₂EGTA and Fluo4 Pentapotassium Salt, purchased from Invitrogen. The solutions at different concentrations were inserted into the microfluidic chamber channel and the fluorescence intensity first measured using an Olympus microscope. Then the microchannels were transported to the optical table

and aligned to a working photodiode. Then, after channel alignment, the light source was also aligned to the channel, so that it was directly on top of it. The room light was shut down and the measurement done in the dark, except for the experiment light source, using the picoammeter. An experiment was also done with HEK293T cells inside microchannels. In this experiment, the protocol was the same for the microfluidic live cell calcium assay in the microfluidic chamber channel, but instead of using an Olympus microscope to record a video, the channel was placed on top of the photodiode and the current measured during the assay duration.

3. Results and Discussion

3.1. Macroscale

As a starting point towards the characterization of GPCRs in microfluidic devices, the response of a GPCR, the P2Y2 receptor, was characterized using the traditional macroscale platform, microtiter plates, using HEK293T. HEK293T was the chosen cell type because they are an adherent cell type which can be robustly assayed, have an average doubling time of less than 24h and are commonly used in GPCR characterization assays, normally with the receptor to be characterized overexpressed. Additionally, they are easy to culture, to maintain, and to passage and, since P2Y2 is produced endogenously in HEK293T, there is no need to overexpress the receptor. Also, previous studies had been done on GPCR activation with HEK cells, and the protocol was already optimized for microtiter plate assays. The GPCR chosen to be targeted was the P2Y2 receptor because one of the second messengers in the associated signaling cascade is cytosolic calcium which can be assayed easily with established protocols. Another reason was the existence of literature for the characterization of this receptor at macroscale, but not at microscale. Fluo4 Direct™ was the chosen dye for the calcium assays because it is specially made for GPCR assays involving the release of intracellular calcium in high throughput platforms. It has important features for this type of assays, such as its compatibility with media containing serum, its homogeneity and its large assay window, as it reduces background and has high cell fluorescence intensity (Figure 3-1).

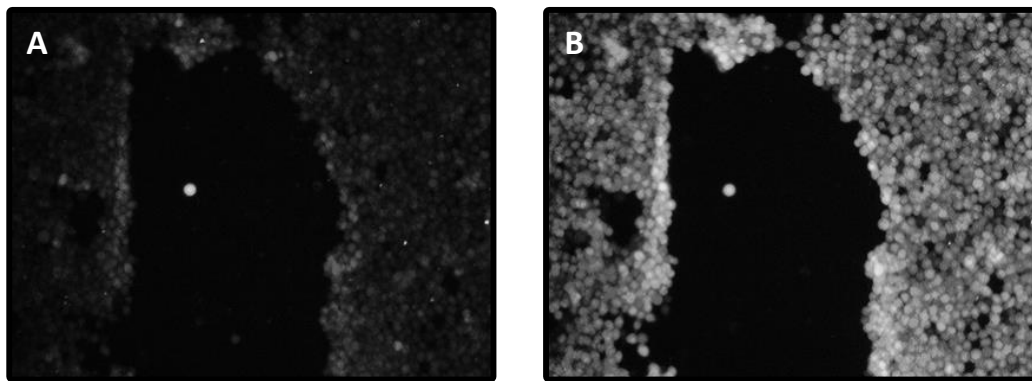


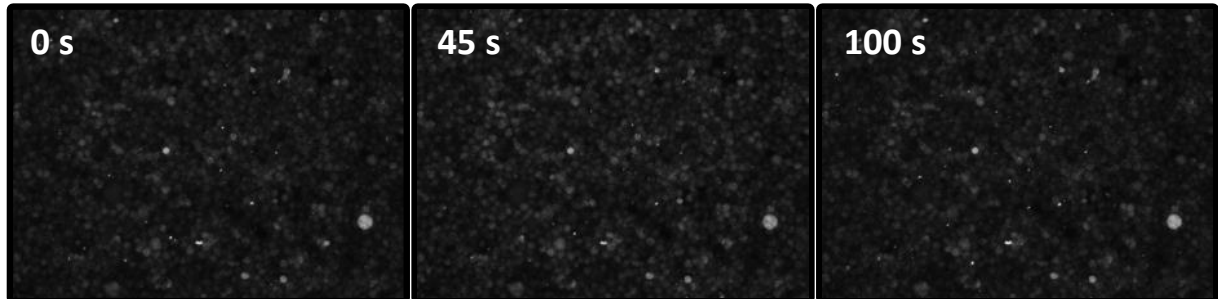
Figure 3-1 Contrast between the background and cell fluorescence using Fluo4 Direct™. The images shown are grey scale fluorescence images. (A) Initial cell fluorescence, before adding UTP (B) Increased cell fluorescence after adding 100 μM of UTP.

3.1.1. Agonist Assays

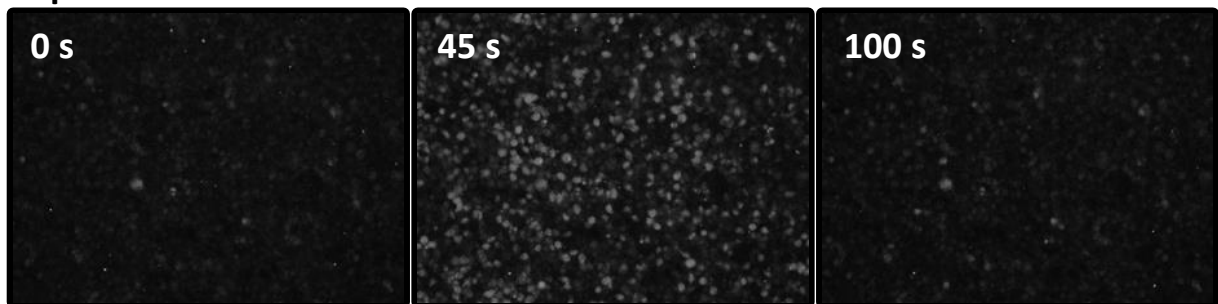
The characterization of the response of the P2Y2 GPCR in HEK293T cells to the agonist UTP was done in microtiter plates using an inverted fluorescence microscope. In the agonist live cell assays in microtiter plates using Fluo4 Direct™, the intracellular calcium concentration was monitored over time. In the first 20 s of the assay, the baseline calcium fluorescence of the cells was recorded, then UTP was introduced into the microtiter plate to activate the P2Y2 receptor. When UTP was added to the well plates, the cells

responded by releasing intracellular calcium which translated into increased fluorescence, as seen in the second and third row of pictures of Figure 3-2. However, when just assay buffer without UTP was added, the cells didn't respond significantly, as pictured in the first row of images of Figure 3-2.

0 μM UTP



2 μM UTP



150 μM UTP

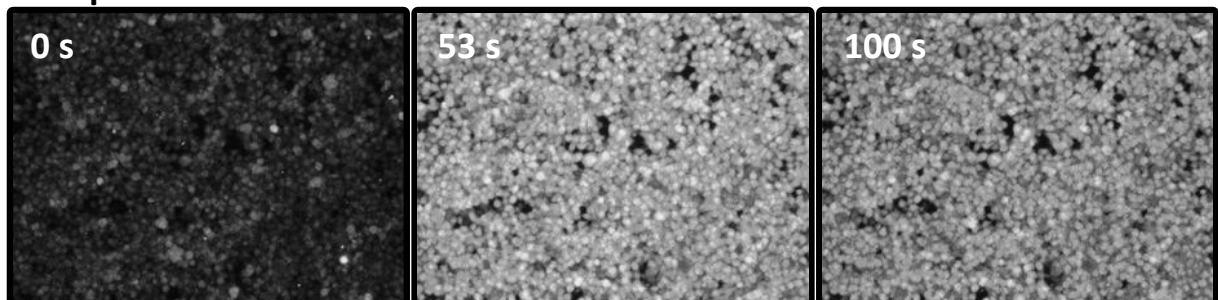


Figure 3-2 Cell response to different UTP concentrations at similar time points in well plates. The first column of pictures was taken at the beginning of the assay, then, after 20 s the concentrations of UTP displayed in each row were added. The second picture in each row was taken when maximum fluorescence was reached. The last picture in each row was taken at the end of the assay, after 100 s. This image is in greyscale.

In Figure 3-2, it is possible to observe that the response of cells was higher when a concentration of 150 μM was used, compared to 2 μM as the cells were not as fluorescent at the halfway time point, indicating that not as much calcium was released into the cytosol. Also, when no UTP was present, only assay buffer used, the cells didn't respond, meaning that it was the UTP that triggered the release of calcium inside the cells. It is also noticeable that in the 2 μM assay, the pictures at time points 0 and 100 s are very similar, indicating that the intracellular calcium concentration returns to its basal level. That was not

apparent for the 150 μM UTP concentration, indicating that when higher concentrations of calcium are released inside the cell, the longer time it takes for the intracellular calcium to return to a pre-activation level. The pictures in Figure 3-2 only provide a qualitative observation, in order to quantify and compare all the UTP concentrations assayed, the assay videos were analyzed in ImageJ software and the fluorescence normalized to the baseline of each assay, consisting of the first 20 seconds of each video. This normalization is needed because the baseline cell fluorescence varies from well to well, as can be seen at the beginning of each assay in Figure 3-2. After normalizing, the values obtained represent the percentage of increase in cell fluorescence relative to the baseline of the same assay.

UTP concentrations ranging from 0 to 150 μM were assayed, with the cell fluorescence being monitored for 100 s. The normalized change in fluorescence over time is presented in Figure 3-3.

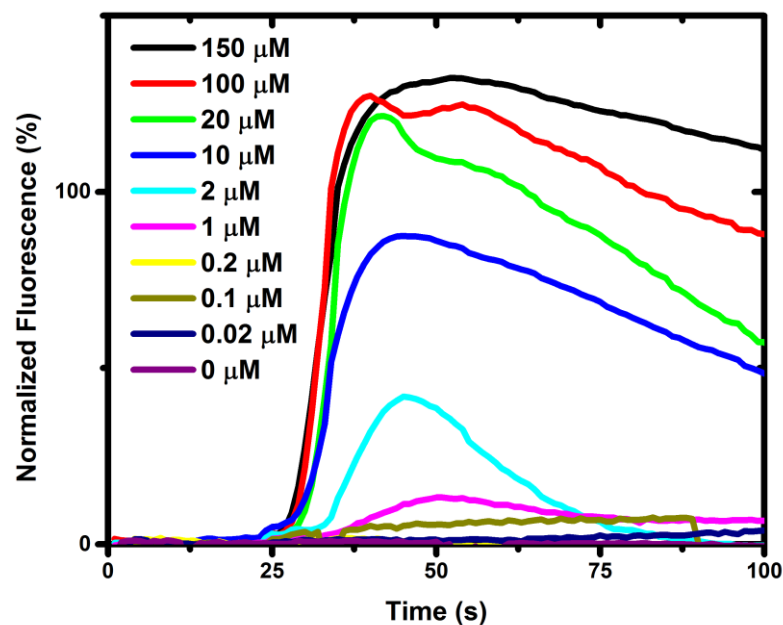


Figure 3-3 Normalized fluorescence vs. time for different UTP concentrations in microtiter plates. For each assay, the different UTP solutions were added after 20 s from the start.

In Figure 3-3, the higher the UTP concentration, the higher the normalized cell response to the drug; however, for the 20, 100, 150 μM assays the maximum fluorescence doesn't seem to vary much, as compared to lower concentrations. This fact may be explained by the P2Y2 receptor being saturated with the drug, and so by increasing the agonist concentration, there is no greater release of calcium after a point, due to the activation of all the existing receptors. In this picture it is also possible to see that for the higher concentrations, after 100 s, the initial basal calcium concentration is not reached, but for concentrations lower than 10 μM it had. This falls in line with what was also observed in Figure 3-2, that the higher the concentration, the longer it takes for the intracellular calcium concentration to return to its pre-GPCR activation levels. It is also worth mentioning that the cell response time was similar for

all the UTP concentrations assayed, ranging from 5 to 10 seconds after adding UTP, meaning that it is mostly independent of concentration.

As it was assumed that the P2Y2 receptor was saturated when a concentration of 150 μM was used, the value of fluorescence obtained for this concentration was normalized to 100%, since it accounts for the maximum cell fluorescence achieved among all the assays performed. After doing this normalization, a Hill dose-response was plotted (Figure 3-4).

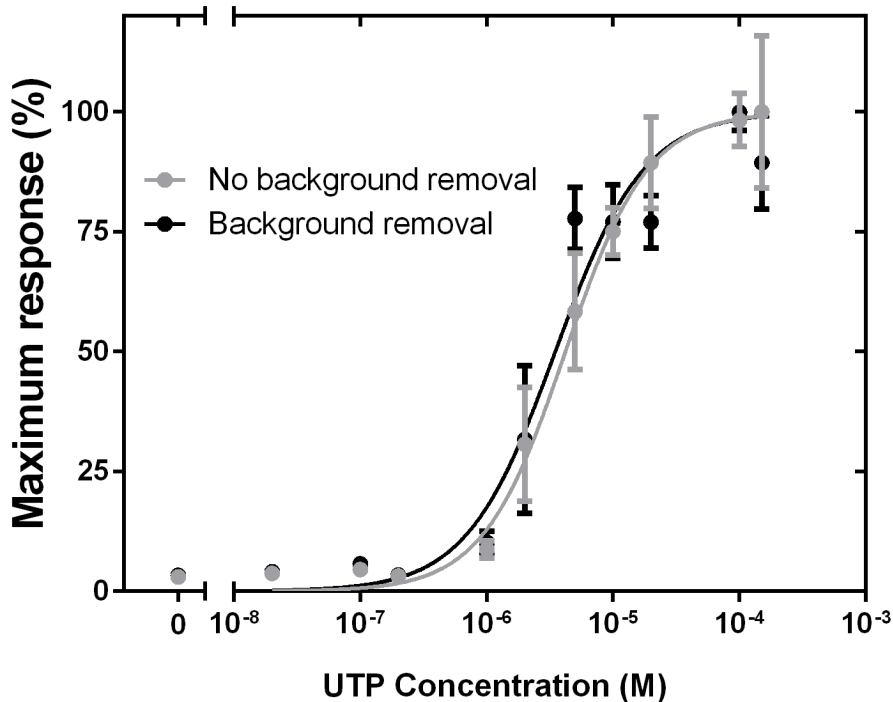


Figure 3-4 Hill dose-response curve for UTP in microtiter plates. The two sets of points represent the same experiments but using different software analysis methods, one where the background of the well plate was removed and another where it was not. Each point in this graph corresponds to a single UTP concentration, and is an average of separate experiments. The error bars of each point represent the standard error of the mean (SEM). The EC₅₀ (the concentration that produces a response of 50% of the maximum) values for removing and not removing background were 3.5 μM and 4.2 μM , respectively.

In the UTP dose response curve pictured in Figure 3-4, it is possible to see that the graph has three distinct phases. The lower plateau, corresponding to the lower concentrations 0 to 10^{-7} M (0.1 μM), is the phase where there is not a significant increase in response, the exponential phase, where there is a great increase in intracellular calcium release, and the upper plateau, where the receptor is most likely saturated and the response stabilizes. It is possible to notice that, although there is a slight variation between the plot with the background removed and the plot without removal, the EC₅₀ is about the same. Removing the background the EC₅₀ was 3.5 μM , with a 95% confidence interval falling between 2.7 μM and 4.6 μM , whereas without removing background, the EC₅₀ was 4.2 μM , with a 95% confidence interval of 3.4 μM to 5.2 μM . So both methods of analysis are in the same 95% confidence

intervals making the difference not very significant. The removing background method was used because of the microfluidic assays, as removing the background is important, since the concentration of cells is much lower than in microtiter plates.

The assay buffer used to prepare the solutions in the assays of Figure 3-4 had calcium ions. To make sure that the calcium observed inside the cell was not from extracellular origin, but in fact released from the endoplasmic reticulum, an assay buffer without any calcium ions was also tested, with the results in Figure 3-5.

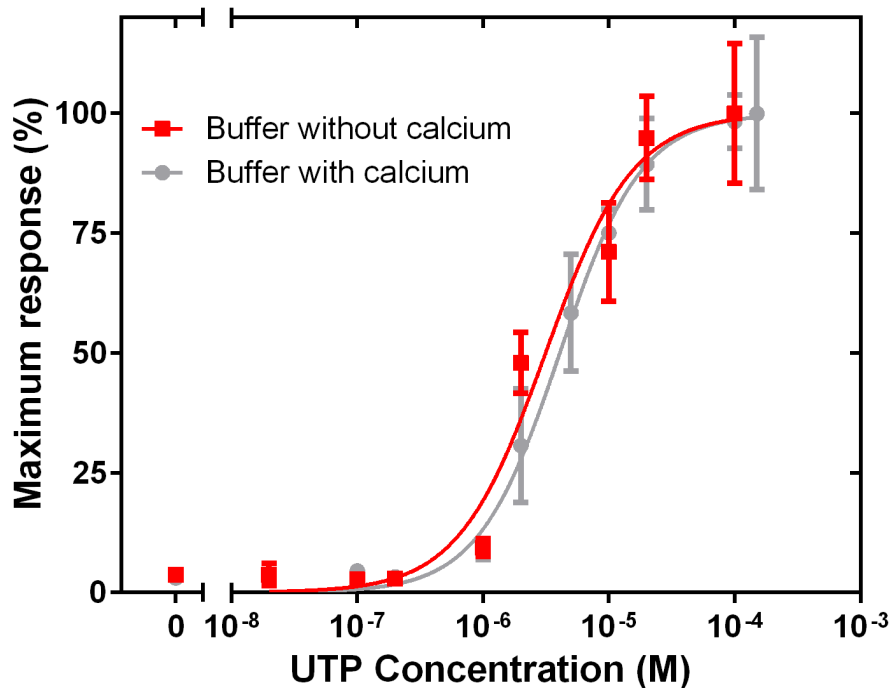


Figure 3-5 UTP dose-response for experiments with and without calcium ions in the assay buffer. The EC50 values for the experiments done with assay buffer with calcium was the same as before, 4.2 μM , and without calcium was 3.1 μM . The method of analysis used for this experiments was without removing background.

There was some difference between the EC50 values for the experiments done with assay buffer with and without calcium ions. It is important to show that the 95% confidence interval for the EC50 of the experiments of assay buffer with calcium was 3.1 μM to 5.4 μM and for the assay buffer without calcium was 2.2 μM to 4.5 μM . Even though the usage of calcium or not in the assay buffer may have some effect on the fluorescence of the cells, statistically the difference is not very significant.

Table 3.1 EC50 values and its 95% confidence intervals for different combinations of video analysis methods and assay buffer composition.

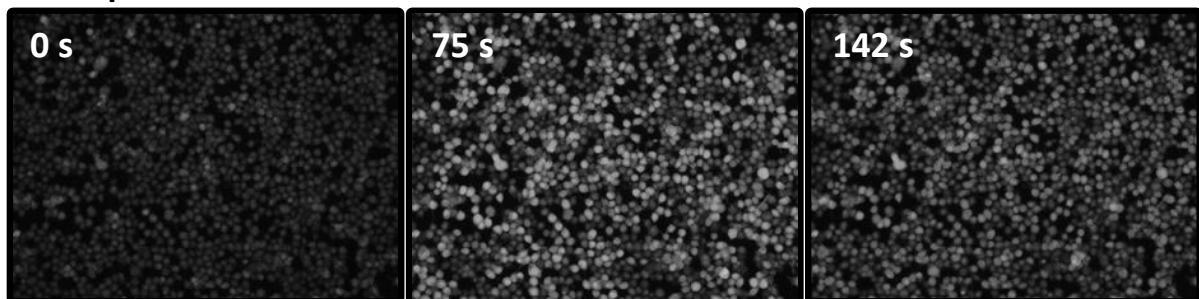
Assay Buffer	Analysis Method	EC50 (μM)	95% Conf. Interval
With Calcium	Background not removed	4.2	3.1 – 5.4
With Calcium	Background removed	3.5	2.7 – 4.6
Without Calcium	Background not removed	3.1	2.2 – 4.5

All the EC50 values in Table 3.1 fall within the range of EC50 values for the activation of P2Y2 receptor with UTP, in literature. [34][35] The values of EC50 obtained fit in the range of 1.5-5.8 μM reported in [34] for murine and human P2Y2, however other studies report an EC50 of 0.14 μM , such as [15].

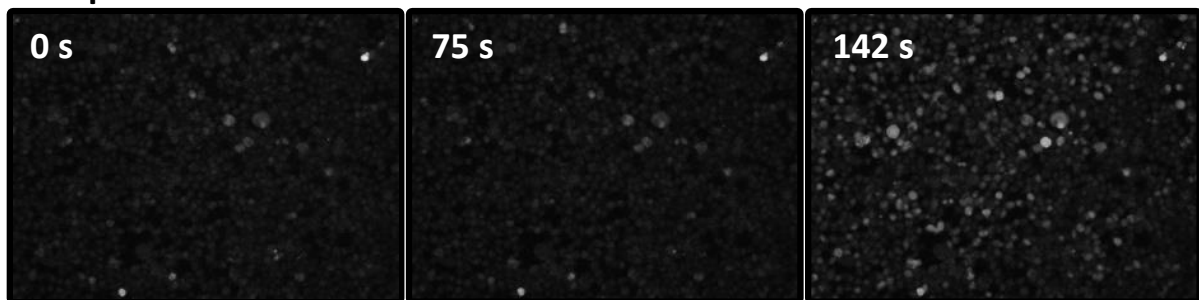
3.1.2. Antagonist Assays

The antagonist used in the assays of this section was suramin. These assays were done in the same conditions as the agonist assays, but first by adding the antagonist and then the agonist. The antagonist was inserted after 20 s from the beginning of the assay, and monitored for 60s. After that time, the agonist was added and the cell response monitored for 100 s, for a total assay time of 180 s. The cells weren't expected to respond to the addition of suramin, because as an antagonist, it should block the P2Y2 receptor binding of UTP and subsequently, prevent the release of calcium. However, for higher concentrations of suramin, the cells had a significant response, as seen in Figure 3-6. The UTP concentration used for every antagonist assay was 10 μM , equivalent to the EC80 (Effective concentration to achieve 80% of maximal response) for the microtiter plate agonist assays.

1500 μM Suramin



750 μM Suramin



0 μM Suramin

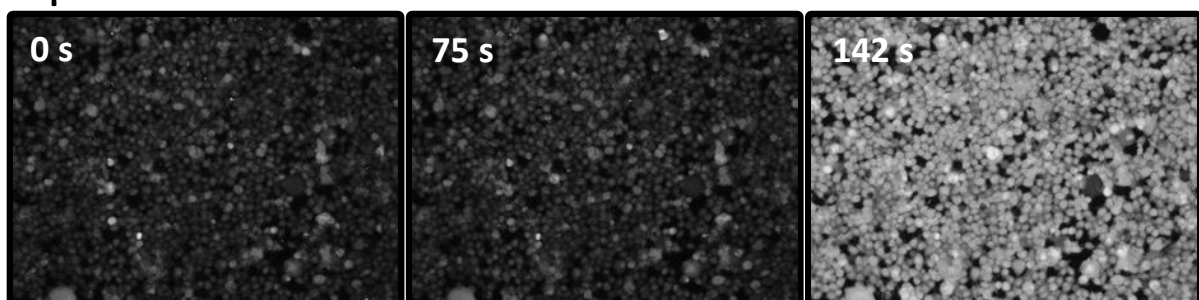


Figure 3-6 Cell response to different concentrations of suramin and a fixed UTP concentration. Suramin was added to the well after 20 seconds and UTP at 80 s. The concentration of UTP added to each well was 10 μM . In the 1500 μM suramin assay, the cells responded before any UTP was added. In the 750 μM suramin assay, the cells responded significantly less to the same UTP concentration than the assay without any suramin.

In Figure 3-6, it is possible to see that high suramin concentrations can cause the release of intracellular calcium, with this effect being enhanced by the presence of calcium on the assay buffer. The response of the cells to suramin was an unexpected result, as in the literature suramin was always depicted as an antagonist to GPCRs that have calcium as a second messenger in the signaling cascade, and never as an agonist or partial agonist. One of the possible explanations to this effect is the large plethora of functions that intracellular calcium can have in cells, not just as a GPCR second messenger. Intracellular calcium can also be released in response to thermal and kinetic stress among others, so possibly the addition of such a high concentration of suramin (1.5 mM) could have triggered a GPCR unrelated stress response. Yet another possibility is the presence of powder particles on solution, since suramin was prepared by dissolving its powder form on assay buffer.

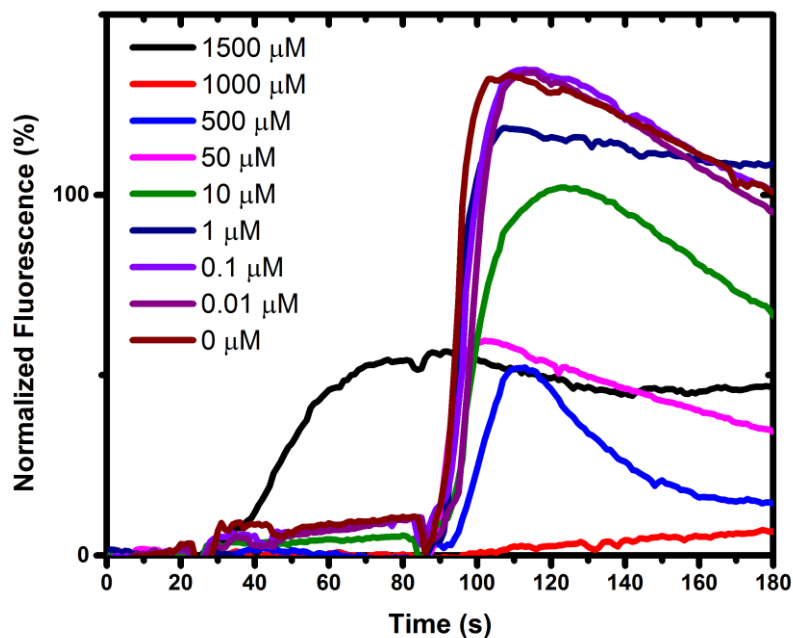


Figure 3-7 Normalized fluorescence vs time for different suramin concentrations in microtiter plates. Different concentrations of suramin were added at 20 s and 10 μM of UTP added at 80 s. The 1500 μM assay has an early response time because it was the cell response to suramin and not to UTP.

The cells usually responded only very weakly to suramin, with just a small increase in fluorescence at the 25-40 s mark, however, for the 1500 μM suramin concentration, the cell response to suramin was very high, as seen in Figure 3-7. As expected, the cell response to UTP increased with the lowering of the suramin concentration, with the response time start ranging from 85 to 90 s. This effect is due to the fact that suramin is a weak antagonist of P2Y2, so it binds to the receptor, but instead of activating it, blocks the agonist, UTP, from binding.

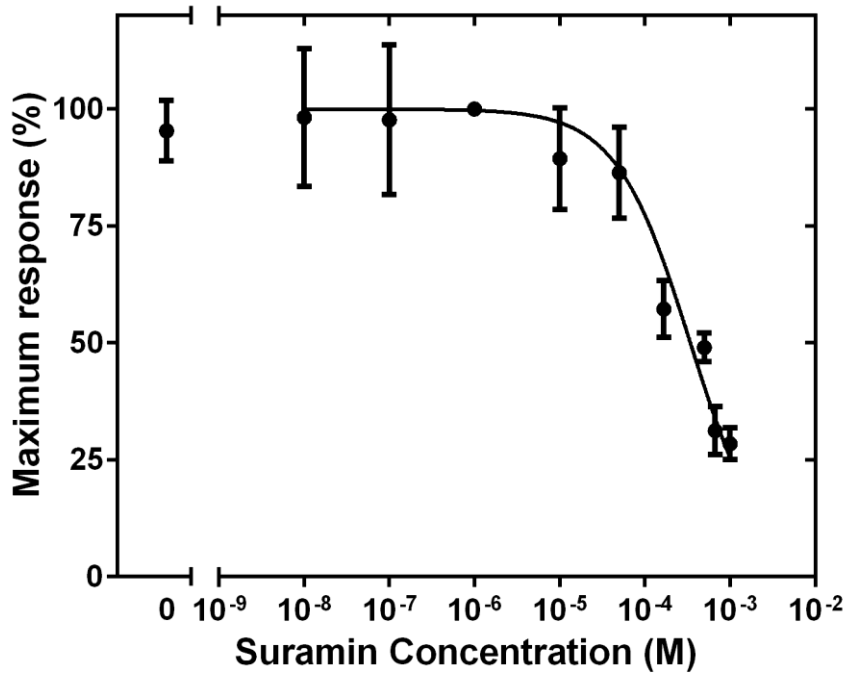


Figure 3-8 Antagonist Hill dose-response curve for suramin in microtiter plates. Each point in this graph corresponds to a single suramin concentration, and is an average of separate experiments. The error bars of each point represent the SEM. The obtained IC₅₀ value for suramin was 342 μ M. The method of analysis used was without background removal and the assay buffer was without calcium.

Because suramin is a weak P2Y₂ antagonist, the inhibition is not total, and there is still some response due to UTP on the highest suramin concentration, 1 mM. This suramin concentration was the highest possible to assay, since increasing its concentration from this point only lead to increased cell response from suramin alone.

The IC₅₀ (the antagonist concentration that inhibits 50% of the response) obtained for suramin was higher compared to that of literature, namely, 342 μ M as opposed to the reported 50 μ M. [35]

3.2. Microscale

The experiments performed at macroscale, agonist and antagonist assays, were also done at microscale. A microchannel with a chamber for cell adherence and a total volume of 255 nL was used. The channel had a height of 60 μm , a chamber with 1 mm of diameter and two arms coming from each side of the chamber with a width of 200 μm . The channel was first filled with fibronectin, an ECM protein, to facilitate the adherence of the cells to the channels surface. The cells were inserted into the channel and settled inside the chamber as pictured in Figure 3-9.

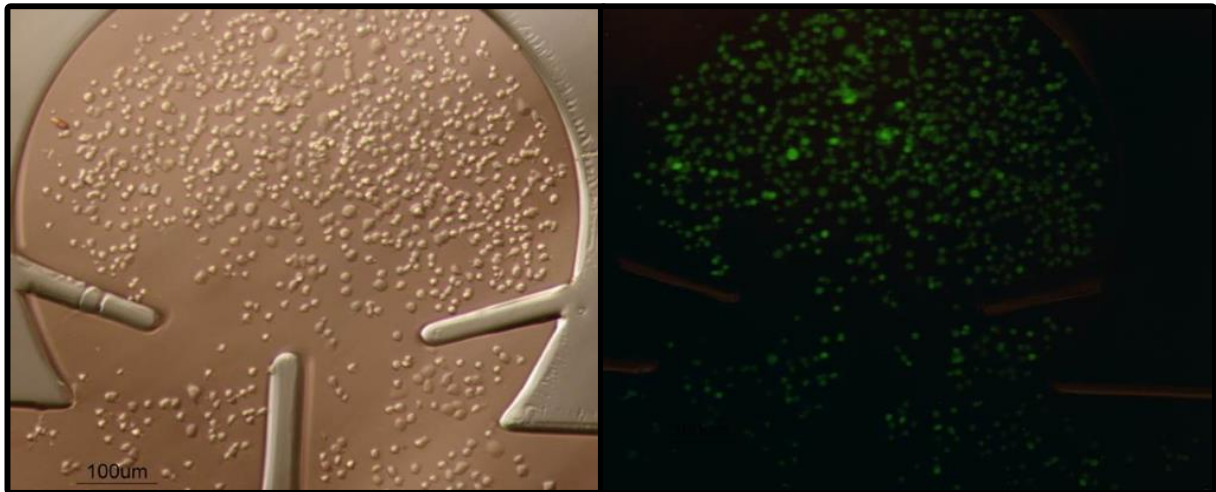


Figure 3-9 Microfluidic chamber with cells. The picture on the left shows the cells adhered to the channel coated with fibronectin. The picture on the right shows the same cells on the same channel but exhibiting fluorescence due to the fluorophore Fluo4.

3.2.1. Fluo4 Direct Optimization

The conditions of the macroscale assays were adapted to microscale, using practically the same solutions. However, because the cells get sensitive inside the channel, the concentration of Fluo4 Direct™ needed to be optimized for microfluidic experiments. Experiments were done with different proportions of Fluo4 and cell medium (DMEM with 10% FBS and 1% Anti-Anti), as pictured in Figure 3-10.

In Figure 3-10, there is an increase in fluorescence with the increase in Fluo4 proportions, however, for the highest concentration, the cells were at high stress and detached from the channel and were washed out. Fluo4 is a compound that enters the cells and binds to calcium, leading to fluorescence, but it is toxic to cells, so the highest the concentration, the least the cells will tolerate it and die or detach from the channel. Also, the time the cells are exposed to Fluo4 is important, as the longer they are exposed to it, the more fluorescent and stressed they become.

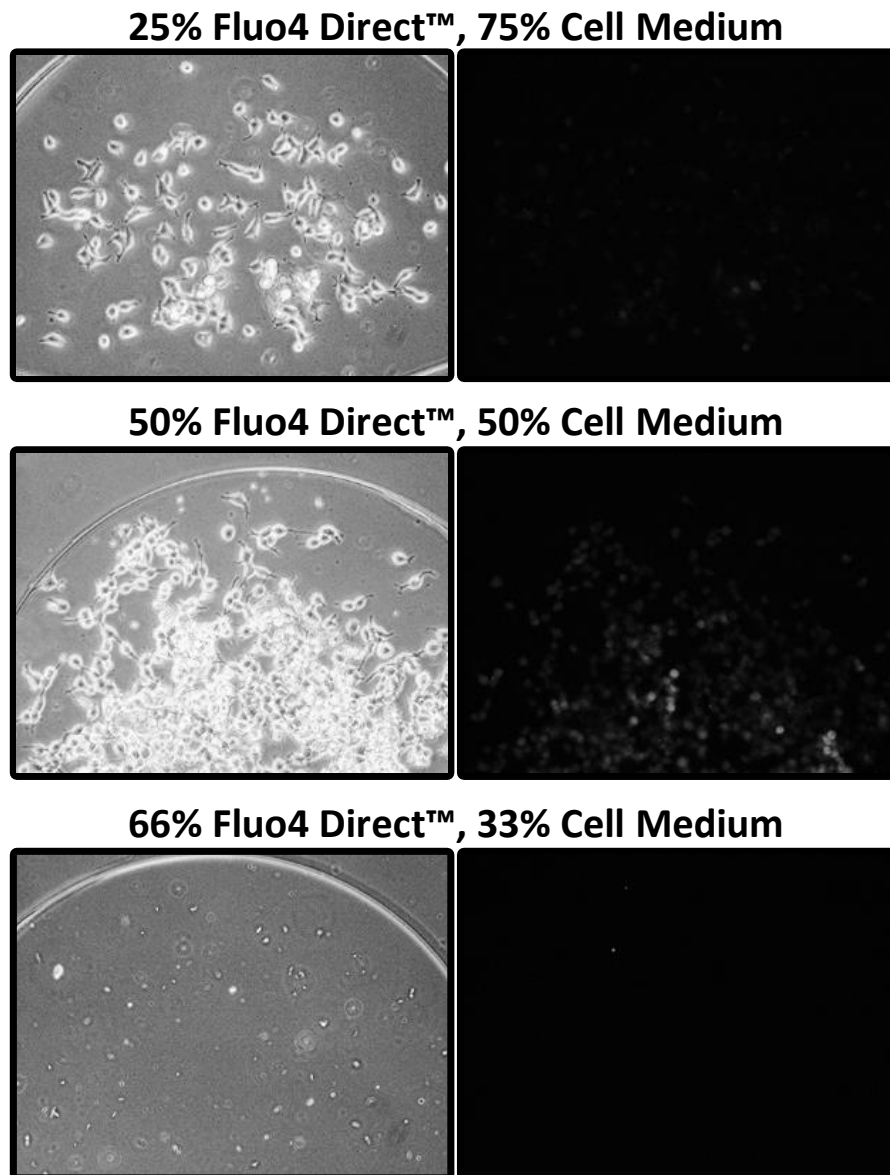


Figure 3-10 Microfluidic Fluo4 Direct™ concentration optimization experiments. On the left is the bright field image of the channel with cells and on the right are the fluorescent images in greyscale. Each channel was first incubated with fibronectin for 2 h, the cells were inserted and the different proportions of Fluo4 and cell medium flowed inside the channel.

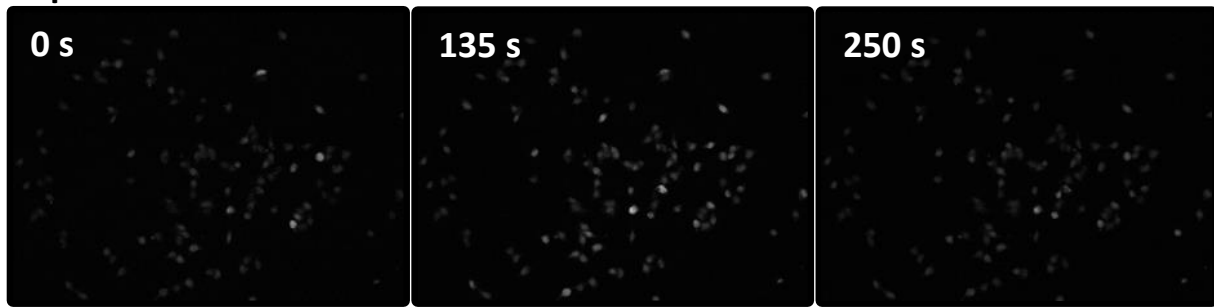
For the experiments where 25% or 50% of Fluo4 solution was used, the cells stayed in the channel and were fluorescent. For the 50% Fluo4 solution, the cells were very fluorescent and it would be difficult to do an assay and distinguish the basal calcium level from the response, as it was too fluorescent to begin with. Also, the cells were trying to find contact points, as evidenced by the dark filaments coming out of the cells, which is a sign of stress. When a 25% Fluo4 solution, was used the cells didn't appear to be as stressed as with the other concentrations and were not too fluorescent. So, for the remaining microfluidic assays, a Fluo4 Direct™ solution of 25% with cell medium was used.

3.2.2. Agonist Assays

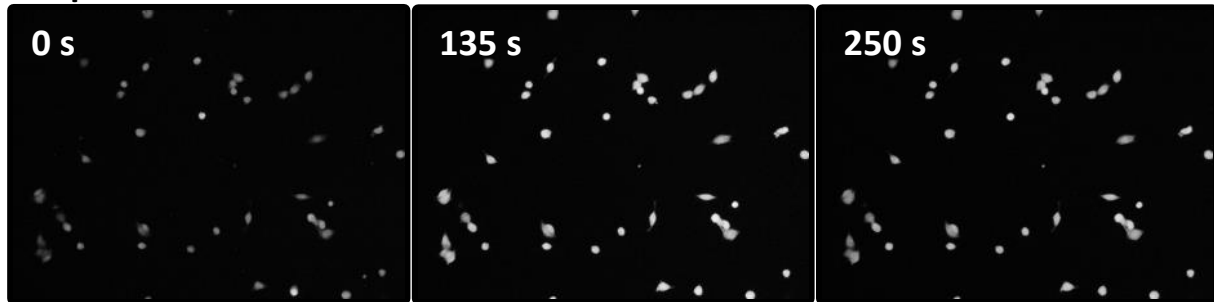
The range of UTP concentrations used for the microfluidic agonist cell assays was similar to the one used in the microtiter plate experiments, 100 μM -0 μM UTP as opposed to 150 μM -0 μM UTP. The reason for this change was the fact that for concentrations below 100 μM , the receptor appeared to be already saturated and hence, higher points were not required. The main difference in the microfluidic assay compared to the well plate was that for the former, the UTP would be flowing into the channel, whereas in the latter it was dispensed from a pipette over the cells. Initially it was thought that the EC50 for the macroscale experiment would be lower than the microscale, as the cells would get a violent burst of UTP after it was dispensed from the pipette with convection being the major mass transfer mode, as opposed to diffusion in the microfluidic channel. Diffusion was thought to be the main mode of mass transfer in the microfluidic channel because of the chamber section where the cells would adhere. In that section of the channel, there is a lower velocity as a result of an expansion in width from the section leading up to it, so convection shouldn't play a big part in mass transport. Another big difference between the two assaying platforms is the concentration of cells being assayed. In the microtiter plates, the microscope view area, 10x objective, would have a great number of cells, ranging from a few hundreds to almost a thousand of cells, enabling a good estimation of the mean calcium response of a cell population. In the case of the microfluidic channel, it was very difficult to have a constant number of cells inside the microchannel as it varied with the concentration of cells inserted, fibronectin or laminin functionality, and mainly because when the tubing was cut, after cell insertion, many cells would leave the channel. Also, when cell insertion worked well the maximum number of cells achieved almost never reached a hundred. This was a problem because it made having a good estimation of the cell population response difficult and also left a large area without cells. The latter problem was fixed by removing the background using ImageJ software.

In the microfluidic assays, because the drug was flowed, the way the cells responded to the drugs was slightly different, instead of having the cells respond all practically at the same time, the cells had different response times and also the fluorescence was of smaller duration, with some cells just blinking and then quickly returning to their basal fluorescence level. These differences might be due to the flowing nature of the assay, as the drug molecules are constantly being replenished inside the chamber with some of them washed from the receptors, possibly explaining the blinking effect. The fact that all the cells were not responding simultaneously, could be due to the microfluidic assay being done in a flowing mode with some cells exposed to flow at different times, this was also evident in the microtiter assays when the drug was dispensed from the pipette at the borders of the well plate, causing a sort of cascading fluorescence effect, as the cells closer to the point of dispensing responding first than the others. In Figure 3-11, the cell response to different concentrations of UTP in a microfluidic device is pictured.

0 μM UTP



50 μM UTP



100 μM UTP

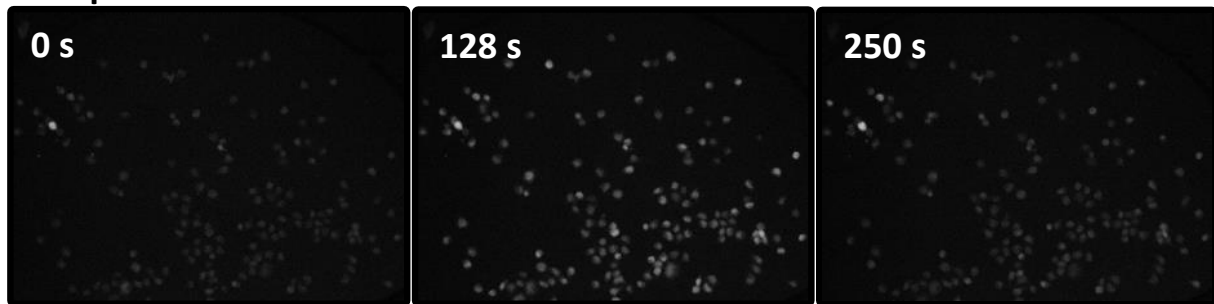


Figure 3-11 Cell response to different UTP concentrations at similar time points in the microfluidic chamber. The picture of the first time point for each concentration was taken at the beginning of the assay, the second picture was taken when the maximum fluorescence was reached for a particular assay and the final picture was taken at the end the assay. In these assays, the cell basal fluorescence was recorded for 10 s, and then the fluorescence shutter closed, as not to bleach the cells. Then at about 40 s the pump was turned on, with UTP flowing into the channel, and the fluorescence shutter opened 20 s later. The remaining assay time was for monitoring the cell response to UTP.

As can be seen in Figure 3-11, the cell concentrations inside the chamber varied significantly, something not ideal for consistent measurements, as a lower number of cells caused a larger background area and the cells to appear more fluorescent, since the Fluo4 solution is the same for all assays, with each cell absorbing more fluorophore. Also, due to the flow, the cells can respond to the buffer, as just the slight convection can lead to the release of calcium unrelated to GPCR signaling. This is especially significant when the cells are in a more stressed state, becoming very sensitive to flow. There are several reasons as why the cells become stressed, such as not having enough laminin or fibronectin inside the channel

for them to adhere, being subjected to high flow rates, being in contact with Fluo4 for too long and when a cell passage is done at high confluence (when the cells are too close to each other on the T-flask). The latter reason can be very significant, as subsequent cell passages, even if done at good cell confluence (about 80%), will have cells that prefer to be in clusters and become very stressed when put inside microfluidic channels, where they can't be as close to each other as they were in the T-flask. When the cells were stressed due to this reason, they would not respond to the drug, probably because they had released intracellular calcium due to other stimuli (sometimes the mere cutting or inserting the tubing leads to calcium release) or they would respond highly just to the flow, making it difficult to distinguish between the control assay with buffer and the highest concentrations of UTP, such as 100 μM . Even though there were some problems, there were some successful experiments, with some shown in Figure 3-12.

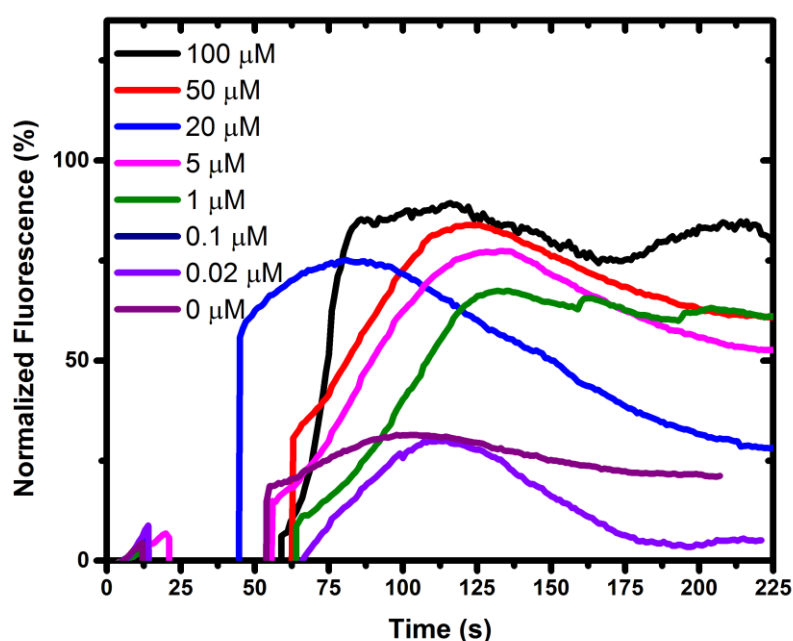


Figure 3-12 Normalized fluorescence vs time for different UTP concentrations in the microfluidic chamber. In each assay, the baseline was recorded for 10 s and then the fluorescence shutter closed, so as not to bleach the cells. The drug flow was activated at 30-40 s and the shutter opened at 45-60 s, with the remaining time used to monitor the cell response to UTP. The gap between the baseline monitoring and the cell response is due to the closing of the fluorescence shutter.

In Figure 3-12, the cell response time is not as consistent as the one observed for the microtiter plate assays, as it is difficult to know as when the flow will go inside the chamber, with being fast on some assays and being slow with others. In some cases, such as the 0.2 μM UTP concentration, is difficult to be sure that the observed cell response is due to the drug or just from the insertion of the capillary tubing or flow, since the response happens very fast (at around 50 s) as opposed to the other assays (70 and 125 s). In the beginning of every assay, the baseline seems to increase, and this happens because of

the light from the lamp. As the cells are in a microfluidic channel on top of a relatively thin glass substrate and slightly stressed, the light has an effect on their behavior, causing a slight increase in fluorescence, as opposed to the microtiter plates where the distance between the cells and the lights is greater. This reason is also why the shutter is closed, because if it were to stay open, the cells would be subjected to even more light, which would cause added stress and eventually bleaching. It is also easy to notice that the concentrations ranging from 100 μM to 1 μM have very similar maximum fluorescence values as opposed to the 150 to 20 μM range observed at macroscale (Figure 3-3). This shift of about an order of magnitude, from 20 to 1 μM at the top plateau, is also present in the EC50 obtained for the microfluidic assays.

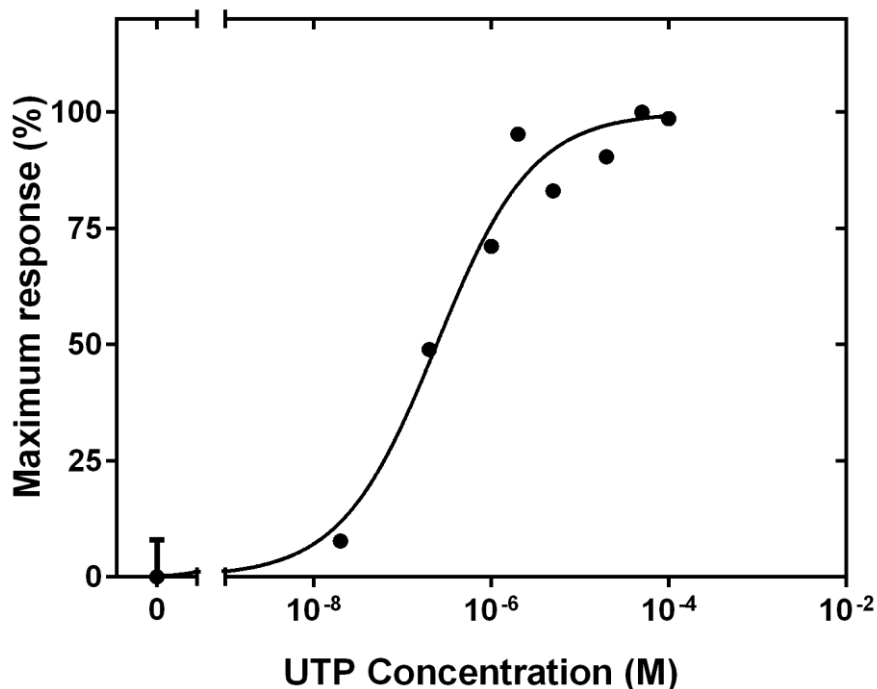


Figure 3-13 Hill dose-response curve for UTP in the microfluidic chamber. The video data used for this graph was analyzed using the removing background method. The EC50 value for the microfluidic GPCR assay with UTP was 0.24 μM .

The video analysis method where the background is removed was used for microfluidics, the reason for this choice was that for low cell concentrations, it would be difficult to detect the maximum fluorescence because of the noise from the background, which diluted the signal obtained from the cells. Without removing the background, high cell concentration assays were yielding consistently higher results than low cell concentration assays independent of UTP concentration, so an analysis method only focusing on the cells and neglecting the background offers a better estimation of the fluorescence of the cells. The comparison between the two methods can be seen in Video Analysis Methods in the Appendix section.

The EC₅₀ obtained for the microfluidic experiments was one order of magnitude smaller than the one obtained for macroscale, which was between 4.2 and 3.1 μM . The 95% confidence interval for the microfluidic UTP assay, in Figure 3-13, was from 0.1 to 0.56 μM , and so the difference between the two platforms is quite significant. The difference in EC₅₀ was to be expected, however, it would seem more likely to be the other way around, with microfluidics having a higher value than microtiter plates, for the reasons explained before. There is no conclusion to be made on which method has the best EC₅₀ value compared to the literature, because as shown earlier, there are values in the 1.5-5.8 μM range and there are values in the 0.14 μM range, with the latter being a value within the 95% confidence interval for the microfluidic assay.[34][15] These literature values have to be taken with a grain of salt, as neither reported value was obtained using this particular cell line, HEK293T, as well as some being done using recombinant cells with the P2Y₂ receptor overexpressed, so the comparisons can't be incredibly accurate.

It is important to note that the percentage of failed assays using microfluidics was quite high, as many problems can arise, and that for a significant portion of this work, the live cell calcium assays in microfluidics weren't working, as the cells were not responding. This lack of response could be because of the confluence hypothesis discussed above, as there was a passage that had high confluence and cells from subsequent passages weren't responding. One of the major problems was the presence of air bubbles that, when inside the chamber during the measurement of fluorescence, ruin the assay. Also there was always the chance that the cells wouldn't adhere to the channel, even with fibronectin or laminin, particularly when they were stressed. During cell insertion if the concentration of cells being used was high, there was a chance that the cells would clog the channel and when washing the channel, the chamber would become full with dead cells. The cells could also respond before the assay time, and when the drug was flowed inside the channel, they wouldn't respond.

However, despite the technical challenges, the proof-of-concept was established using the working experiments.

3.2.3. Antagonist Assays

Different concentrations of suramin, the antagonist, were first tested to determine which concentration caused the cells to respond. In the microtiter plate assay using suramin, it started to cause some cell response after 1000 μM , so a suramin assay was performed with the results in Figure 3-14.

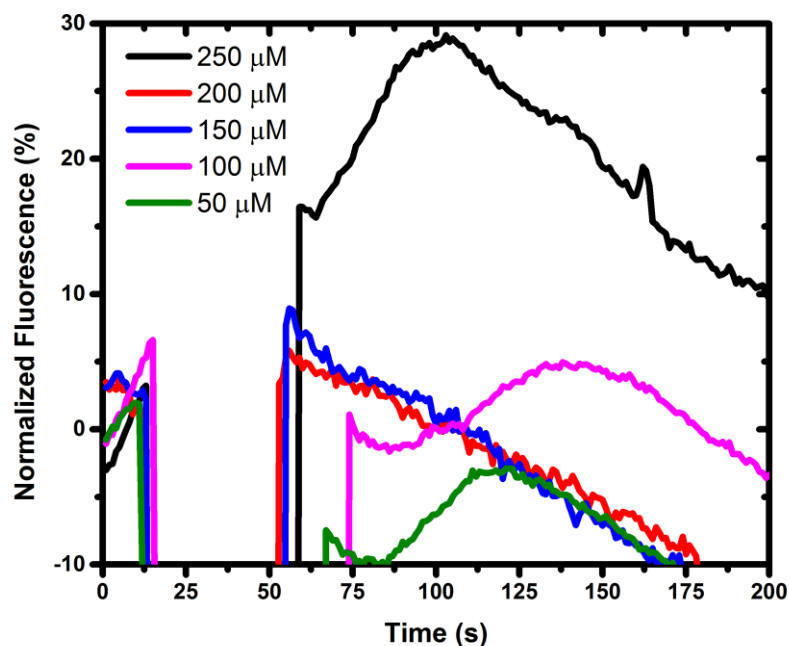


Figure 3-14 Normalized fluorescence vs time for different suramin concentrations in the microfluidic chamber. The assay was conducted in the same manner as the UTP assay.

In Figure 3-14, the only concentration of suramin that produced a significant cell response was 250 μM , while the other concentrations had a negligible effect. It is interesting to note that for the concentrations 50 and 100 μM , there was a decrease in fluorescence relative to the baseline, with suramin having a sort of inverse-agonist like behavior, which was unexpected. With this assay, it was possible to determine that for concentrations greater than 250 μM suramin would elicit a response from the cells. There was a decrease of almost one order of magnitude from the macroscale assays, with the concentration with significant response being 1500 μM suramin. This decrease in the concentration needed for cell response, an increase in sensitivity, is similar to the one found for the agonist assays, where the EC_{50} difference between macroscale and microscale was also close to one order of magnitude.

Antagonist assays were also done at microscale, however, these assays proved to be a bigger challenge than the assays using UTP. The reason for the difficulty was that an emulation of the way it was done in macroscale would be difficult to implement, as it used sequential injection, meaning that one solution, the antagonist, is first added, left to settle and then a second solution, the agonist added. In microscale,

doing a similar procedure would entail two capillary tube changes during cell assaying, which is prone to human error, as well as disturbing the cells, since the displaced fluid from the tubing could enter the channel at higher velocities and cause cell response due to flow. Also in biological terms, a flowing sequential assay could also be difficult to accomplish, as suramin can potentially be washed out from the receptor binding site, with molecules of UTP then binding and activating the receptor. This can be a problem, since when the agonist binds to the receptor, the latter is internalized, preventing further binding for a certain period of time, however, the same doesn't happen when the antagonist binds, there is no internalization [15], so, in a flowing mode the antagonist becomes vulnerable to washing out, with the receptor being available to the binding of an agonist molecule and activation. Because of the difficult reproducibility of even an agonist assay, and since sequential injection would greatly increase this problem, it was abandoned. The methodology adopted for the microfluidic antagonist assays was to mix different concentrations of agonist with the same antagonist concentration. With this approach, named mixed antagonist, instead of obtaining an IC₅₀ value, what would be obtained would be an EC₅₀ with an expected shift to the right, meaning that a higher concentration of UTP would be needed to reach the 50% of maximum response as suramin should block the receptor.

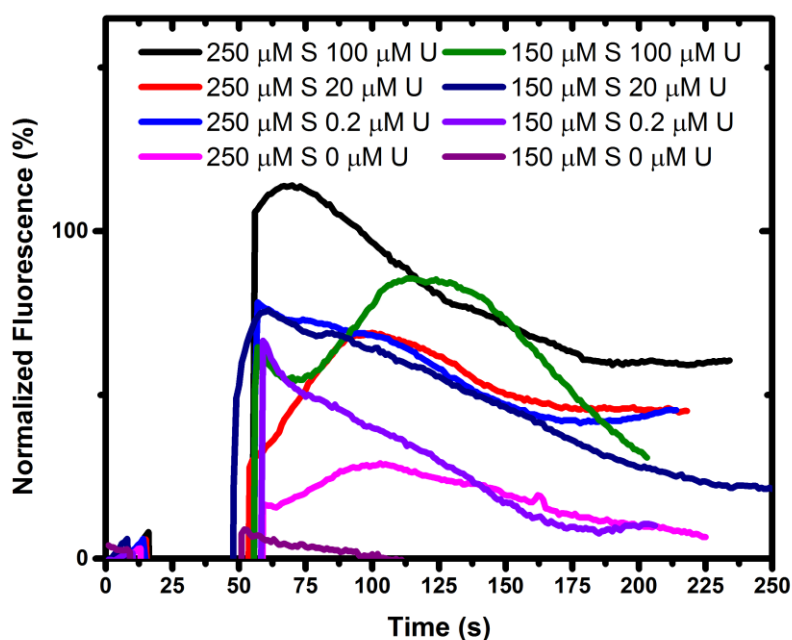


Figure 3-15 Normalized fluorescence vs time for different mixed antagonist assays in the microfluidic chamber channel. These assays were done in the same manner as the UTP and suramin testing assays. On the figure legend, S stands for suramin and U for UTP.

By maintaining a constant concentration of antagonist and varying the concentration of agonist, an EC50 value could be obtained for that particular suramin concentration and compared to the one obtained when only the agonist was used. With this method, it is possible to determine the inhibition of the receptor through direct competition between the agonist and antagonist.

The results shown in Figure 3-15 represent two concentrations of suramin mixed with different concentrations of UTP. It would be expected that the fluorescence intensity of the results with 150 μM would be higher than the ones for 250 μM , because the higher the concentration of antagonist the greater the inhibition, and so less fluorescence. For the UTP concentrations of 20 and 0.2 μM , in 150 μM suramin, the fluorescence intensity obtained for both was very similar, and different from the one obtained when no UTP was in solution, which also was an unexpected result. The expected result would be a lower plateau of concentrations with similar response and an upper plateau with the same happening. The maximum of each of the assays in Figure 3-15 was extracted and a dose-response curve plotted.

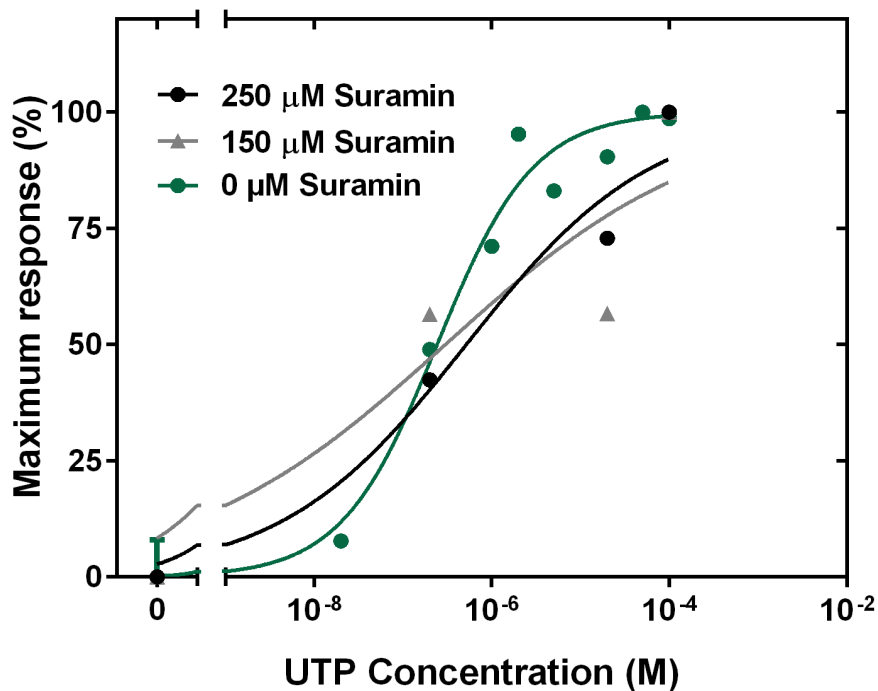


Figure 3-16 Hill dose-response curves for the mixed antagonist assays in the microfluidic chamber. The video analysis method used was the one where the background was removed. The best-fit values for the EC50, for the assays where a concentration of 250 μM and 150 μM suramin was used, were 0.52 and 0.3 μM , respectively. The dose response for the agonist assay was also plotted for comparison, its EC50 is 0.24 μM .

The dose-response curves obtained for the mixed antagonist assays with 250 μM and 150 μM were not good, because, there were not enough data points to enable a good fit, so the curves in Figure 3-16 are a very crude estimation of what a proper curve would look like. The best-fit values for the EC50 for the

two concentrations of suramin tested were 0.3 μM for 150 μM suramin, with a 95% confidence interval of 2.6×10^{-5} μM to 3414 μM and 0.51 μM for 250 μM suramin, with a 95% confidence interval of 0.01 μM to 18.5 μM . With 95% confidence intervals of this range, the results were not matching the envisaged trend, however, the best-fit values obtained, even if not accurate, were what would be expected. There was a shift in the EC50 to higher concentrations of UTP, when higher concentrations of suramin were used. For the agonist experiments where only UTP was used, the EC50 obtained was 0.24 μM , when 150 μM of suramin were present in solution the EC50 value rose to 0.3 μM and in the case of 250 μM of suramin the EC50 value was 0.52 μM . This was to be expected because if antagonist and agonist are both present in solution together, there should be some competition to bind to the receptor, and the higher the concentration of the antagonist, the more molecules there would be compared to the agonist, with a greater chance of the antagonist binding to the receptor and preventing the release of intracellular calcium due to GPCR activation.

3.2.4. Single Cell Traps

Single cell trapping experiments were carried out in the gradient generator channel. The goal of these experiments was to achieve single cell trapping, in order to assay each cell in a specific place, so single cell analysis could be performed. In the first experiment with the gradient generator channel, fibronectin was used to promote cell adherence to the channel after the cells were trapped. A picture of the cells in the trapping area of the channel is represented in Figure 3-17.

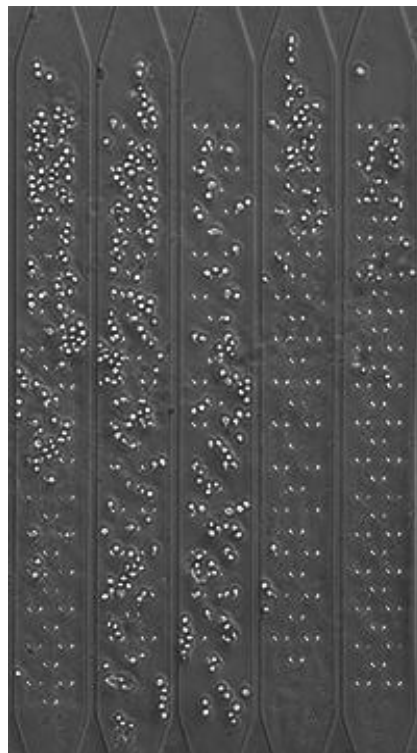


Figure 3-17 Cells trapped inside the gradient generator channel using fibronectin. In the two rightmost channels, the cell concentration is lower than on the remaining channels because there was a cell blockage upstream.

In Figure 3-17, it is possible to observe that the cells become stuck in the traps, although with the majority not in single cell traps. In this experiment with fibronectin, incubated for 2h, the concentration of cells used might have been too high, and after some time the cells started to cluster together in the trapping area. The fibronectin contributed to this clustering, making the channel sticky and causing the cells to remain in the channel in areas that had no traps, causing blockages. Although there was some clustering, there were some traps with single cells, and the vertical cell distribution inside the traps was rather homogenous and not concentrated just at the top.

In order to try to avoid the clustering of the cells inside the channel, an assay without fibronectin was performed. The difference between this experiment and the one done with fibronectin was that instead of incubating the channel for 2 hours with fibronectin, it was incubated with cell medium (DMEM with 10% FBS and 1% AntiAnti). This step was made so that some of the proteins in the medium would stick to the channel and allow for a better cell adhesion than just raw glass.

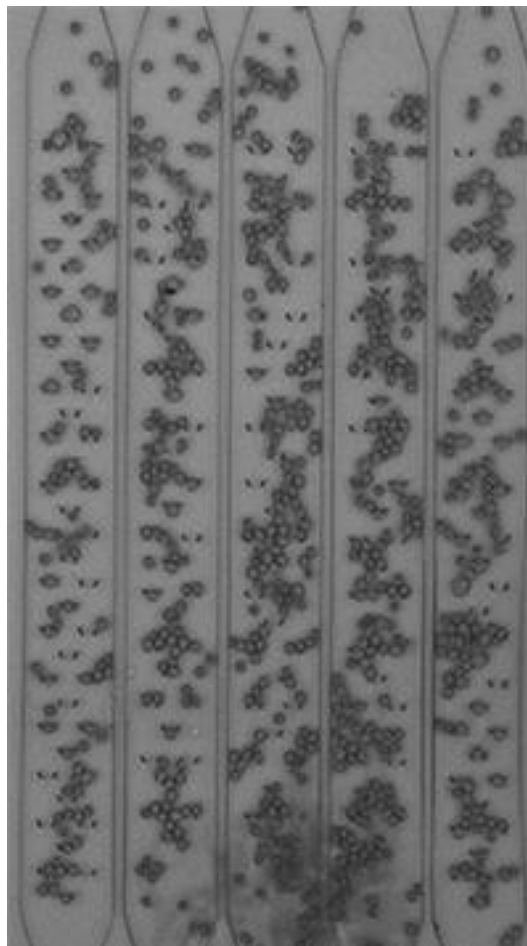


Figure 3-18 Cells trapped inside the gradient generator channel without using fibronectin.

Although there was some clustering in Figure 3-18, there are more single cell traps than in the experiment with fibronectin. The cell distribution in the channels is homogeneous, with similar concentration on the top, middle and bottom. Also, all the channels have similar homogeneity with the

three channels in the middle having a slightly higher concentration of cells. There is a significant number of single cell traps, especially on the leftmost channel in Figure 3-19.

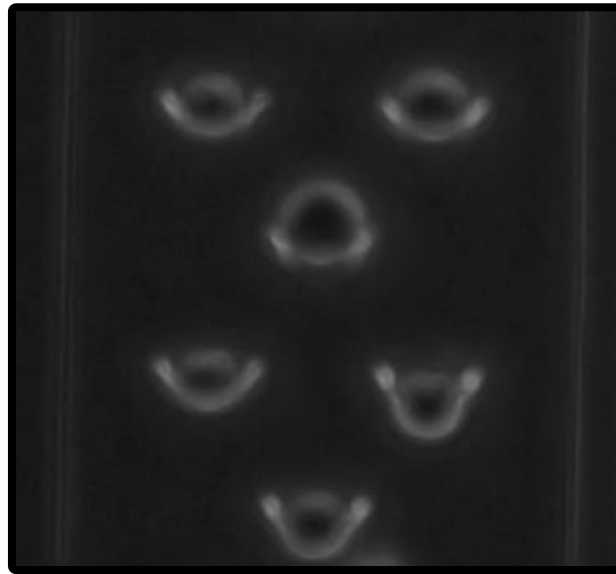


Figure 3-19 Single cell traps inside the gradient generator channel.

However, it is important to note that many cells passed through the middle of the traps, a gap of $7\ \mu\text{M}$, especially if the velocity inside the channels was high. The cells have a flexible membrane, so they squeeze through the traps despite their diameter being on average $10\ \mu\text{M}$.

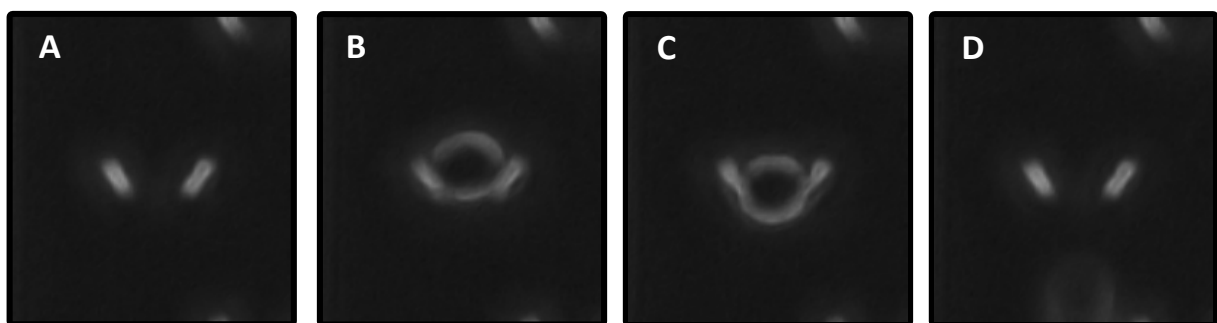


Figure 3-20 Cell leaving the trap through its opening, after being trapped. (A) The trap is empty. (B) The cell settles on the trap. (C) The cell membrane starts to contract and the cell starts to squeeze through the opening of the trap. (D) The cell escapes the trap.

Although, the example shown in Figure 3-20 represents a cell escaping the trap after it had been trapped, there were many cells that just passed through the opening of the traps without even settling there, meaning that the trap opening was too wide. The problem with the opening being too small is that the flow could have a different path, with the cells avoiding the traps altogether or that every cell would become trapped and the channel would quickly become clogged.

An interesting phenomenon observed in the single cell traps, was that cells that were too big and could not pass through the opening of the trap, would be still forced to go through the opening, due to flow, leading to bleb formation. Blebs are bulges of the plasma membrane, caused by localized decoupling of the cytoskeleton from the plasma membrane. They usually form due to increased intracellular pressure, generated by the contractile of a specialized layer of cytoplasm on the inner face of the plasma membrane which functions as a mechanical support of the plasma membrane, called cell cortex.[36]

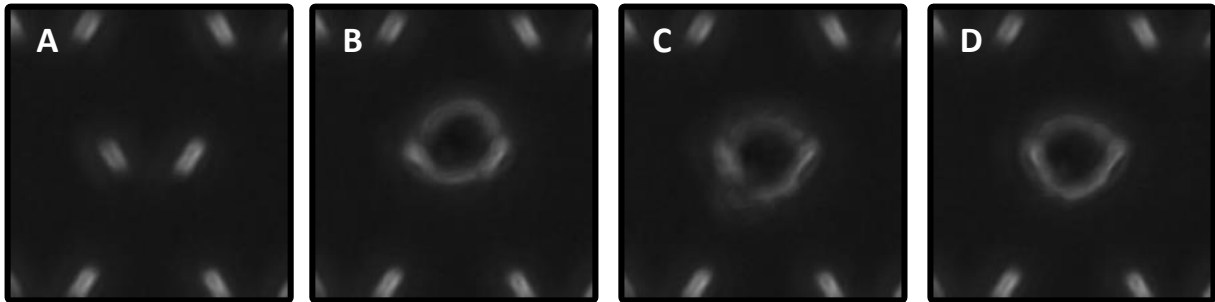


Figure 3-21 Formation of blebs on a cell in a trap.(A) The trap is empty. (B) The cell lands on the trap. (C) The cell tries to squeeze through the trap and, due to the increase of intracellular pressure, some protuberances start to appear from the cellular membrane, called blebs. (D) The blebs start to disappear and the cell stays trapped.

The formation of these blebs was also observed when performing cell insertion on the microfluidic chamber channel, especially if the flow rate was high. The blebs formed on the cells that were on the chamber channel didn't disappear unlike the ones observe in Figure 3-21.

Despite some clogging problems, the traps seemed to work properly, so the experiment was a moderate success, however there is room for improvement in the trapping process. The traps should have a smaller gap, maybe 4-5 μm , as the majority of the cells, more than 90%, didn't become trapped, also the channel should have an increased height, currently has 16-17 μm , so that the velocity inside the channel diminishes, lowering cell shear, and cells can pass above adhered cells, avoiding clogging. As the average cell size is 10 μm a height of at least 20 μm is recommended. Also initial cell concentration, insertion flow rates and times need to be optimized. The cell concentration used for the fibronectin experiment was too high, 0.3×10^6 cells/mL, causing clogging upstream, and the concentration for the experiment without fibronectin was 0.15×10^6 cell/mL, not causing clogging but filling the trapping area with too many cells. The insertion flow rate also needs to be optimized, with the flow rate of 500 nL/min being too high and the 100 nL/min being better, however the duration of insertion also plays an important role, as after about 8 min the cells start to form clusters, causing clogging.

3.2.5. Gradient Generation with Calcium Solutions

Gradient generation was tested using calibrated calcium solutions in the gradient generator channel. For this experiment, different concentrations of CaEGTA were mixed with K_2EGTA . The gradient

generator main principle was the mixing of different concentrations in laminar flow through diffusion. There were three inlets, with each having a different concentration flowed, and, through the contact with flows from the other inlets, a gradient was formed. The testing was done flowing 10 mM CaEGTA, 5 mM CaEGTA with 5 mM K₂EGTA and 10mM K₂EGTA with 0 mM CaEGTA, these concentrations correspond to 39 μM, 0.15 μM and 0 μM of calcium ions, respectively. The concentration of calcium ions is not proportional to CaEGTA due to the ionic strength and dissociation of EGTA, with the concentrations being calculated using the method explained in Appendix a.

The calculation of the output concentrations of the gradient generator were done using the information in [23]. In this paper, it was assumed that each level, starting from the top, was defined by the letter B, with the initial level, with three inlets being B=3, the next level, with 4 channel splits, being B=4, and the final level being B=5. Each vertical channel, or channel splitting, was defined by the letter V, with V=0 being the first branch of each level. A visual representation is presented in Figure 3-22.

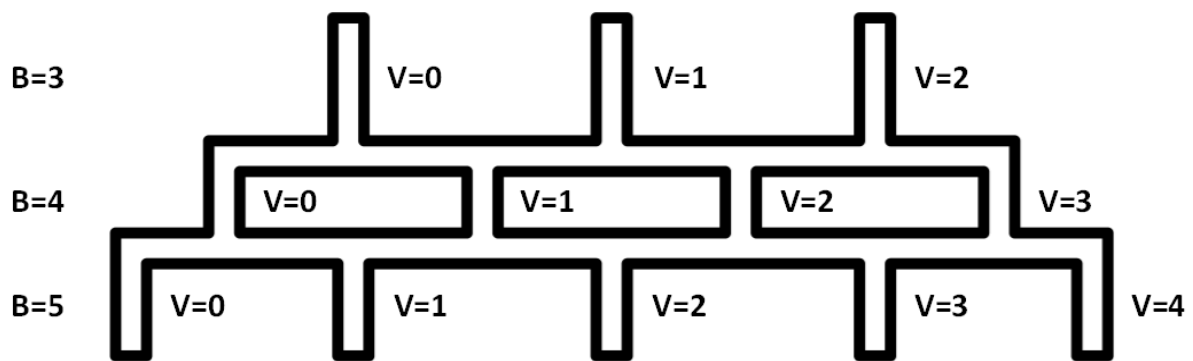


Figure 3-22 Representation of the gradient generator bifurcations and assigned letters.

In order to determine which fraction of flow from a level goes right or left in the level below Equation 7 and Equation 8 are used.

$$F_{left} = \frac{B - V}{B + 1} \quad \text{Equation 7}$$

$$F_{right} = \frac{V + 1}{B + 1} \quad \text{Equation 8}$$

In the equations above F_{left} and F_{right} are the fractions of flow going to the left and right, respectively. Using these equations it is possible to relate the fractions of laminar flow going left or right, which also enables the determination of the concentration that the joined flows will have, using Equation 9.

$$C = \frac{C_{right} \times F_{left}}{(F_{left} + F_{right})} + \frac{C_{left} \times F_{right}}{(F_{left} + F_{right})} \quad \text{Equation 9}$$

In Equation 9, C is the concentration in an intersection, C_{right} is the concentration of the flow coming from the right of the level above and C_{left} is the concentration of the flow coming from the left of the level above. A visual representation of these variables can be seen in Figure 3-23.

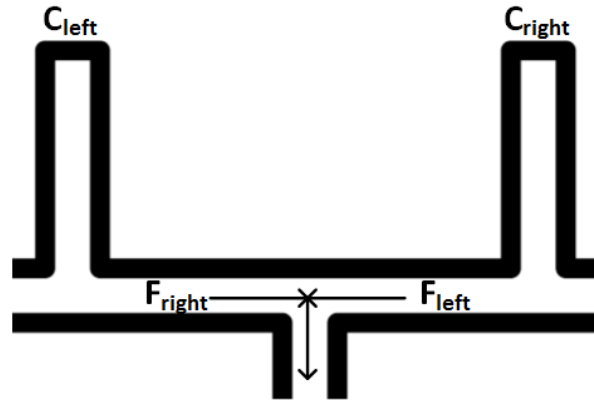


Figure 3-23 Mixing of two different bifurcations at an intersection.

The concentrations used in the gradient generator inlets were 10, 5 and 0 mM of CaEGTA with 4 μ M Fluo4, so using the equations shown below for all of the bifurcations it is possible to calculate the concentration at the desired place. The desired level would be the one where there were 5 separate channels, connected to the trapping area of the gradient generator channel. The concentrations in each of the different bifurcations of the channel are represented in Figure 3-24.

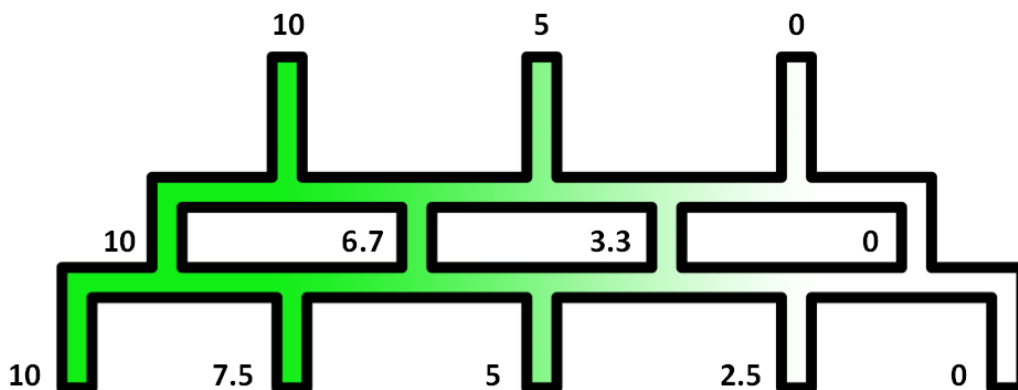


Figure 3-24 CaEGTA concentration in each of the different areas of the channel. The concentrations are expressed in mM. The concentrations can be inverted depending on the concentration at the inlets.

In the experiment performed, the inlet concentrations were, from left to right, 0, 5 and 10 mM of CaEGTA, and at the measurement site were, from the left to the right, 0, 2.5, 5, 7.5 and 10 mM of CaEGTA or 0, 0.05, 0.15, 0.45 and 39 μ M of free calcium. The measurements were done at 15 min intervals for 60 min, using an Olympus microscope, with CellSens imaging software using 1 s exposure time and 12 gain. The flow rate used was 0.5 μ L/min, to ensure that the liquid inside the 50 μ M sections, in the mixing area, was 10 mm/s as suggested by [23]. The results of the experiment can be seen in Figure 3-25.

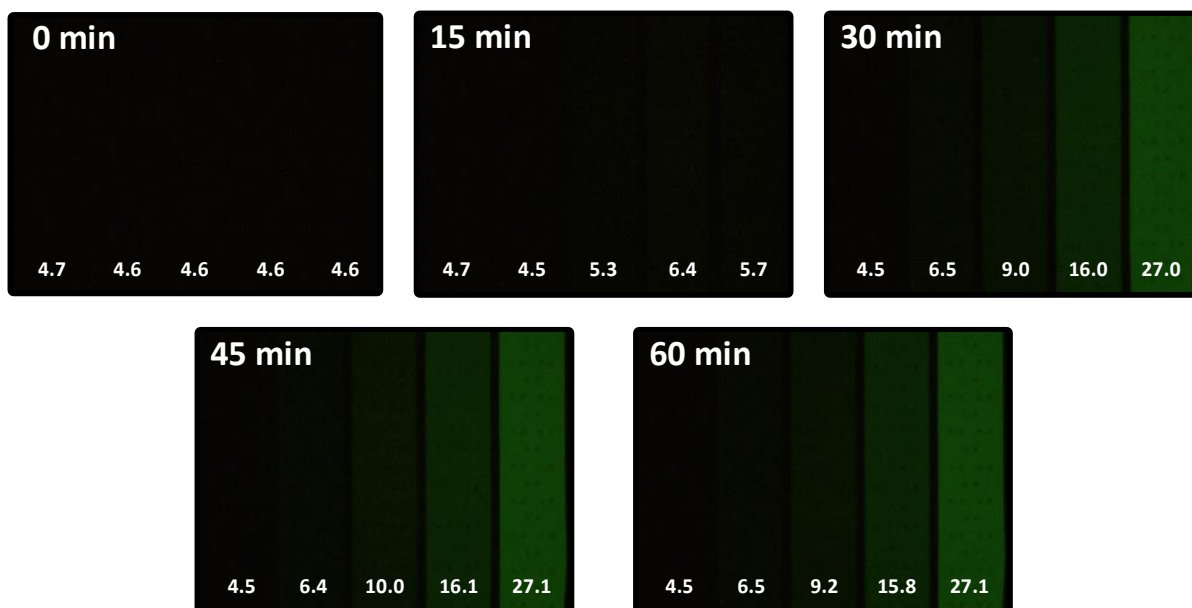


Figure 3-25 Gradient Generation using CaEGTA solutions with Fluo4. On the bottom of each channel, on each time point is the fluorescence value of that channel, in arbitrary fluorescence units.

The gradient generation worked well, with a distinct fluorescence difference between every channel after 30 minutes and then stabilization of the gradient without significant differences in the fluorescence of the channels. Also the left channel of the 30, 45 and 60 min time points showed no fluorescence at all, as its fluorescence value decreased compared to time point 0 min. There was a problem in the injection at the beginning of the experiment, with one of the concentrations 10 mM not entering the channel properly, which if had been done at the beginning would have stabilized the gradient at the time point of 15 min.

To determine the exact time of gradient formation, another experiment was done, this time capturing a video instead of taking single photos after a certain time. For this, the same microscope and software were used, but an exposure time of 5 s used instead. The results of this experiment are represented in Figure 3-26.

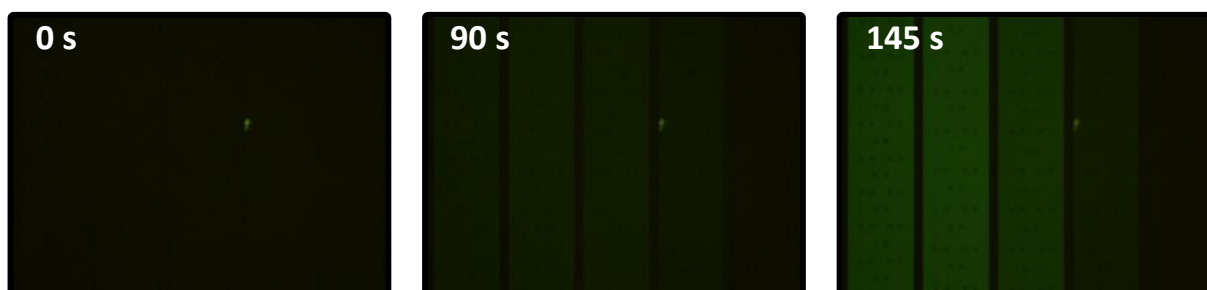


Figure 3-26 Determination of the time for gradient generation. In this experiment the initial concentrations were the same as the previous one, but the inlets are inverted, so 10 mM of CaEGTA is on the left and 0 mM of CaEGTA on the right.

The time it took for the gradient to be completely established was about 145 s, with the first fluorescent solution arriving at the measurement area at about 90 s. It is important to note that in the experiment represented in Figure 3-26, there was a piece of PDMS partially blocking the leftmost channel, causing the gradient not to be as defined as the one in Figure 3-25.

Overall, the gradient generation experiments were a success, as a defined gradient was achieved and in a time that is compatible with live cell experiments, 145 s. It can also be noted that a live cell calcium assay experiment with gradient generation of UTP was tried, however, there were some air bubbles inside the channel causing all the cells to be displaced and the assay to be ruined. In that experiment, the cells were already fluorescent inside the channel and three different concentrations of UTP, 100, 50 and 0 μM , were to be flowed. The gradient channel with fluorescent cells before air bubbles entered the channel is represented in Figure 3-27.

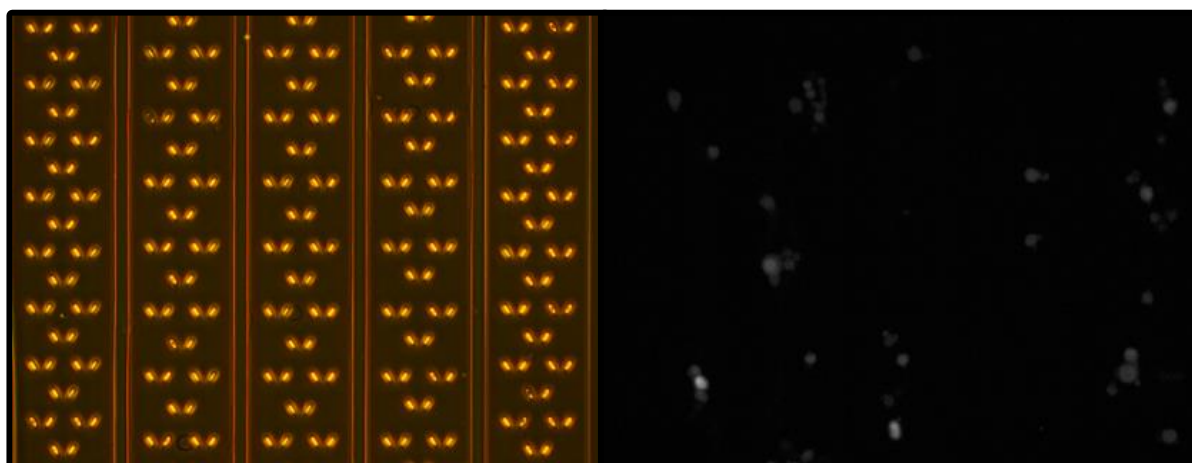


Figure 3-27 Fluorescent cells inside the gradient generator channel. The picture on the left is represented to give an idea about the location of the channels for the picture on the right.

3.3. Photodiode experiments

3.3.1. Photodiode Characterization

The photodiodes were characterized using two different light sources: a tungsten halogen lamp coupled to a monochromator and a light emitting diode (LED) with a peak emission wavelength at 470 nm coupled to a low pass filter with a cut-off at 500 nm. The LED was used since it was thought that it would increase photon flux and have a lower current, therefore removing some of the noise from the excitation light, while the increased photon flux would excite the cells or calcium solutions more and generate higher fluorescence. The wavelengths used for the lamp-monochromator combo were 494 and 516nm, these represent the excitation and emission wavelengths of Fluo4, the fluorophore used for the live cell assays and calcium experiments.

To determine the voltage at which the photodiode experiments should be done, a current density versus voltage was done. The operating voltage should be the voltage at which the difference between the current from the light sources and the dark current is greater, so maximum sensitivity can be reached.

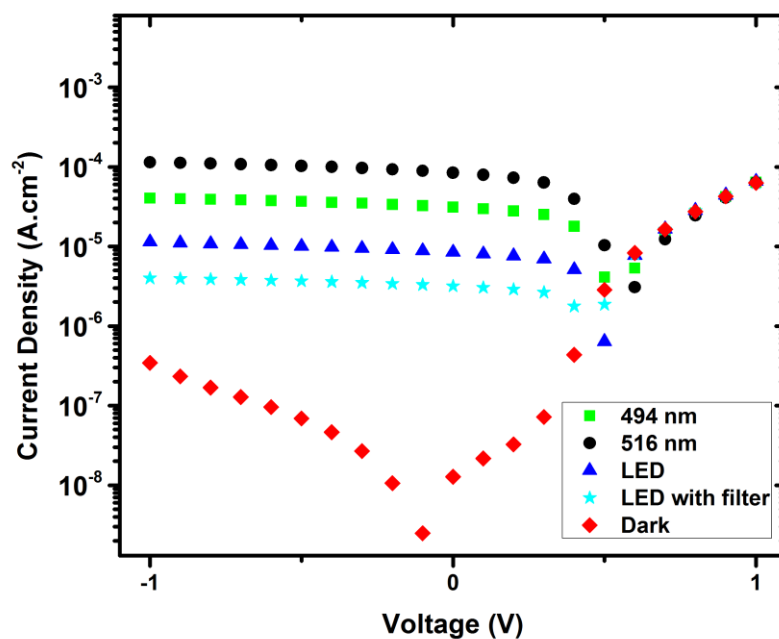


Figure 3-28 Current density vs voltage plot for the different light sources and the dark.

In Figure 3-28, all the different light sources and dark current have the same tendency with the increase in voltage, their current density decreases steadily, then drops abruptly and finally increase again. The dark current has a minimum peak at about 0 V, which makes the greatest difference between its current density and the current density obtained for all the light sources used, so this will be the voltage used.

The efficiency of the integrated filter of the photodiode was also characterized, and for this experiment, wavelengths ranging from 400 to 600 nm in intervals of 5 nm were tested, the current density analyzed and converted to external quantum efficiency.

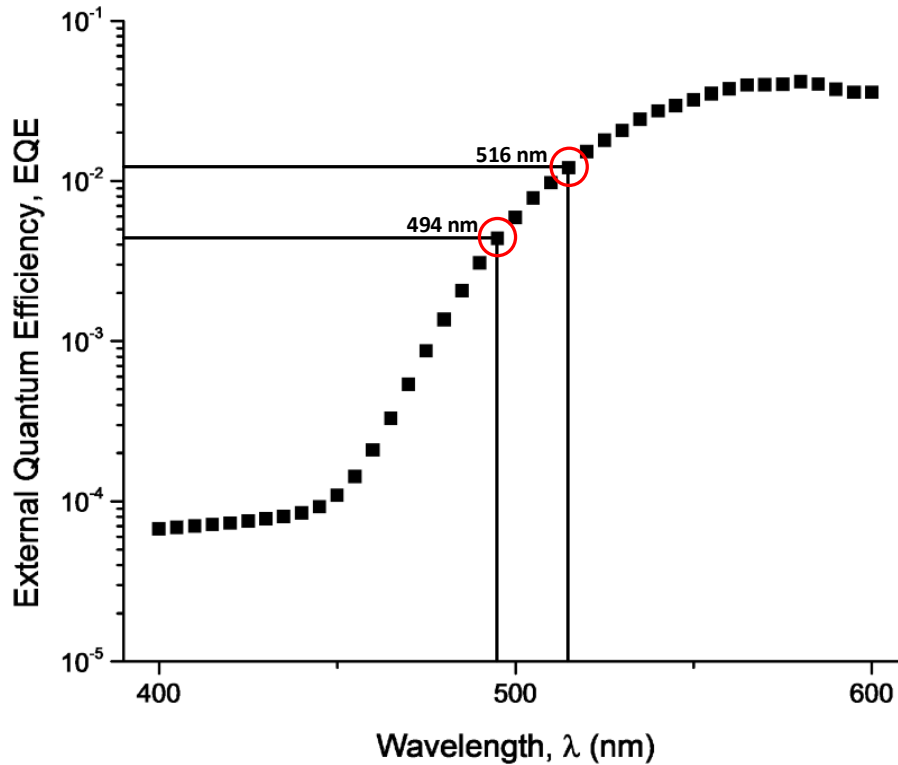


Figure 3-29 External quantum efficiency of the photodiode for wavelengths ranging from 400 to 600 nm.

The photodiode integrated filter blocks low wavelength light, wavelengths under 450 nm have a very low current, and because it is an absorption filter, there is a steady increase of current with higher wavelengths until a plateau at about 550 nm is reached, where the current is maximal. In Figure 3-29, the most important thing to consider is the ratio between 494 and 516 nm, as these are the wavelengths that need to be distinguishable. The EQE for 494 nm is 0.0044 and for 516 nm is 0.012, which corresponds to a small EQE ratio of 2.8. Due to the small Stokes shift of Fluo4 and the characteristics of the integrated filter, the EQE difference between the emission (516 nm) and absorption (494 nm) is not very big, meaning that it would be difficult to differentiate between the excitation light and the fluorescence emitted from the cells. The filter integrated in the photodiodes is not optimal for this type of cell assays, as the EQE ratio between excitation and emission is very low, it is only 2.8, while in other studies ratios of about 20 have been reported for amorphous silicon photodiodes.[3]

The photon flux for the different wavelengths of light from the monochromator and the LED was measured using a calibrated crystalline silicon photodiode (Hamamatsu S1226-5BQ). The photon fluxes measured with this device are represented in Table 3.2.

Table 3.2 Photo fluxes for the light sources used. *The shown wavelength for the LED is its peak emission wavelength.

Light Source	λ , Wavelength (nm)	Φ , Photo Flux (cm^2s^{-1})
LED	470*	3.85×10^{15}
LED with filter	470*	2.80×10^{15}
Lamp and monochromator	494	2.51×10^{15}
Lamp and monochromator	516	2.81×10^{15}

The current density obtained from the photodiodes using these sources with different external neutral density filters was also measured, and is represented in Figure 3-30.

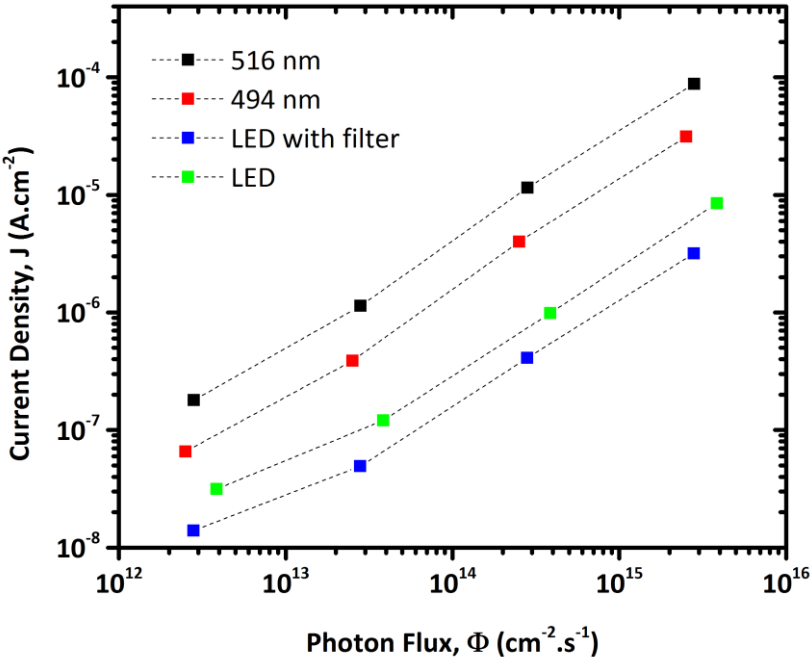


Figure 3-30 Relationship between the current densities (J) and the incident photon flux (Φ) for different light sources. The different photon fluxes for each light source were obtained using neutral density filters.

It is important to note that all of the points in Figure 3-30 have a higher current density than the dark current density at the operating voltage (2.5 nA), with the lowest current density obtained for the LED with filter being 14 nA. This current density was obtained using a neutral density filter that cut light

intensity 1000 times. The fact that all light sources have higher current densities values than the dark is good, meaning that experiments can have some sensitivity, however the lowest value for the LED with filter is close to the dark current, with results in that range having some noise, as seen by the displayed non-linearity of the lowest current densities obtained. The higher the current densities, the more linear the relationship between the photon flux and current density, as evidenced by the 494 and 516 nm plots.

3.3.2. Calcium Fluorescence Experiments

The measurement of different fluorescence calcium concentrations, using the 200 × 200 sq.microns amorphous silicon photodiodes were done in the microfluidic chamber channel using a LED coupled to a low pass filter and tungsten-halogen lamp coupled with a monochromator at a wavelength of 494 nm

The calcium solutions used for this experiment were the same as the ones used for the gradient generation experiment. Solutions of CaEGTA and K2EGTA were mixed to achieve different concentrations of free calcium, with Fluo4 pentapotassium salt being added to make the solutions fluorescent. Prior to the photodiode experiment, the solutions inside the channel were analyzed using an Olympus microscope (Figure 3-31), with CellSens software at an exposure time of 1 s and 12 gain. The final concentration of the solutions used was 0, 2, 4 and 10 mM CaEGTA, which equates to 0, 0.038, 0.1 and 39 μ M of free calcium, respectively.

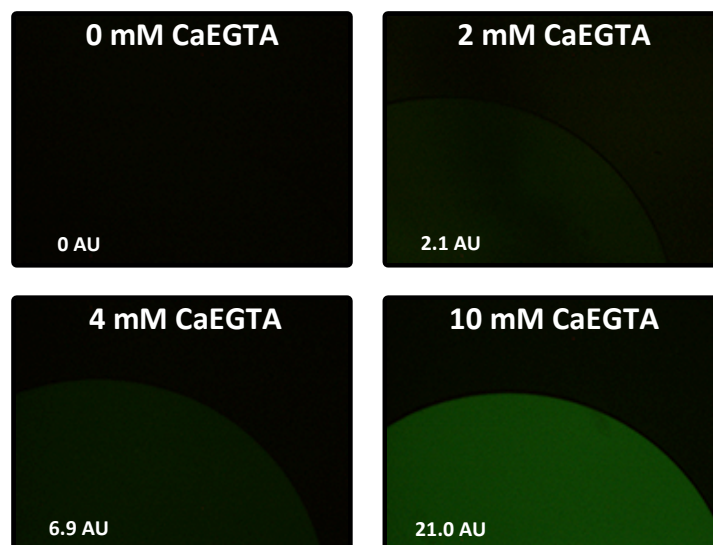


Figure 3-31 Fluorescent calcium solutions inside the microfluidic chamber channel. The number on the bottom of each picture represent the absolute fluorescence (channel fluorescence minus background fluorescence) value of that channel, in arbitrary fluorescence units.

The same channels were then measured on top of the photodiodes, with the results obtained in Figure 3-32.

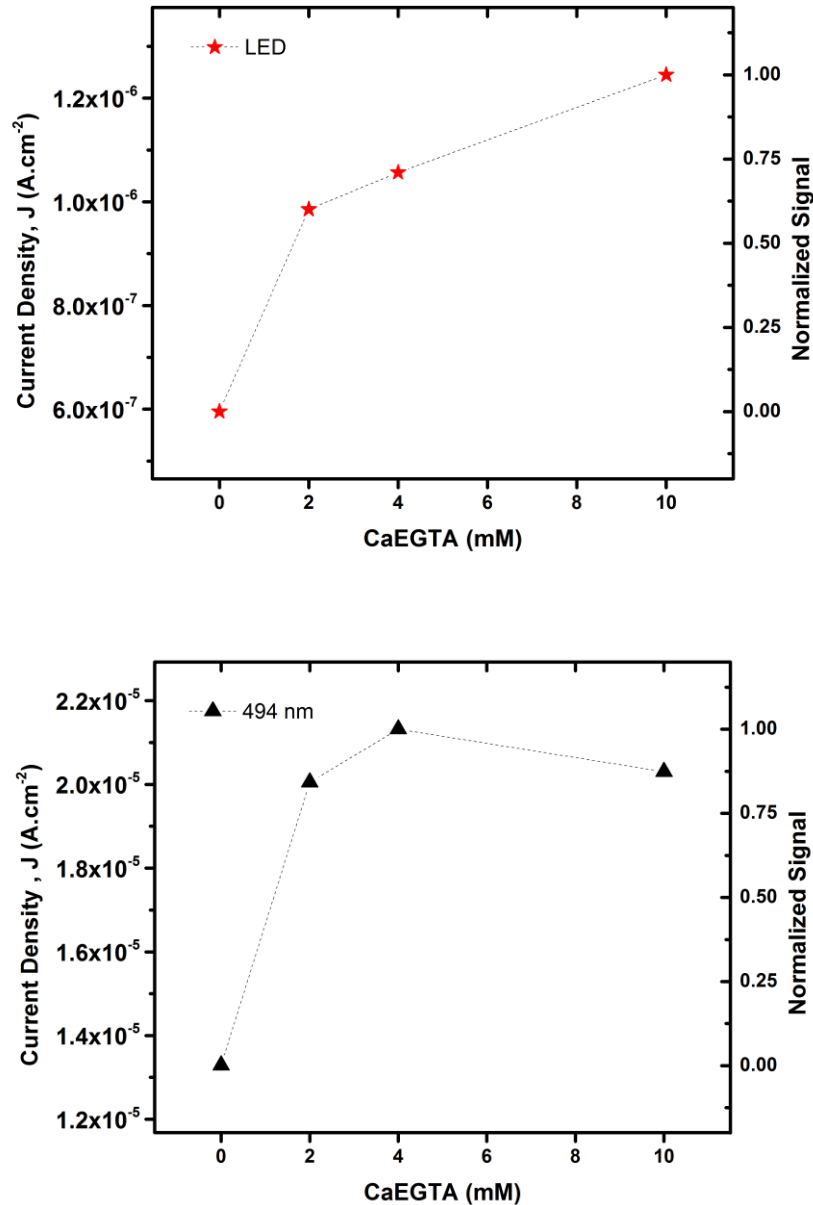


Figure 3-32 Calcium fluorescence measurement using photodiodes with the LED and lamp-monochromator combo. The graph on top is for the LED and the one at the bottom is for 494 nm wavelength light from the monochromator.

From the results obtained, it is possible to say that the photodiodes could determine if a channel had a fluorescent solution or not, as there is a significant difference between the 0 mM CaEGTA, the one not fluorescent, and the other solutions. However, to distinguish between the channels that are fluorescent is complicated. For the 494 nm experiment, 10 mM actually had a lower current density than the 2 or 4 mM, which is quite unexpected, since it had a much higher fluorescence signal when using a microscope, Figure 3-31, than any other solution. For the experiment using the LED, the results make more sense as the 10 mM has the highest current density, followed by 4mM, then 2 mM and finally 0 mM CaEGTA. But the difference between 0 and 2 mM ($3.9 \times 10^{-7} \text{ A.cm}^{-2}$) is greater than the one between

2 and 10 mM (2.6×10^{-7} A.cm⁻²), which is unexpected as the differences when seen through a microscope were 2.1 AU and 18.9 AU.

The results were positive, the photodiodes could differentiate between channels that did and didn't have a fluorescence solution. However, the difference between fluorescent solutions was very difficult to determine, meaning that the sensitivity of the photodiodes was not great. There are two main reasons for this lack of sensitivity. The Stokes shift for Fluo4 is very small, as the excitation (494 nm) and emission (516 nm) wavelengths are very close and the filter is not suitable for these experiments as both excitation and emission wavelengths do not have very different EQE values. These two reasons cause the photodiode to pick up the emission light (516 nm) but also the excitation light (494 nm), and since the filter is not filtering the excitation light as well as desired it will generate a similar current to the emission for the same photon flux. However, because the photon flux and intensity of light is higher for the excitation light (coming from the lamp or LED) than the emission light (coming from the calcium solution), the photodiode will be flooded with signal from the excitation and barely register a difference between two different fluorescent solutions, which is a problem. A solution for this problem could be the usage of a photodiode coupled with an interference filter which has a steep wavelength cut-off, meaning that it could completely filter 494 nm and be transparent to 516 nm, only reading the fluorescence. This solution is very expensive and difficult to fabricate, so may not be viable. Another solution is the usage of fluorophore, other than Fluo4, with a higher Stokes shift. One different marker could be Fura-2 which is excited at 340 and 380 nm, at the lower plateau of Figure 3-29, and with emission at 510 nm, still at steep phase of the curve but enabling an EQE ratio between 510 and 380 nm of 100, as opposed to 2.8 for Fluo-4. In addition, Fura-4 is commonly used to determine absolute calcium intracellular concentration, as it has a peak excitation wavelength in the presence of calcium (340 nm) and another in the absence of calcium (380 nm), so a ratio between these two wavelengths could be used to quantify the increase in absolute cytosolic calcium concentration. This would be very helpful for live cell assays with photodiodes, as the assay is between a basal fluorescence and a higher level of fluorescence, where there needs to be extreme sensitivity.

3.3.3. Microfluidic Live Cell Calcium Assay with Photodiodes

It is also worth mentioning that a live cell calcium assay was performed with detection of the intracellular calcium change being monitored using photodiodes. For this assay, the cells were treated the same way as in the microfluidic live cell calcium assays using the microscope, but instead the channel with the cells was put on top of the photodiode where the intracellular calcium change was monitored. A graph with the two different concentrations of UTP assayed is represented in Figure 3-33.

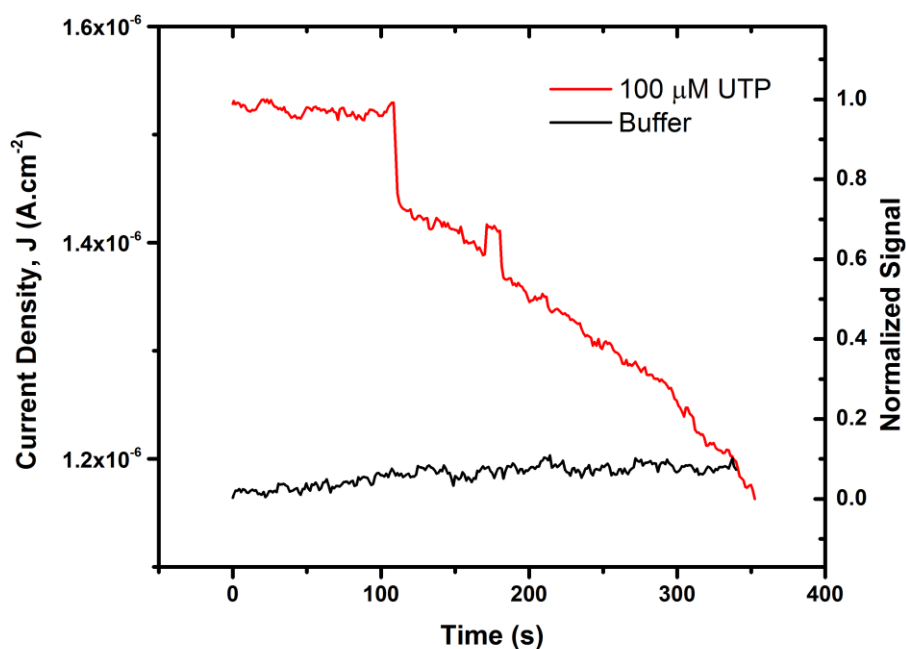


Figure 3-33 Current density vs time for a microfluidic live cell calcium assay. Buffer (0 μM UTP) and 100 μM UTP were the solutions assayed.

The results presented in Figure 3-33 are difficult to explain, as the behavior seen is unexpected. For the buffer experiment, the results indicate that the fluorescence intensity remains fairly constant. However, for the experiment with 100 μM , there seems to be an initial high plateau and then the fluorescence gradually decreases, with a slight peak in the middle. There are two possible explanations for this behavior. The cells at the beginning can be already activated, with the initial maximum fluorescence accounting for that and then steadily decrease due to bleaching, with the slight peak near time point 200 s explained by a cell that responded later than the others. Another initial explanation could be the fact that the Fluo4, which is slightly red tinted, is washed out of the chamber, leading to the decrease at 100 s, the peak at 200 s is explained by the cells responding. The first explanation seems more plausible, as further experiments with just flowing buffer after the chamber was filled with Fluo4 seemed to indicate that the washing out of the Fluo4 lead to an increase in current and not a decrease as represented. The alignment of the photodiodes with the chamber was difficult to do, and even more difficult was the alignment of the cells with the photodiode.

4. Conclusions

In the present work, the screening of GPCR targets in cells using a calcium based approach in a microfluidic platform, the use of integrated photodiodes to determine intracellular levels of calcium and a gradient generating single cell microfluidic cell platform were demonstrated, contributing towards the path to a high-throughput microfluidic drug discovery platform for the screening of GPCR targets in cells.

A technology using low cost materials, very low solution volumes for the calcium based activation of GPCRs in cells was created. The monitoring of the change in intracellular calcium concentration due to the activation of endogenous P2Y2 receptors in HEK293T cells was accomplished using a microfluidic PDMS channel with a 90 nL chamber. The activation of the P2Y2 GPCR was determined by using the fluorescent calcium indicator Fluo4 Direct™ to measure the change in intracellular calcium levels with an inverted fluorescence microscope. The assays were done with HEK293T cells adhered to a microfluidic chamber previously incubated with 8 µL of fibronectin, and UTP or suramin flowed using a peristaltic pump to agonize or antagonize the receptor. The response of the endogenous P2Y2 receptor to the agonist UTP with concentrations ranging from 0.02-100 µM was performed in the microfluidic chamber channel and microtiter plates with a Hill dose response curve fitted to the results of both platforms. For the microfluidic channel, an EC₅₀ value of 0.24 µM was obtained, which was more than an order of magnitude lower than the one obtained for the microtiter plates, between 3-4 µM. The EC₅₀ values reported in the literature ranged from 0.14 to 5.8 µM, so no conclusion regarding which method was more sensitive was reached. [15][34] The characterization of the P2Y2 receptor to its weak antagonist suramin was also performed. Although suramin at higher concentrations caused cell response above 1 mM in microtiter plates and 250 µM in the microfluidic chamber channel, it also worked as an antagonist at lower concentrations with an IC₅₀ of 342 µM, quite high compared with 50 µM reported in literature. [35] In the microfluidic channel, assays with solutions of antagonist mixed with agonist were also performed, maintaining constant the suramin concentration and changing that of the UTP's. It was observed that when higher concentrations of suramin were mixed, there is an associated EC₅₀ increase. The concentrations of suramin assayed being 250 µM and 150 µM, with EC₅₀ values of 0.52 µM and 0.3 µM, respectively, both being higher than the EC₅₀ obtained without suramin, 0.24 µM. There were some technical challenges when performing these assays; for example, notably there was a longer period of time where microfluidic cell assays were not showing good response. The reason for this might be the state of the cells after passage from a T-flask, a hypothesis is that if in previous passages the cells had very high confluence, higher than 80% confluence, they will not respond in microfluidic assays, as they become stressed because of the low cell-to-cell contact inside the microfluidic chamber. Due to stress, the cells become more sensitive, with calcium being released due to other stimuli besides GPCR activation.

A gradient generator channel with integrated hydrodynamic single cell trapping was also created, which enabled the establishing of linear molecule gradients that can be used to test different concentrations at the same time and allowing single cell variance analysis in a population. The gradient generation worked by letting separate laminar flows with different concentrations to run concurrently and mix by

diffusion, outputting a gradient of concentrations. The gradient generation aspect of the channel was demonstrated using calibrated solutions of calcium by mixing CaEGTA and K₂EGTA with Fluo4 pentapotassium salt, which binds to free calcium. In the designed and fabricated channel, three different solutions could be inserted with a gradient of five appearing in the assaying area of the channel. The formation of the gradient was monitored over time, with the time for the establishment of a steady gradient determined to be 145 s. Single cell trapping capabilities were also partly accomplished, as some cells inside the gradient generator channel were trapped individually, albeit with many traps having more than one cell. A live cell calcium assay using the gradient generator channel was also attempted, with the trapped cells dyed with Fluo4 Direct™, the assaying with a gradient of UTP was tried but technical problems with air bubbles led to the displacement of the trapped cells upon infusion pump activation.

The ability of 200 per 200 sq.micron a-Si:H photodiodes with integrated absorption filters to measure different concentrations of free calcium similar to intracellular calcium levels before and after GPCR activation in a microfluidic channel was also achieved. Despite Fluo4's low Stokes shift causing a low EQE ratio between excitation (516 nm) and emission (494 nm) wavelengths of only 2, there was a significant difference between channels with fluorescent calcium solutions and channels without fluorescence, proving that the photodiodes can detect fluorescence from calcium ions. However, when fluorescent calcium solutions of different concentrations were compared, there was practically no sensitivity when using a 494 nm wavelength from a lamp-monochromator combo. In this case, the current density for two different solutions with a difference in fluorescence of one order of magnitude, in arbitrary fluorescence units when analyzed using a microscope, had almost the same current density, with sometimes less fluorescent solutions having higher values. When using the LED with a low-pass filter, the results were better as the highly fluorescent solutions had higher current density values, however, the difference in current density between solutions was not as big as the one found when analyzing in a microscope. The monitoring of the intracellular calcium release due to P2Y2 activation with UTP was also attempted, with a lack of convincing results. The reason for this was the difficulty in aligning the cells with the photodiodes, and also the difficulty in distinguishing between different concentrations of calcium.

5. Future Work

This work proved three different concepts, that microfluidic live cell calcium assays for GPCR screening can be performed, that a gradient generation with single cell trapping can be achieved and microscale photodiodes can be used to detect calcium concentrations similar to intracellular calcium levels. So, in the future, all these concepts could be integrated into one, namely performing live cell calcium assays in a gradient generator channel with single cell trapping, while the fluorescence is being monitored by photodiodes. In this way, different concentrations of a drug can be assayed at the same time with integrated detection.

On the microfluidic channel assays, further characterization could be done, with experiments relating cell confluence in the T-flasks with cell response to an agonist. This could be performed to determine the influence of confluence on subsequent passages. Temperature control, when the channels are outside the incubator, could be employed, as the present work started in winter and ended in summer, the temperature differences might have had some influence on the results. Adding a level of automation to the assays could also be something that should be implemented. An important objective should be designing a microchannel with consistent cell insertion strategies, as the cell concentration varied greatly between assays, no doubt influencing the results.

On the gradient generation, more chambers could be used, increasing the number of concentrations being assayed and implementation of photodiodes for single cell traps could be implemented. The present channel and operating parameters could be optimized by increasing channel height, decreasing the width of the trap openings, changing flow rates and using different cell concentrations among other parameters.

For the photodiodes, there are some aspects that could be worked on to improve their sensitivity. The fluorophore could be changed, with the present one, Fluo4, having a small Stokes shift and so the current generated for the excitation light (494 nm) and emission (516 nm) being similar. This could be remedied by using another fluorophore, such as Fura-2 which has two excitation wavelengths, one in the presence of calcium at 340 nm and another in the absence at 380 nm, and an emission wavelength of 510 nm, which translates into a Stokes shift ranging from 170 nm to 130 nm contrasting with the 22 nm for Fluo4. The change in fluorophore could lead to an increase, of about 50 times, in differentiation between excitation and emission light compared to Fluo4, as the EQE ratio for the excitation and emission wavelengths, using the current photodiodes with the present filter, for Fura-2 is 100 and for Fluo4 about 2. This is a feasible change, and not difficult to implement. Another solution, albeit difficult to implement at microscale, would be the fabrication of an interference filter for the photodiodes cutting off the wavelength of 494 nm and being transparent to 516 nm, leading to low noise levels from the excitation light.

References

- [1] G. Thomas, *Fundamentals of Medicinal Chemistry*. 2003.
- [2] B. Anson, J. Ma, and J.-Q. He, "Identifying Cardiotoxic Compounds," *Gen*, vol. 29, no. 9, 2009.
- [3] S. A. M. Martins, G. Moulas, J. R. C. Trabuco, G. A. Monteiro, V. Chu, J. P. Conde, and D. M. F. Prazeres, "Monitoring intracellular calcium in response to GPCR activation using thin-film silicon photodiodes with integrated fluorescence filters," *Biosens. Bioelectron.*, vol. 52, pp. 232–238, Feb. 2014.
- [4] S. A. M. Martins, J. R. C. Trabuco, G. A. Monteiro, V. Chu, J. P. Conde, and D. M. F. Prazeres, "Towards the miniaturization of GPCR-based live-cell screening assays," *Trends Biotechnol.*, vol. 30, no. 11, pp. 566–574, 2012.
- [5] S. A. M. Martins, J. Mateus, V. Chu, D. M. F. Prazeres, and J. P. Conde, "Thin-film amorphous silicon photodiodes with integrated fluorescent filters for monitoring live-cell G-protein coupled receptors (GPCR)," *IEEE Abstr.*, 2014.
- [6] S. R. George, B. F. O'Dowd, and S. P. Lee, "G-protein-coupled receptor oligomerization and its potential for drug discovery.," *Nat. Rev. Drug Discov.*, vol. 1, no. 10, pp. 808–20, Oct. 2002.
- [7] K. Lundstrom and M. Chiu, *G Protein-Coupled Receptors in Drug Discovery*. CRC Press, 2005, p. 376.
- [8] S. A. M. Martins, J. R. C. Trabuco, G. A. Monteiro, and D. M. F. Prazeres, "GPCR Screening and Drug Discovery : Challenges and Latest Trends," vol. 17, no. 2, 2012.
- [9] D. Filmore, "It's a GPCR world.," *Mod. Drug Discov.*, vol. 7, no. November, pp. 24 – 28, 2004.
- [10] R. Zhang and X. Xie, "Tools for GPCR drug discovery.," *Acta Pharmacol. Sin.*, vol. 33, no. 3, pp. 372–84, Mar. 2012.
- [11] H. Bourne, R. Horuk, J. Kuhnke, and H. Michel, Eds., *GPCRs: From Orphanization to Lead Structure Identification*, vol. 2006/2. Berlin, Heidelberg: Springer Berlin Heidelberg, 2007.
- [12] I. Meyvantsson, J. W. Warrick, S. Hayes, A. Skoien, and D. J. Beebe, "Automated cell culture in high density tubeless microfluidic device arrays," *Lab Chip*, vol. 8, no. 5, pp. 717–24, May 2008.
- [13] L. Tran, J. Farinas, L. Ruslim-litrus, P. B. Conley, C. Muir, K. Munnely, D. M. Sedlock, and D. B. Cherbavaz, "Agonist-induced calcium response in single human platelets assayed in a microfluidic device.," *Anal. Biochem.*, vol. 341, no. 2, pp. 361–8, Jun. 2005.
- [14] G. Burnstock, "Introduction: P2 receptors.," *Curr. Top. Med. Chem.*, vol. 4, no. 8, pp. 793–803, 2004.
- [15] M. Abbracchio and G. Burnstock, "International Union of Pharmacology LVIII: update on the P2Y G protein-coupled nucleotide receptors: from molecular mechanisms and pathophysiology to therapy," *Pharmacol.*, vol. 58, no. 3, pp. 281–341, 2006.
- [16] I. Von Kügelgen and D.- Bonn, "Pharmacology of mammalian P2X- and P2Y-receptors," no. 3, pp. 59–61, 2008.
- [17] P. Tabeling, *Introduction to Microfluidics*. 2010.

- [18] E. K. Sackmann, A. L. Fulton, and D. J. Beebe, "The present and future role of microfluidics in biomedical research," *Nature*, vol. 507, no. 7491, pp. 181–9, Mar. 2014.
- [19] K. Avila, D. Moxey, A. de Lozar, M. Avila, D. Barkley, and B. Hof, "The onset of turbulence in pipe flow.," *Science*, vol. 333, no. 6039, pp. 192–6, Jul. 2011.
- [20] J. Nilsson, M. Evander, B. Hammarström, and T. Laurell, "Review of cell and particle trapping in microfluidic systems," *Anal. Chim. Acta*, vol. 649, no. 2, pp. 141–157, 2009.
- [21] A. Banaeiyan, D. Ahmadpour, C. Adiels, and M. Goksör, "Hydrodynamic Cell Trapping for High Throughput Single-Cell Applications," *Micromachines*, vol. 4, no. 4, pp. 414–430, Dec. 2013.
- [22] J. El-Ali, P. K. Sorger, and K. F. Jensen, "Cells on chips.," *Nature*, vol. 442, no. 7101, pp. 403–11, Jul. 2006.
- [23] N. Li, S. K. W. Dertinger, D. T. Chiu, I. S. Ch, A. D. Str, and M. W, "Generation of Solution and Surface Gradients Using Microfluidic Systems," pp. 8311–8316, 2000.
- [24] T. M. Keenan and A. Folch, "Biomolecular gradients in cell culture systems.," *Lab Chip*, vol. 8, no. 1, pp. 34–57, Jan. 2008.
- [25] B. E. A. Saleh, M. C. Teich, and C. J. Wiley, *Fundamentals of Photonics*, vol. 5. 1991.
- [26] F. Fixe, V. Chu, D. M. F. Prazeres, and J. P. Conde, "An on-chip thin film photodetector for the quantification of DNA probes and targets in microarrays.," *Nucleic Acids Res.*, vol. 32, no. 9, p. e70, Jan. 2004.
- [27] A. C. Pimentel, A. T. Pereira, V. Chu, D. M. F. Prazeres, and J. P. Conde, "Detection of Chemiluminescence Using an Amorphous Silicon Photodiode," *IEEE Sens. J.*, vol. 7, no. 3, pp. 2006–2007, 2007.
- [28] A. Gouveia, A. T. Pereira, A. C. Pimentel, D. M. F. Prazeres, V. Chu, and J. P. Conde, "Colorimetric detection of molecular recognition reactions with an enzyme biolabel using a thin-film amorphous silicon photodiode on a glass substrate," *Sensors Actuators, B Chem.*, vol. 135, no. 1, pp. 102–107, Dec. 2008.
- [29] A. C. Pimentel, D. M. F. Prazeres, V. Chu, and J. P. Conde, "Fluorescence detection of DNA using an amorphous silicon p-i-n photodiode," *J. Appl. Phys.*, vol. 104, no. 5, p. 054913, 2008.
- [30] A. T. Pereira, A. C. Pimentel, V. Chu, D. M. F. Prazeres, and J. P. Conde, "Chemiluminescent detection of horseradish peroxidase using an integrated amorphous silicon thin-film photosensor," *IEEE Sens. J.*, vol. 9, no. 10, pp. 1282–1290, 2009.
- [31] A. C. Pimentel, A. T. Pereira, D. M. F. Prazeres, V. Chu, and J. P. Conde, "Detection of fluorescently labeled biomolecules immobilized on a detachable substrate using an integrated amorphous silicon photodetector," *Appl. Phys. Lett.*, vol. 94, no. 16, p. 164106, 2009.
- [32] A. C. Pimentel, D. M. F. Prazeres, V. Chu, and J. P. Conde, "Comparison of amorphous silicon photodiodes and photoconductors for detection of quantum dot biomolecular tags," *J. Appl. Phys.*, vol. 106, no. 10, p. 104904, 2009.
- [33] A. Joskowiak, M. S. Santos, D. M. F. Prazeres, V. Chu, and J. P. Conde, "Integration of thin film amorphous silicon photodetector with lab-on-chip for monitoring protein fluorescence in solution and in live microbial cells," *Sensors Actuators, B Chem.*, vol. 156, no. 2, pp. 662–667, Aug. 2011.

- [34] B. Velázquez, R. C. Garrad, G. A. Weisman, and F. A. González, "Differential agonist-induced desensitization of P2Y2 nucleotide receptors by ATP and UTP.," *Mol. Cell. Biochem.*, vol. 206, no. 1–2, pp. 75–89, Mar. 2000.
- [35] S. S. Wildman, R. J. Unwin, and B. F. King, "Extended pharmacological profiles of rat P2Y2 and rat P2Y4 receptors and their sensitivity to extracellular H⁺ and Zn²⁺ ions.," *Br. J. Pharmacol.*, vol. 140, no. 7, pp. 1177–86, Dec. 2003.
- [36] D. Pesen and J. H. Hoh, "Micromechanical architecture of the endothelial cell cortex.," *Biophys. J.*, vol. 88, no. 1, pp. 670–9, Jan. 2005.

A.Appendix Section

a. Calculating Free Calcium Concentrations.

The concentrations of free calcium to use in the gradient generation and photodiode experiments were calculated using Equation 10.

$$[Ca^{2+}] = K_d^{EGTA} \times \frac{[CaEGTA]}{[K_2EGTA]} \quad \text{Equation 10}$$

In Equation 10, K_d^{EGTA} is the dissociation constant of EDTA, $[CaEGTA]$ the molar concentration of CaEGTA, $[K_2EGTA]$ the molar concentration of K_2EGTA and $[Ca^{2+}]$ the free calcium concentration. The dissociation constant of EGTA was obtained from Table A.1. The assumed pH and temperature were 7.2 and 20°C, respectively.

Table A.1 Dissociation constants of EGTA for Ca²⁺ in 0.1 M KCl

pH	K_d^{EGTA} (nM)	
	20°C	37°C
6.50	3728	2646
6.60	2354	1672
6.70	1487	1057
6.75	1182	841
6.80	940	669
6.85	747	532
6.90	594	423
6.95	472	337
7.00	376	268
7.05	299	213
7.10	238	170.0
7.15	189.1	135.4
7.20	150.5	107.9
7.25	119.8	86.0
7.30	95.4	68.6
7.35	76.0	54.7
7.40	60.5	43.7
7.45	48.2	34.9
7.50	38.5	27.9
7.60	24.5	17.88
7.70	15.61	11.49
7.80	9.99	7.42
7.90	6.41	4.82
8.00	4.13	3.15
8.10	2.68	2.08
8.20	1.75	1.39

b. Video Analysis Methods

The video analysis was done using ImageJ software, with two methods being used. A method where the video would not be modified and only be subjected to a mean intensity over time measurement (Plot Z Axis Profile). On the other method used, the background (area not occupied by cells) was removed using software imaging tools. Both methods are going to be explained below.

No background removal method

The video is opened in ImageJ, the option chosen when prompted is to convert the stack to grayscale.

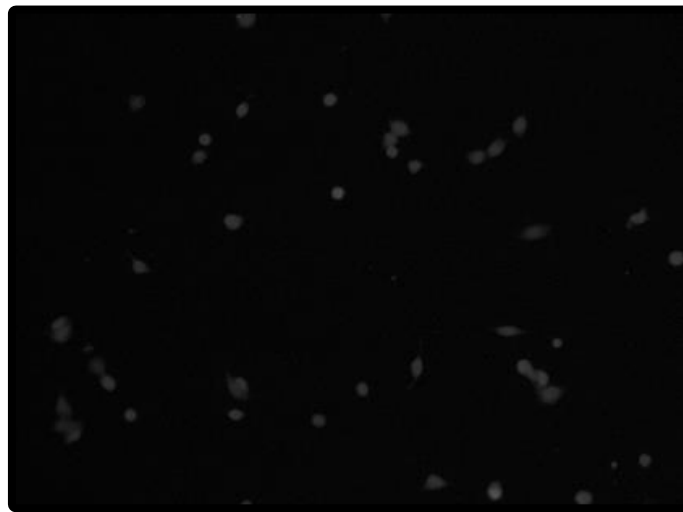


Figure A-1 Stack converted to grayscale.

Then the “Image/Stacks/Plot Z-axis Profile” option in the dropdown menu chosen, with the resulting graphic appearing. This command plots the mean gray value versus slice, with each slice accounting for 1 second.

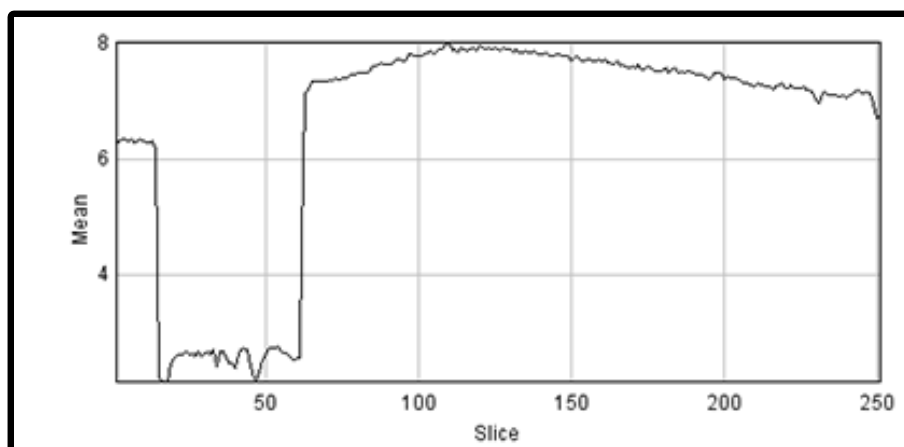


Figure A-2 Mean image intensity values over time, without removing background

Background removal method

The video is opened just like in the previous method and converted to grayscale (Figure A-1). Then instead of using the “Plot Z-axis Profile” command, the “Image/Stacks/Z Project...” command is chosen. The Z Project option is selected for Maximum Intensity. This command creates an output image wherein each pixel in that image represents the maximum value over all images of the video at the particular pixel location (Figure A-3).

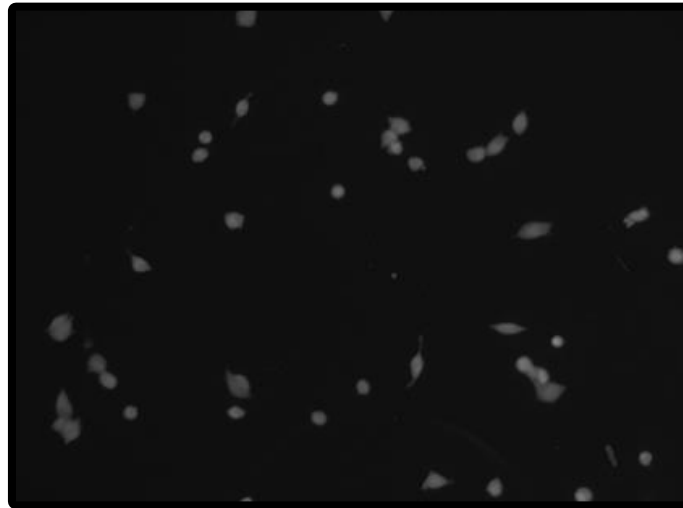


Figure A-3 Z Project image representing the maximum intensity of each pixel of the stack.

The brightness and contrast (“Image/Adjust/Brightness-Contrast”) are adjusted to obtain a more intense image. The adjustment is set to auto, to have the program select the best way to adjust these definitions.

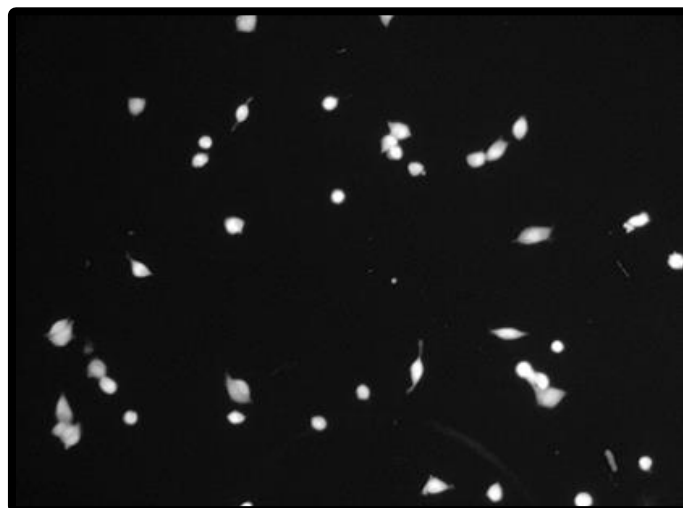


Figure A-4 Enhanced Z Project image

Then the threshold of the image is adjusted so that the area occupied by the cells is filled with white and the remainder area black, using “Image/Adjust/Threshold”. This command enables the segmentation of

grayscale images into features of interest and background, the features of interest in this case being the cells. Again the threshold is set to auto.

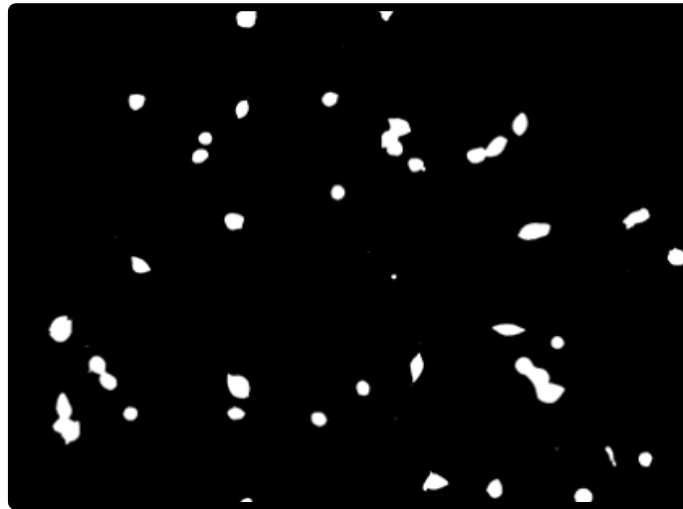


Figure A-5 Enhanced Z Project image after being subjected to an auto threshold.

The threshold image obtained is subtracted to the original stack, so that only the area with cells is with its original composition and the background is black (intensity 0). This is done by using the command “Process/Image Calculator...”



Figure A-6 Stack with the background removed.

After the background is removed the command “Image/Stacks/Plot Z-axis Profile” is used, to obtain the final graphic with the values to be used to determine the maximum fluorescence of the cells. The comparison between the two methods can be seen in Figure A-7. After removing background the noise level that appeared to influence the results if not removing the background are minimized and the cell response curve smoothed.

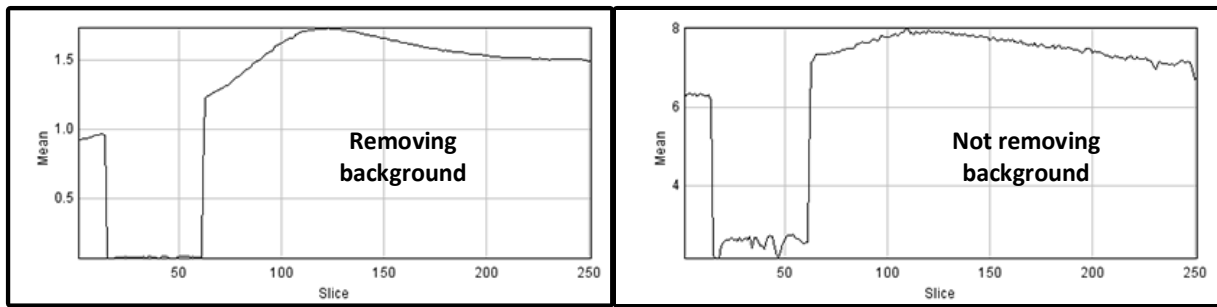


Figure A-7 Comparison of the final results after removing and not removing background.

In order to not have to manually execute every one of these commands each time for one of the hundreds of videos obtained from the experiments, a macro was developed to automatically process the videos using both methods. In this macro the user could choose a folder to analyze, and the macro would process each video in that folder. It would then create three new subfolders on the same folder, one to save both Z-axis profiles, such as the ones in Figure A-7, for the user to observe the visual differences between the two methods, another to save a list of values of intensity over time for the method of not removing background and the last folder to save the list for the method of removing background. The ImageJ macro code is shown below.

```

macro "Ultimate Batch Process [F8]" {
requires("1.33s");
dir = getDirectory("Choose a Directory ");
setBatchMode(true);
count = 0;
time1=getTime();
countFiles(dir);
n = 0;
numberproc=0;
first=true;

myDir1 =dir+"Remove_Background"+File.separator;
File.makeDirectory(myDir1);
if (!File.exists(myDir1))
    exit("Unable to create directory");

myDir1 =dir+"Simple Z-Projection"+File.separator;
File.makeDirectory(myDir1);
if (!File.exists(myDir1))
    exit("Unable to create directory");

myDir2 =dir+"Plot Comparison"+File.separator;
File.makeDirectory(myDir2);
if (!File.exists(myDir2))
    exit("Unable to create directory");

processFilesUltimate(dir);
//print(count+" files processed");

function countFiles(dir) {
list = getFileList(dir);
for (i=0; i<list.length; i++) {
if (endsWith(list[i], ".avi"))
countFiles(""+dir+list[i]);
else
count++;
}
}

function processFilesUltimate(dir) {
list = getFileList(dir);
for (i=0; i<list.length; i++) {
if (endsWith(list[i], ".avi"))
processFilesUltimate(""+dir+list[i]);
else {
showProgress(++count);
path = dir+list[i];
processFileUltimate(path);
}
}
}

function processFileUltimate(path) {
if (endsWith(path, ".avi")) {
print(path);
run("AVI...", "select=&path first=1
convert");
name=getTitle();
run("Plot Z-axis Profile");
saveAs("Jpeg", myDir2+name);
Plot.getValues(xvalues, yvalues);
f = File.open(myDir1+name+".txt");
for (i=0; i<xvalues.length; i++) {
print(f,xvalues[i]+"\t"+yvalues[i]);
}
File.close(f);
selectWindow(name);
stacktitle=getTitle();
run("Z Project...", "start=1 stop=500
projection=[Max Intensity]");
//run("Brightness/Contrast...");
run("Enhance Contrast", "saturated=0.35");
run("Apply LUT");
setAutoThreshold("Default");
//run("Threshold...");
setOption("BlackBackground", false);
run("Convert to Mask");
imagetitle=getTitle();
imageCalculator("Subtract create stack", stacktitle,
imagetitle);
resulttitle=getTitle();
run("Plot Z-axis Profile");
saveAs("Jpeg", myDir2+name+" No Background");
Plot.getValues(xvalues, yvalues);
f = File.open(myDir1+name+".txt");
//print(f,name);
for (i=0; i<xvalues.length; i++) {
print(f,xvalues[i]+"\t"+yvalues[i]);
}
File.close(f);
close(imagetitle);
close(resulttitle);
selectWindow(stacktitle);
close();
selectWindow("Results");
run("Close");
numberproc++;
}
}

time2=getTime();
time=(time2-time1)/1000;
time=floor(time/60);
times=round(time%60);
Dialog.create("Done");
Dialog.addMessage("Processed "+numberproc+"
files in "+time+" minutes and "+times+"
seconds.");
Dialog.show();
selectWindow("Log");
run("Close");
}
}

```

c. AutoCAD Microchannel Designs

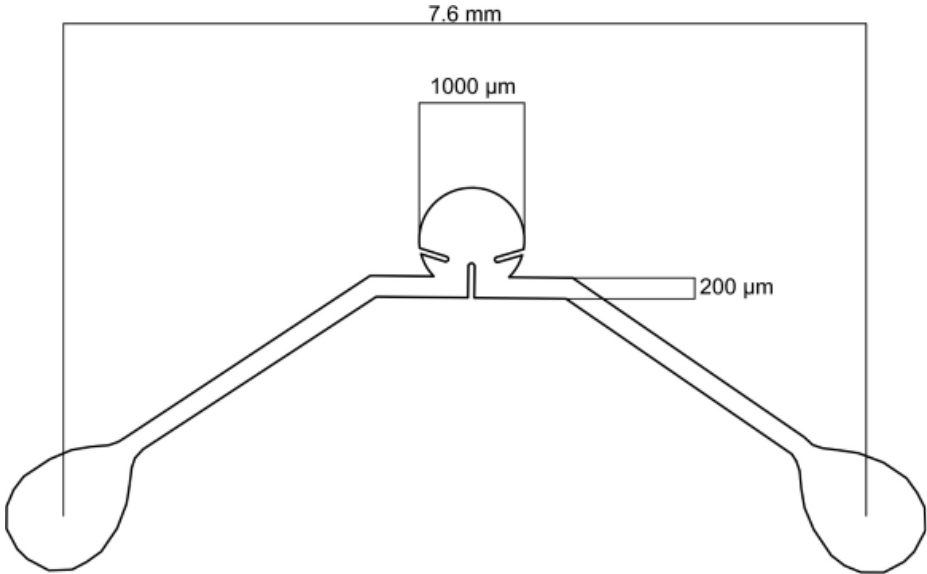


Figure A-8 Microfluidic chamber channel schematics. This was the main channel used for the microfluidic experiments. Its main feature is the central chamber where the cells are assayed.

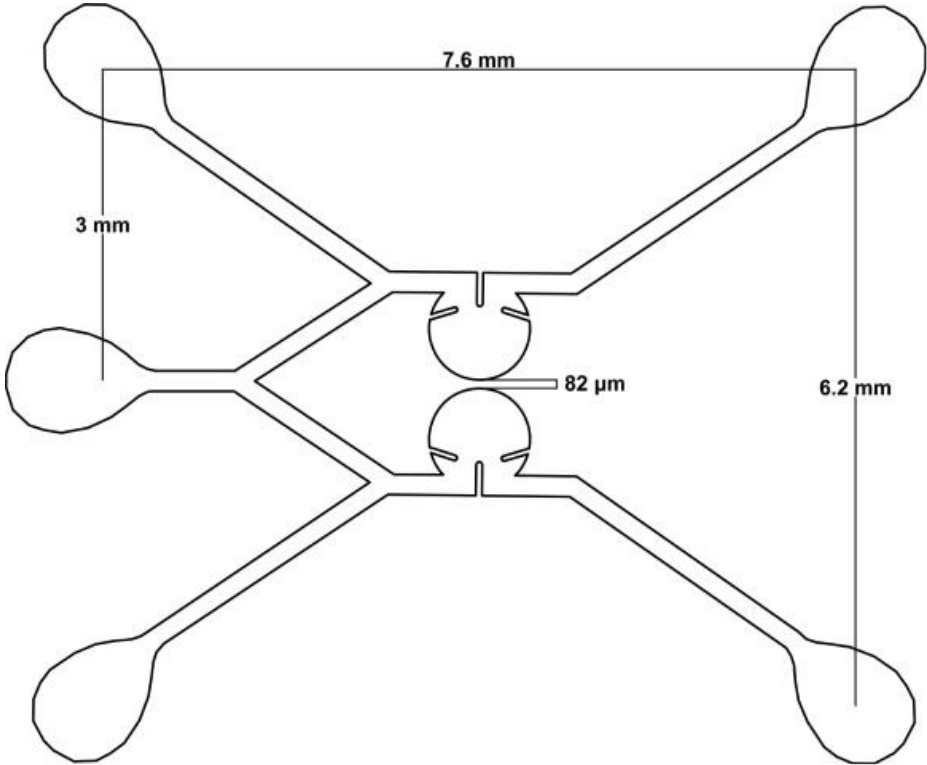


Figure A-9 Dual chamber variation of the microfluidic chamber channel. This structure was designed for the purpose of performing two assays at once, with the middle inlet serving as a feeder for common reagents. This design was just conceptual and never converted into a hard mask.

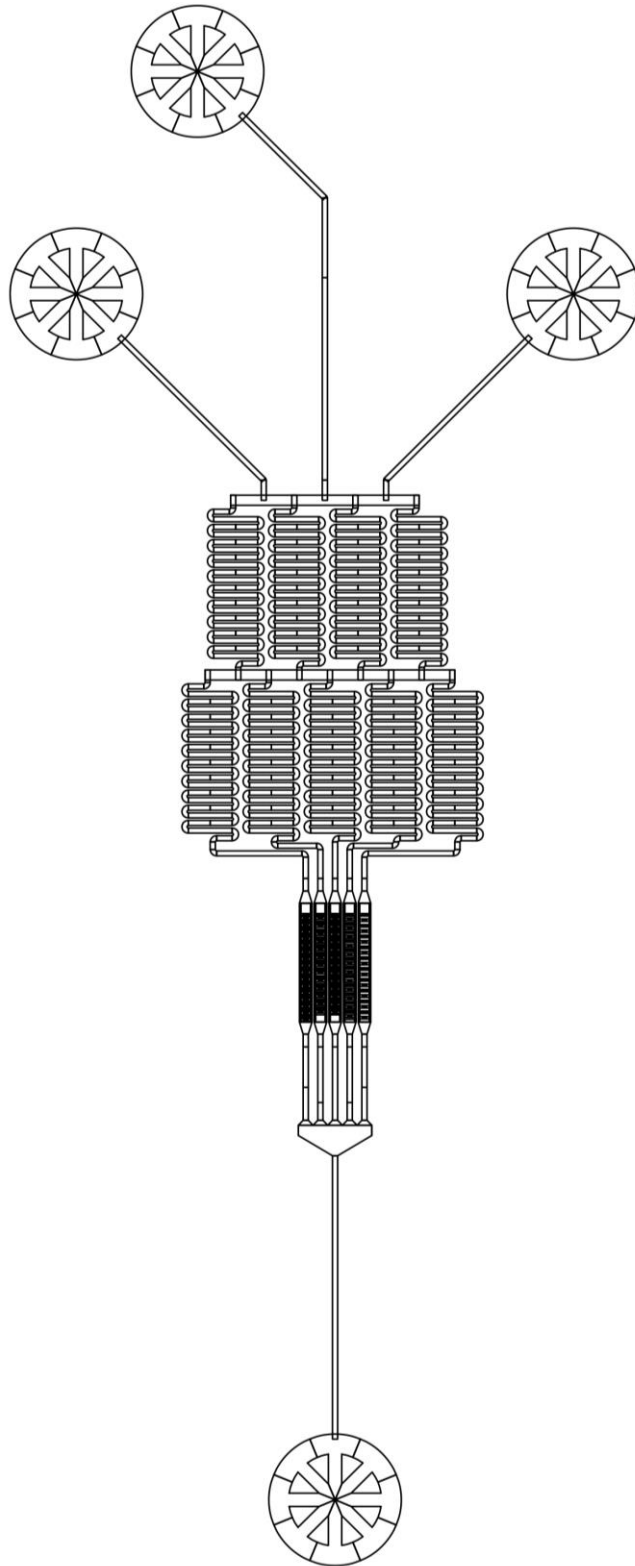


Figure A-10 Gradient generator channel schematics.

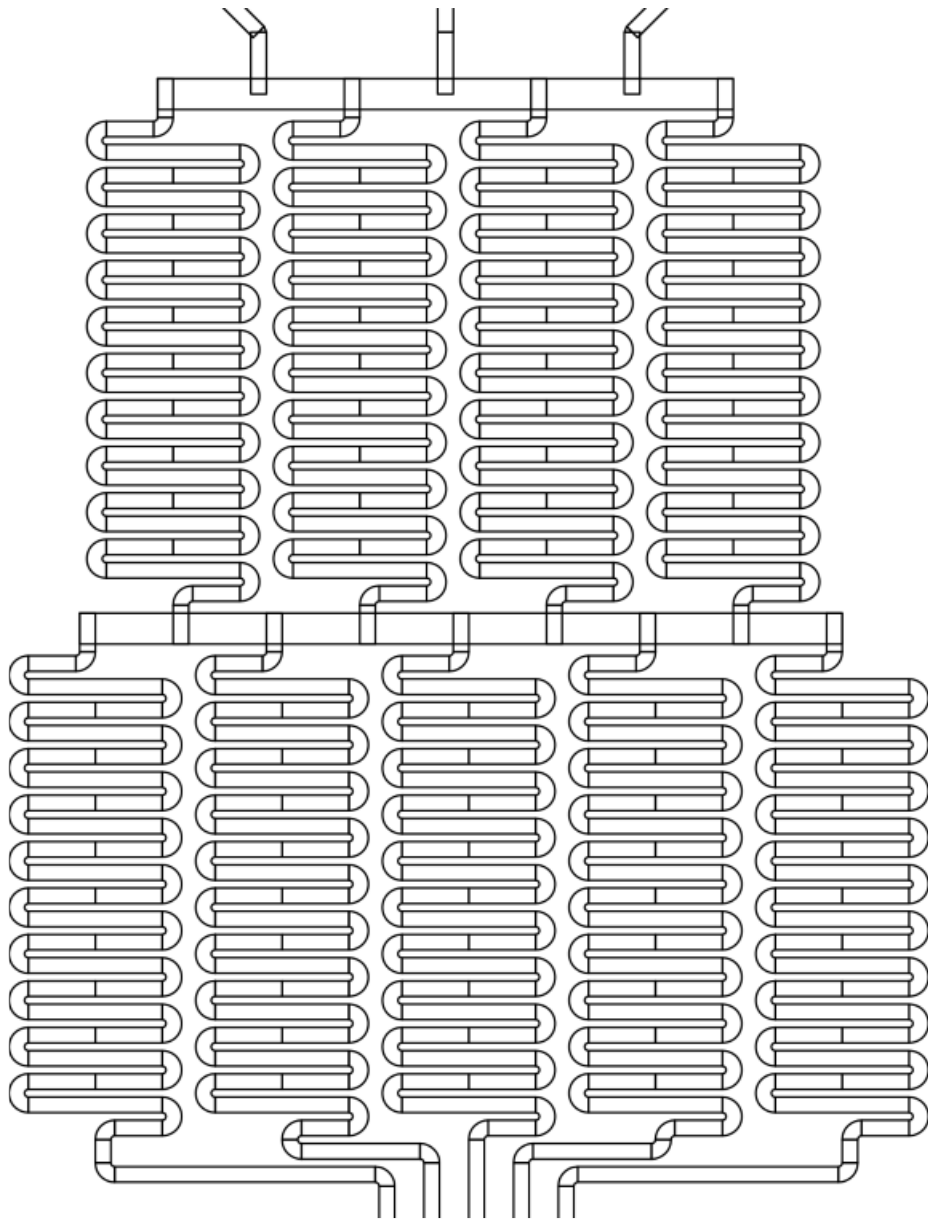


Figure A-11 Serpentine section of the gradient generator channel. It is in this section that the fluid will mix and form a gradient in the trap section.

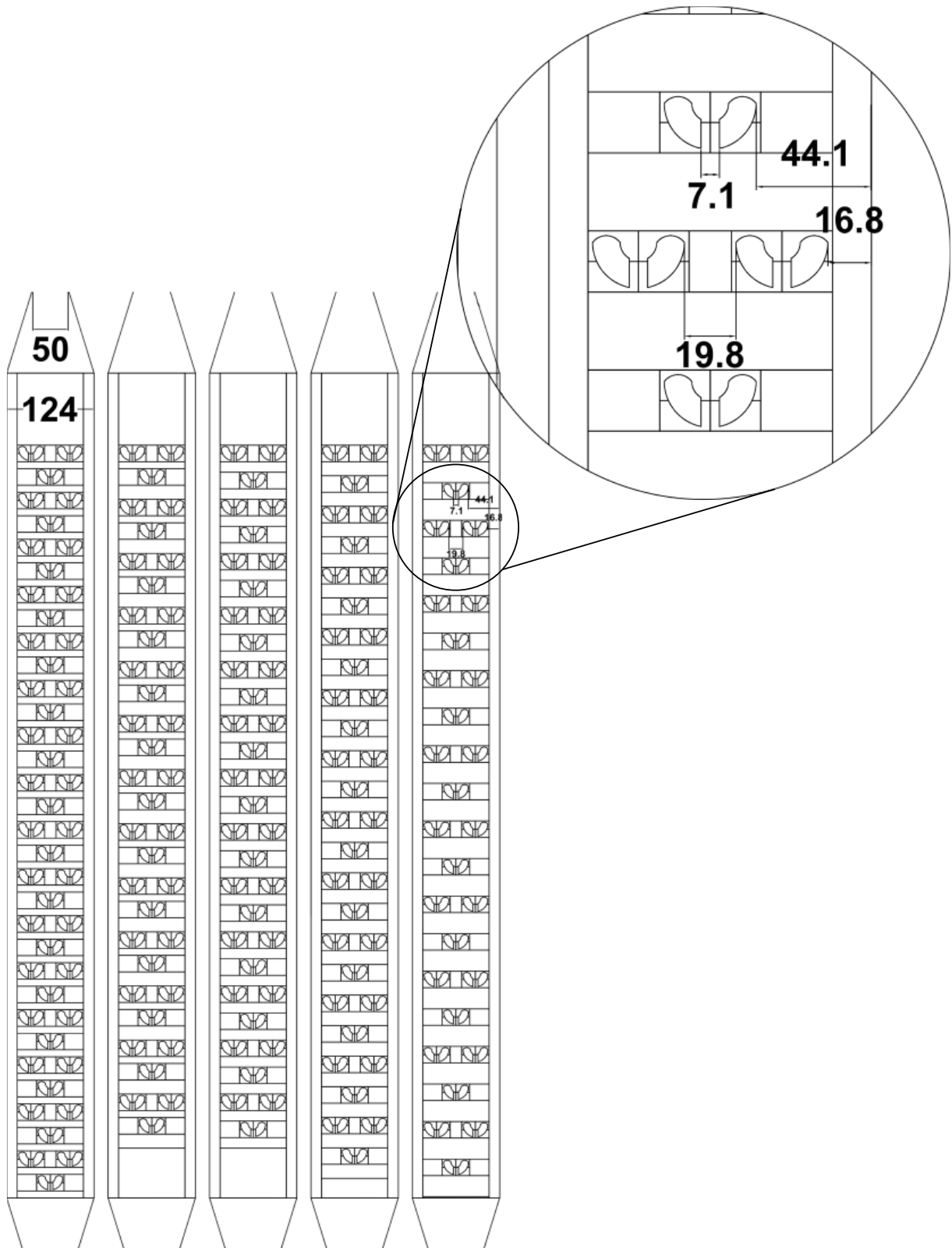


Figure A-12 Gradient generator trapping area close-up. The dimensions show are in micrometers.

d. Crystalline Silicon Photodiode

The photon fluxes of the LED and the light from the monochromator at 494 and 516 nm was measured in a calibrated photodiode, with the values in the table below used.

Table A.2 Spectral response characteristic of the Hamamatsu photodiode.

W. L.	S	Q. E.									
nm	mA/W	%									
200	114	70.9	350	148	52.3	600	306	63.2	900	220	30.2
210	119	70.4	360	144	49.7	620	317	63.4	920	190	25.6
220	122	68.5	370	145	48.6	640	325	63.0	940	159	21.0
230	125	67.6	380	156	50.8	660	333	62.6	960	128	16.6
240	128	66.3	390	169	53.7	680	339	61.8	980	100	12.6
250	121	60.0	400	178	55.2	700	343	60.7	1000	73	9.0
260	110	52.5	420	196	57.9	720	344	59.3	1020	50	6.1
270	98	45.2	440	210	59.3	740	343	57.5	1040	33	3.9
280	101	44.7	460	224	60.3	760	341	55.6	1060	21	2.5
290	113	48.4	480	237	61.3	780	333	53.0	1080	14	1.6
300	127	52.7	500	250	61.9	800	323	50.1	1100	9	1.0
310	136	54.5	520	260	62.1	820	309	46.8	1120	6	0.6
320	141	54.7	540	273	62.7	840	293	43.2	1140	3	0.3
330	144	54.1	560	285	63.0	860	271	39.1	1160	1	0.1
340	147	53.5	580	295	63.0	880	247	34.8	1180	1	0.1

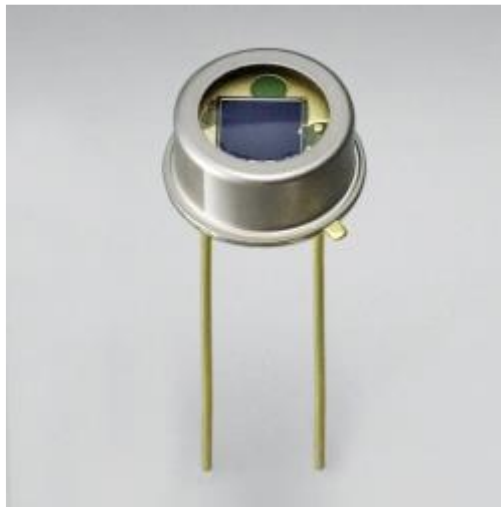


Figure A-13 Hamamatsu S1226-5BQ crystalline silicon photodiode.

e. Hydrogenated Amorphous Silicon Photodiode

In this section of the appendix section, some extra photos and schematics pertaining to the hydrogenated amorphous silicon photodiode used in this work will be shown

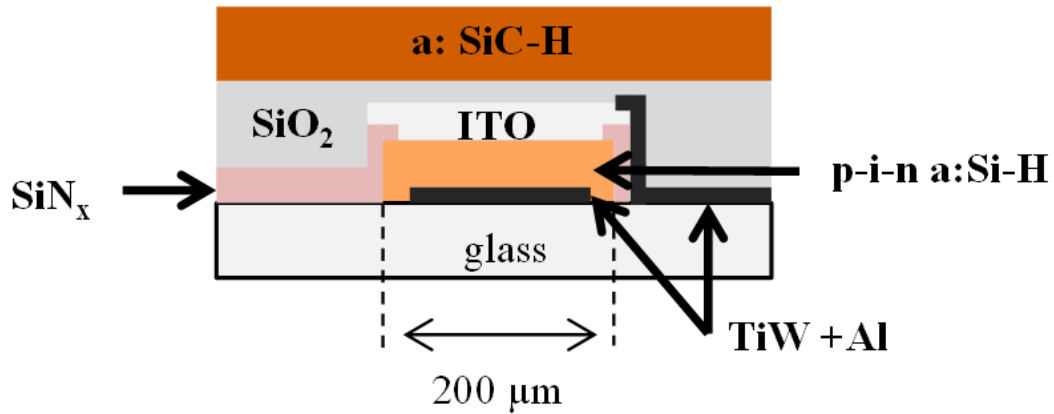


Figure A-14 Cross section of the $200 \times 200 \mu\text{m}^2$ hydrogenated amorphous silicon photodiodes used. Image used with permission from Dr. Sofia Martins.

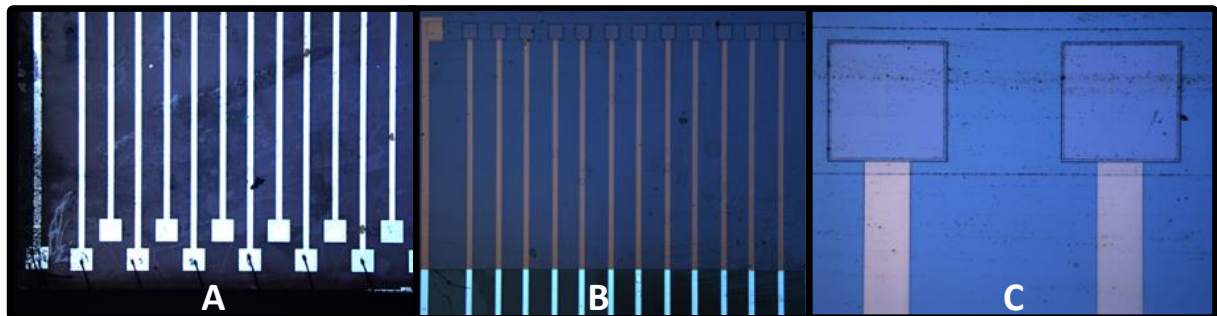


Figure A-15 Amplification of different areas of the hydrogenated amorphous silicon photodiodes. A) The contact pads that connect the photodiodes to the picoammeter. B) The 12 array photodiodes. C) Amplification of two photodiodes with $200 \times 200 \mu\text{m}^2$. Image used with permission from Dr. Sofia Martins.

f. SolidWorks Support

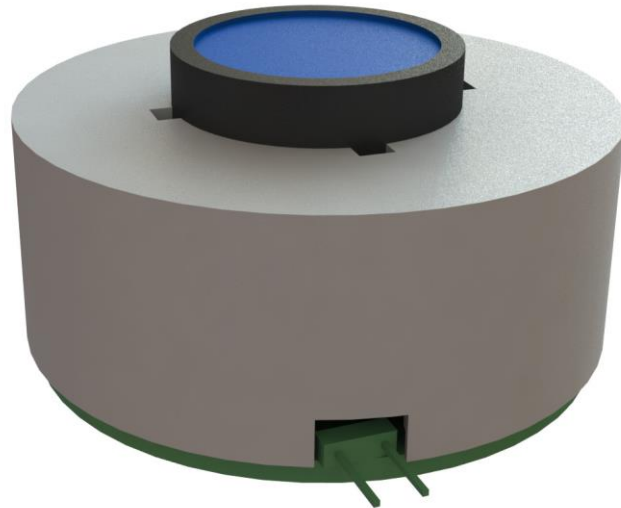


Figure A-16 LED-filter system with the support made in SolidWorks. The 3D printed part is in gray, it has at the bottom a slot for the power supply connector and on top, an opening where the filter is placed.

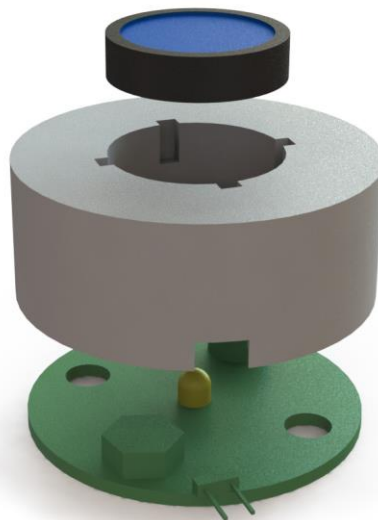


Figure A-17 Exploded view of the LED-filter system. The bottom part is the base of the LED with a connector to the power supply, in the middle is the 3D printed support and at the top is the low pass filter.